Universität Hamburg
DER FORSCHUNG | DER LEHRE | DER BILDUNG

FAKULTÄT
FÜR MATHEMATIK, INFORMATIK
UND NATURWISSENSCHAFTEN

Attosecond Quantum Dynamics of Molecular Inner-Shell Processes

Dissertation

zur Erlangung des Doktorgrades
an der Fakultät für Mathematik, Informatik und Naturwissenschaften
Fachbereich Physik
der Universität Hamburg

vorgelegt von

Milad Behrooz

Hamburg
2022

Gutachter/in der Dissertation:	Prof. Dr. Daniela Pfannkuche
	Prof. Dr. Robin Santra
Zusammensetzung der Prüfungskommission:	Prof. Dr. Markus Drescher
	Prof. Dr. Daria Gorelova
	Prof. Dr. Sven-Olaf Moch
	Prof. Dr. Daniela Pfannkuche
	Prof. Dr. Robin Santra
Vorsitzende/r der Prüfungskommission:	Prof. Dr. Sven-Olaf Moch
Datum der Disputation:	29.07.2022
Vorsitzender das Fach-Promotionsausschusses Physik:	Prof. Dr. Wolfgang J. Parak
Leiter des Fachbereichs Physik:	Prof. Dr. Günter H. W. Sigl
Dekan der Fakultät MIN:	Prof. Dr. Heinrich Graener

Eidesstattliche Versicherung

Hiermit versichere ich an Eides statt, die vorliegende Dissertationsschrift selbst verfasst und keine anderen als die angegebenen Hilfsmittel und Quellen benutzt zu haben.

Hamburg, den 09.05.2022

Milad Behrooz

Acknowledgments

First of all, I would like to thank my supervisor Daniela Pfannkuche for giving me the opportunity to pursue my Ph.D. in the *Quantentheorie der Kondensierten Materie* Group. She helped me to find new approaches to overcome difficulties and without her continued support and advice, this thesis would not have been possible. Moreover, I appreciate her support in enabling me to attend conferences and summer schools.

Furthermore, I am very grateful to my co-supervisor Robin Santra for providing help to find the direction of this work and many clarifying discussions and advices. During our discussions, I learned a lot from his intuition for ultrafast phenomena and atomic and molecular physics.

I would also like to thank the other committee members Markus Drescher, Daria Gorelova and Sven-Olaf Moch for agreeing to form my examination committee.

In addition, I would like to express my gratitude to my colleagues for always being approachable and helpful. Special thanks go to Lars-Hendrik Frahm for his patience in answering my questions about many-body theory and quantum chemistry in the early stages of my project. I would like to thank Thorben Schmirander and Motilal Jana for having a great time in our office and many opportunities to talk about different aspects of physics. Frederik Bartelmann has helped a lot with answering my non-physics questions, proofreading my thesis, and traslation of the abstract. It was a pleasure to work with Daniel Duarte Ruiz and Hosnieh Safaei Katoli as well as all past and present members of the *Quantentheorie der Kondensierten Materie* group, responsible for a nice working atmosphere.

Special thanks go to the PHYSnet team, Martin Stieben, Michael Vedmedenko, and Bodo Krause-Kyora for providing rapid and flexible IT supports.

Finally, I would like to extend my sincere thanks to my family and friends. Without their tremendous understanding and encouragement in the past few years, it would have been impossible for me to complete my doctoral work.

Abstract

With the advent of ultrafast spectroscopy techniques based on attosecond light pulses, tracing the electronic motions in molecular systems under non-equilibrium conditions has become feasible. A good example of such kind of conditions would be the response of the electronic cloud to an ultrafast perturbation such as ultrafast excitation or ionization. To interpret the experimental data, it is necessary to have a precise computational method to simulate electron dynamics by properly including quantum many-body effects. In the recent five years, some algorithms have been developed to extend the density matrix renormalization group (DMRG) concept and the matrix product state (MPS) method to describe the time-dependent phenomena in molecules. One of these algorithms, which has been implemented by Frahm, is based on the time-evolution of the many-body wave function in the MPS representation. It has been shown that this method is capable to describe electron dynamics in ionized molecules efficiently. This work is the continuation of Frahm's work. In this thesis, we firstly investigate the role of the ordering of orbitals and of numerical noise on the performance of variational optimization of the MPS as the heart of the time-dependent MPS approach. We see that the ordering of the orbitals plays an important role in the performance of the time-dependent MPS method to describe the electron dynamics in the core ionized silicon tetrafluoride molecule. Furthermore, we show that the numerical noise can enhance the efficiency of the MPS approach by improving the convergence rate of the dynamics in terms of the MPS bond dimension. Additionally, we study the charge migration triggered by the ionization of the $2p$ orbital of the silicon atom in the silicon tetrafluoride molecule and pinpoint how electronic correlations lead to intense and fast electron dynamics in the valence orbitals while the initial hole stays unchanged during the process. Finally, we study the role of the nuclear geometry on the charge migration process and find out that considering the finite width of the nuclear wave function may lead to a damping of the charge migration.

Kurzzusammenfassung

Moderne Ultraschnelle Spektroskopiemethoden, auf Basis von Attosekundenpulsen ermöglichen es, Elektronenbewegungen in molekularen Systemen auSSerhalb des Gleichgewichts zu verfolgen. Ein gutes Beispiel für ein solches System im Ungleichgewicht ist die Reaktion einer Elektronenwolke auf eine ultraschnelle Anregung oder Ionisierung. Zur Interpretation experimenteller Daten ist eine präzise Berechnungsmethode erforderlich, um mittels dieser die Elektronendynamik unter Berücksichtigung von Quanten-Vielteilchen-Effekten zu simulieren. In den letzten fünf Jahren wurden mehrere Algorithmen zur Erweiterung des Konzepts der Dichtematrixrenormalisierungsgruppe (DMRG) und der Methode der Matrixproduktzuständen (MPS) entwickelt, um diese auf zeitabhängige Phänomene zu erweitern. Einer dieser Algorithmen, entwickelt von Frahm, basiert auf der Zeitentwicklung der Vielteilchen-Wellenfunktion in der MPS-Darstellung. Es wurde gezeigt, dass diese Methode geeignet ist, um die Elektronendynamik in ionisierten Molekülen effizient zu beschreiben. Diese Arbeit ist die Fortführung der Arbeit von Frahm. Wir untersuchen zunächst die Auswirkung der Ordnung der Orbitale und von numerischem Rauschen auf die Performanz von variationeller Optimierung der MPS als Kern des zeitabhängigen MPS-Ansatzes. Bei der Beschreibung von kernionisiertem Siliciumtetraflourid sehen wir, dass die Ordnung der Orbitale eine bedeutende Rolle für die Performanz der MPS-Methode spielt. AuSSerdem zeigen wir, dass das numerische Rauschen die Effizienz des MPS-Ansatzes verbessern kann, indem es die Konvergenzrate der Dynamik hinsichtlich der MPS-Bond-Dimension erhöht. Darüberhinaus untersuchen wir die Ladungsmigration, die durch die Ionisierung des 2p-Orbitals des Siliciumatoms in Siliciumtetraflourid ausgelöst wird, und stellen fest, wie elektronische Korrelationen zu intensiver und schneller Elektronendynamik in den Valenzorbitalen führt, wobei der ursprüngliche Lochzustand während der Prozesse unverändert bleibt. AbschlieSSend analysieren wir die Bedeutung der Geometrie der Atomkerne auf den Prozess der Ladungsmigration und stellen fest, dass die Annahme einer endlichen Breite der nuklearen Wellenfunktion zu einer Dämpfung der Ladungsmigration führen kann.

Contents

Introduction

1

Quantum mechanics is a fundamental theory in physics which describes nature at the scale of atoms and subatomic particles. In the 19th century, several discoveries and experiments showed that existent classical theories can not explain phenomena correctly. These failures led to the first ideas in the development of quantum theory in the early 19th century. Quickly after the introduction of the ideas and principles of the quantum theory, scientists applied it to physical systems to discover their properties [1, 2]. Simultaneously with the development of the mathematical formulation of quantum mechanics, several experiments were performed to confirm its predictions and discover new phenomena. Today, around a hundred years later, quantum based technology plays an important role in our daily life. For example, the transistors as the heart of smartphones and other electronic gadgets, which are widely used in our daily life, work based on the laws of quantum mechanics [3].

Molecular systems are one of the most interesting manifestations of quantum mechanics. The electrons which move on Ångstrom length scale and attosecond time scale are the key cause of formation of molecular bonds [4]. Therefore, a chemical reaction is a result of quantum mechanics. In this picture, quantum mechanics emerges in chemistry. The field of quantum chemistry, which was pioneered by physicists in the early 20th century [5], is an effort to integrate our understanding of quantum physics and molecular systems to realize the foundation of chemistry. This framework is essential for promoting physics and chemistry, since only collaboration between theory and experiment allows any scientific finding to be interpreted and validated.

The interaction between molecules and light provides the possibility to investigate the electronic motion in atoms and molecules directly. Photoinduced processes in atoms and molecules play an important role in physics, chemistry, and biology [6–9]. Generally, such processes are the foundation of several phenomena ranging from photosynthesis [10] to charge transfer in solar cells [11]. In these processes the first response of the molecule with light is manifested by initiating extremely fast dynamics of the electrons in the system which takes place on the femtosecond to attosecond timescale. On these timescales, only electronic interactions are taken into account and nuclear motion can be

neglected. In other words, on these very short timescales, different dynamical effects in a molecular system can occur before nuclear motion initiates effectively.

Nowadays, with the development of the time-resolved spectroscopic techniques [12] and availability of attosecond laser pulses [13], scientists acquire a powerful tool to track dynamics of the electrons in atoms and molecules to study processes that occur on time scales in which nuclear motion can be neglected [14]. A good example of this kind of process would be the response of the electronic cloud to an ultrafast excitation or ionization. More than 20 years ago, it was shown [15] that after a sudden ionization, the electronic many-body effects are capable of generating ultrafast electron dynamics . The positive charge generated after the ionization can migrate throughout the system solely by electron correlation and electron relaxation [16]. Generally, it is called charge migration to illustrate the difference between this process and normal electron and hole transfer, which is driven by nuclear motion [17].

To interpret the experimental results correctly, it is essential to have precise ab initio calculations which describes the time-evolution of the electronic cloud under consideration of many-body effects. In other words, for the proper description of the above-mentioned processes, one needs a dynamical treatment of the electronic many-body wave function. Considering the fixed position for nuclei and solve time-dependent Schrödinger equation for the electronic part of the many-body wave function. Due to the complexity of the problem, which is caused by the huge number of degrees of freedom, finding an accurate theoretical method to solve the time-dependent Schrödinger equation for a many-electron system is one of the main challenges in today's physical and chemical science.

So far, various numerical approaches have been developed to solve the time-dependent Schrödinger equation for the many-electron system ranging from exact solutions to approximate methods where the number of degrees of freedom is reduced. The exact numerical solution [1] is highly computationally costly and it is currently available only for two-electron systems (e.g. see [18]). Therefore, approximate methods currently are getting attention to treat the electron dynamics in the molecules. In this kind of methods, the number of degrees of freedom is significantly reduced to decrease the computational costs, whereas, the wave function is still proper to represent the fundamental mechanisms in the many-electron molecules accurately. Until now, a large family of approximate methods has been developed. This kind of methods can

[1] The solution where the complete basis set limit and full CI method are employed.

be separated into two different approaches. The first approach builds upon the Hartree-Fock theory where the molecular orbitals are employed to describe the molecule. In the second approach, which is based on the density functional theory [19], in the contrast to the first approach, charge density is used instead of the quantum mechanical states.

The Hartree-Fock method is based on describing the molecular state by a single Slater determinant. This approximation leads to the reduction of the many-body problem to a set of coupled single electron problems that are solved self-consistently. The resulting many-body state of the molecule is a simple product state of the molecular orbitals which does not describe electronic correlation. Therefore, to include electronic correlations, the post-Hartree-Fock methods have been developed. This family of methods is based on Hartree-Fock molecular orbitals, but in those, more determinants are employed to describe the molecular states [20].

For example, the configuration interaction (CI) method is one of the most popular post-Hartree-Fock methods which is also employed in time-dependent problems in addition to ground state calculations [21–23]. In this method, if one considers all the possible excited determinants to construct the many-electron molecular state, which is called full configuration interaction (full CI), then the system can be described exactly by introducing all the electronic correlations which exist in the system. However, while the full CI wave function can describe the molecule exactly, it is computationally expensive and only can be applied to small systems. To overcome this issue, truncation of the CI space with respect to the excitation level relative to the Hartree-Fock ground state is essential. The most common approximation to truncate the CI wave function is to consider only single and double excitation, configuration interaction singles and doubles (CISD). Although, this approximation leads to significant reduction of the number of degrees of freedom and thereby save the computational resources, but may induce large errors in the calculations, especially in the time-dependent cases.

In contrast to the above-mentioned approach, where a restricted number of determinants is employed to describe the molecular state, the so-called density matrix renormalization group (DMRG) [24] can produce the many-body wave function precisely and give full CI like results without considering all the excitations [25–29]. In the representation of the many-body wave function in DMRG, instead of cutting configurations from the many-body Hilbert space, electronic correlation is considered and the entanglement from the many-body

state is cut dynamically. In this case, it is assumed that the entanglement of the electrons in the system is limited and the many-body wave function of the molecule can be represented in terms of the matrix product state (MPS) [30].

So far, various methods have been developed to extend the DMRG concept and MPS method to describe time-dependent phenomena, but most of those are only applicable to systems with local interactions [31–33]. However, to date, several studies have been done to implement the time-dependent DMRG and MPS to describe the dynamics in long-ranged interaction systems [34–41], but employing these methods for quantum chemical systems is still new and challenging, and so far only few studies has been done in this field [42–46].

In the recent years an outstanding work to extend the MPS approach to dynamical phenomena in the quantum chemical system has been done by Frahm [45, 47]. He has implemented the time-dependent MPS to investigate the the ultrafast response of electrons in molecules to sudden ionization. He firstly developed the Hamburg CheMPS2 program to investigate the electron dynamics in the molecules, and then, to pinpoint the performance of the MPS approach, he has done several benchmarking tests for small systems such as 10 site hydrogen chain (10 electrons in 10 orbitals), the hydrogen fluoride molecule (10 electrons in 11 orbitals), the water molecule (10 electrons in 13 orbitals), the ammonia molecule (10 electrons in 15 orbitals), and the methane molecule (10 electrons in 17 orbitals). To do benchmark tests, he used small basis sets and compared the MPS based calculation with the quasi exact (full CI) calculations. In addition, he has employed the MPS approach to resolve the charge migration in iodoacetylene (16 electrons in 26 orbitals) which is triggered by ionization out of the linear combination of the outermost valence orbitals namely highest occupied molecular orbital (HOMO) and second highest occupied molecular orbital (HOMO-1).

Further to Frahm's work, other studies have been done by using the Hamburg CheMPS2 extension. For example, Weißler has been studying the impact of light pulses on the hydrogen chain using MPS approach by incorporating light pulse into Hamburg CheMPS2 extension [48], Schaub has been investigated the charge migration dynamics in an ionized water molecule [49] and van Hülst has been investigating the electronic response of the water molecule to light pulses and the induced dynamics [50]. It should be noted that in all the above-mentioned studies, small molecules with poor basis sets have been investigated. In the benchmarking part of Frahm's studies or other studies by Weißler, Schaub, and van Hülst, simple chemical systems have

been considered where employing small basis sets provides the possibility to describe the molecules with a few number of orbitals. In addition, although, charge migration in the iodoacetylene is a correlated dynamic, but due to the ionization out of the outer valence orbitals, it is not essentially highly correlated and can be described in terms of a few excited determinants [51].

This work is a continuation of the work that has been done by Frahm. In this thesis, we use the MPS approach to study the molecular inner-shell processes. We specifically investigate the correlation-driven charge migration in the core ionized silicone tetrafluoride molecule and show how the core ionization triggers ultrafast electron dynamics in the valence shell of the molecule.

This thesis is organized as follows. Chapter 2 includes a brief introduction of ab initio quantum chemistry. We briefly introduce the Born-Oppenheimer approximation and the Hartree-Fock method to describe the many-body state in molecules in the uncorrelated picture. Finally, we outline the configuration interaction method as a post-Hartree-Fock method to take into account electronic correlations. In Chapter 3, we introduce the MPS method in the context of quantum chemistry and outline its properties. Further, in this chapter, we discuss the exploitation of the symmetries of the molecule to reduce the dimension of the many-body Hilbert space and simplify the MPS tensors. Chapter 4 presents the time-evolution of the MPS in terms of the Krylov space method. Furthermore, the variational optimization of the MPS method at the heart of the time-dependent MPS approach which is used throughout this thesis is discussed. Lastly, Some remarks to improve the performance of the the variational optimization procedure are provided. In Chapter 5, we apply the MPS approach to investigate the electron dynamics in the core ionized silicon tetrafluoride molecule. Firstly, we demonstrate that the orbital ordering plays an important role in the performance of the MPS approach to describe the electron dynamics. Furthermore, we investigate the role of the numerical noise and show that this concept can enhance the efficiency of the MPS approach by improving the convergence rate of the dynamics in terms of the MPS bond dimension. In Chapter 6, we analyze the charge migration triggered by the ionization of the $2p$ orbital of the silicon atom in the silicon tetrafluoride. By performing analyses in terms of autocorrelation function and transition probability, we show how electronic correlation leads to intense and fast electron dynamics in the valence orbitals whereas the initial hole does not change during the process. Ultimately, we study the role of the nuclear geometry on the charge migration process and find out that considering a finite width of the nuclear wave function may lead to damping the charge

migration. In the end, a conclusion and an outlook on future directions of research is given in Chapter 7.

Ab Initio Quantum Chemistry

2

2.1 Introduction

Nowadays, quantum chemistry has become an essential tool for studying a wide variety of problems in chemistry and molecular physics. In quantum chemistry, quantum mechanical principles and equations are applied to chemical systems to provide the possibility to describe the governing mechanisms of this kind of system. But, since the molecular phenomena take place on atomic unit scales, appropriate quantum mechanical descriptions, which include all the necessary degrees of freedom and are optimized for performing on today's computational resources, are necessary.

Generally, there are two different computational approaches to describe the chemical phenomena. The first approach is so-called semiempirical methods [52–55] where some parameters from empirical data are widely used to approximate the Hamiltonian which describes the chemical system. In the second approach, ab initio quantum chemistry [56], only physical constants and interactions are considered in the calculation, and no experimental data is required. Although the ab initio methods are commonly more complicated and computationally more expensive due to their fundamental approach, they have become an essential tool in the study of atoms and molecules [57].

In this chapter, we will present some of the concepts, necessary approximations, and numerical techniques which are essential to describe the physical phenomena in molecular systems. We will start with the Born-Oppenheimer approximation which is widely applied in ab initio quantum chemistry to accelerate the computation of molecular wave function and other properties of molecular systems. Next, we will briefly review the Hartree-Fock method which is used to construct an optimal single-particle basis set in this thesis, and finally, we will discuss briefly the configuration interaction approach as a common method to approximate the many-body wave function in terms of possible excitations in the system to capture electronic correlations.

2.2 Born-Oppenheimer Approximation

One of the main goals in molecular quantum mechanic is to solve the *Schrödinger equation* to describe the molecules. If one is interested in the dynamical properties of the molecules, the *time-dependent Schrödinger equation* [58]

$$i\hbar\frac{\partial}{\partial t}\left|\psi(t,R,r)\right\rangle = \hat{H}\left|\psi(t,R,r)\right\rangle \tag{2.1}$$

should be considered.

In this equation, $|\psi(t,R,r)\rangle$ represents the time-dependent many-body wave function of the molecules where r and R denote the position of the electrons and nuclei in molecules respectively, $\hat{H}$ is the Hamiltonian of the system, and $\hbar$ is the reduced Planck constant.

If only the static properties of the molecule are of interest, then the *time-independent Schrödinger equation* would be easily obtained from Equation 2.1. Generally, solving the time-independent Schrödinger equation to find the ground state and ground state energy of the molecule and to determine the electronic structures of atoms and molecules is a remarkable part of quantum chemistry. There are plenty of methods to determine the ground state and first excited states of the molecules [59, 60], where some approximations have been utilized to simplify the underlying Schrödinger equation and make computations feasible.

One of the approximations which is widely used in *ab initio quantum chemistry* is called *Born-Oppenheimer approximation* [61, 62]. Within this approximation, the dynamic coupling between electronic and nuclear motion is neglected, and thereby one solves the electronic part of the Schrödinger equation while the nuclear positions are considered as fixed parameters. On the other hand, the resulting *potential energy surface* [1] provides the foundation for solving the nuclear motion.

[1] The relationship between the energy and the geometry of a chemical system is represented by a potential energy surface.

To review the Born-Oppenheimer approximation in more detail, let us first examine the molecular Hamiltonian in Equation 2.1 in terms of the kinetic and potential energy operators of the electrons and nuclei. The molecular Hamiltonian can be written as a sum of five terms.

1. The kinetic energy operators of the N_n nuclei in the system.

$$\hat{T}_n = -\sum_{i=1}^{N_n}\frac{\hbar^2}{2M_i}\frac{\partial^2}{\partial^2 R_i}\,. \tag{2.2}$$

2. The kinetic energy operators of the N_e electrons in the system.

$$\hat{T}_e = -\sum_{i=1}^{N_e} \frac{\hbar^2}{2m_e} \frac{\partial^2}{\partial^2 r_i} \,. \tag{2.3}$$

3. The potential energy between the electrons and nuclei or in other words, Coulomb interaction between electrons and nuclei in the system.

$$\hat{U}_{en} = -\sum_{i=1}^{N_n} \sum_{j=1}^{N_e} \frac{Z_i e^2}{4\pi\varepsilon_0 \left|R_i - r_j\right|} \,. \tag{2.4}$$

4. The potential energy emerging from Coulomb electron-electron interaction.

$$\hat{U}_{ee} = \sum_{i=1}^{N_e} \sum_{j>i}^{N_e} \frac{e^2}{4\pi\varepsilon_0 \left|r_i - r_j\right|} \,. \tag{2.5}$$

5. The coulomb interaction between the nuclei in the system.

$$\hat{U}_{nn} = \sum_{i=1}^{N_n} \sum_{j>i}^{N_n} \frac{Z_i Z_j e^2}{4\pi\varepsilon_0 \left|R_i - R_j\right|} \,. \tag{2.6}$$

Here M_i and Z_i are the mass and the atomic number of the nucleus i respectively, and m_e is the mass of the electron.

After introducing the molecular Hamiltonian in terms of the kinetic and potential energy operators, we are now in the position to examine the Born-Oppenheimer approximation. As we mentioned before, within this approximation we can neglect the coupling between the motion of the electrons and nuclei in the molecule or in other words, we can separate the Schrödinger equation into electronic and nuclei parts. The main reason for this simplification is based on the fact that the nuclei are much heavier than the electrons. It means, for the same amount of momentum the nuclei move much slower than the electrons.

From a mathematical point of view, the Born-Oppenheimer approximation separates the many-body wave function of the molecule in Equation 2.1 into an electronic and a nuclear many-body wave function. It means

$$|\psi(t, R, r)\rangle = |\psi(t, R, r)\rangle_e \cdot |\psi(t, R)\rangle_n \tag{2.7}$$

where $|\psi(t, R, r)\rangle_e$ is the electronic part and $|\psi(t, R)\rangle_n$ is the nuclear part of the many-body wave function. This enables us to separate the molecular Hamiltonian into electronic and nuclear terms. In addition, based on the

above-mentioned assumption, one can assume the electrons in a molecule to move in the field of the fixed nuclei and neglect the kinetic energy of the nuclei (Equation 2.2). Further, within this approximation, the repulsion between nuclei can be considered as a constant. Therefore, the electronic part of the molecular Hamiltonian in the Born-Oppenheimer approximation can be written as

$$\hat{H}_e = \hat{T}_e + \hat{U}_{ee} + \hat{U}_{en} + E_n \tag{2.8}$$

where E_n only depends on the fixed nuclei positions. It has to be mentioned that the electronic Hamiltonian in Equation 2.8 is responsible for the dynamics in the molecule on short time periods. It means the nuclear part of the many-body wave function on short time periods does not change and consequently, to study the dynamics in the molecules, only the electronic time-dependent Schrödinger equation

$$i\hbar\frac{\partial}{\partial t}\left|\psi(t,R,r)\right\rangle_e = \hat{H}_e\left|\psi(t,R,r)\right\rangle_e \tag{2.9}$$

should be solved. [2]

[2] In our study, the Born-Oppenheimer approximation restricts the time range we are able to describe. Light elements may begin to move on the time scale of femtoseconds as a response to electronic motion.

As the final point, we would like to mention that if one has solved the electronic problem, it is possible to investigate the motion of the nuclei under the same assumptions as used to formulate the electronic problem. As we have already mentioned, the electrons move much faster than the nuclei in the molecules. Therefore, one can consider the nuclei to move in the average field of the electrons which is described by the so-called nuclear Hamiltonian [63].

$$\hat{H}_n = \hat{T}_n + E_e(R) \tag{2.10}$$

where the nuclear kinetic energy is reintroduced and the electronic energy $E_e(R)$ represents the average field of the electrons which affects the nuclear motion in the molecule.

2.3 Hartree-Fock Method

In the previous section, we have seen that Born-Oppenheimer approximation leads to separation of the molecular many-body Schrödinger equation into an electronic and a nuclear part. For the reasons outlined above, solving the electronic part of the many-body Schrödinger equation is one of the main and

challenging problems in quantum chemistry and so far numerous methods have been developed to solve this equation approximately [20, 64–67] [3]. The simplest approach to the many-body problem is the *Hartree-Fock method*. This method is at the core of most approaches in quantum chemistry and that is why we will briefly present the concept of this method is the following.
The Hartree-Fock method is based on some assumptions. First, it is assumed that the many-body ground state of the molecule which consists of N electrons can be described in the form of a single Slater determinant

$$|\phi_0\rangle = |\chi_1\chi_2\cdots\chi_N\rangle \tag{2.11}$$

where χ represents a single electron orbital.
Secondly, a variational principle is employed to find approximate solutions of the Schrödinger equation. The variational principle states that any approximate wave function has energy above or equal to the exact ground state energy or in other words the best ground state wave function is the one that gives the lowest possible energy [60, 63].

$$E_0 = \langle\phi_0|H_e|\phi_0\rangle \tag{2.12}$$

where H_e is the electronic Hamiltonian in Equation 2.8. Based on the variational principle, we can obtain the optimal many-body wave function by varying its parameters, the single electron orbitals, until we minimize the energy. Doing so, the following equation determines the optimal single electron orbital

$$\hat{F}(r_1)\chi_i(r_1) = \epsilon_i\chi_i(r_1)\,. \tag{2.13}$$

This equation is called Hartree-Fock equation where ϵ_i is the energy eigenvalue associated with orbital χ_i and $\hat{F}(r_1)$ is called Fock operator which is defined as

$$\hat{F}(r_1) = \hat{h}(r_1) + \sum_j \int \chi_j^*(r_1)\frac{e^2}{4\pi\varepsilon_0\,|r_1 - r_2|}(1 - \hat{P}_{12})\chi_j(r_2)dr_2\,. \tag{2.14}$$

Here $\hat{P}_{12}$ is permutation operator and $\hat{h}(r_1)$ indicates the one electron Hamiltonian which consists of the kinetic energy of electron 1 and its potential energy in the field of the nuclei

$$\hat{h}(r_1) = \frac{-\hbar^2}{2m_e}\frac{\partial^2}{\partial^2 r_1} - \sum_{i=1}^{N_n}\frac{Z_i e^2}{4\pi\varepsilon_0\,|R_i - r_1|}\,. \tag{2.15}$$

[3] In the following, we will concentrate exclusively on the electronic part. That is why we will use the Schrödinger equation synonymous term for the electronic Schrödinger equation and omit the subscript $|.\rangle_e$.

The Hartree-Fock equation is an eigenvalue equation with the single electron orbitals as eigenfunctions and the energy of the single electron orbitals as eigenvalues. It is possible to solve this equation exactly for only atoms. For complicated systems such as molecules, it is common practice to introduce a set of single electron orbitals and solve the equation in the space spanned by the orbital basis set. It should be noted, in either case the solution depends on the orbital basis set. When we optimize the single electron orbitals, the Fock operator changes and it is necessary to solve Hartree-Fock equation *self-consistently*. It means, the Hartree-Fock equation as an eigenvalue problem should be solved iteratively until the Fock operator has converged. For this reason, the Hartree-Fock method is called a *self consistent field* (SCF) approach.

In the Hartree-Fock method, one of the most notable features of quantum mechanics, electronic correlations, are neglected. Considering a single Slater determinant to approximate the many-body wave function of the molecule leads to ignoring all the correlations in the system, and the many-body wave function obtained from the Hartree-Fock method is uncorrelated. Therefore, to take into account the electronic correlations in the molecules, it is necessary to go beyond the single determinant representation of the wave function. In the next section, a description of the *configuration interaction* (CI) as a *post-Hartree-Fock method* is given.

2.4 Configuration Interaction

As we have already mentioned, to capture the electronic correlation in the molecules it is essential to consider more than a single determinant to represent the many-body wave function and to go beyond the Hartree-Fock method to describe the electrons in molecules correctly. Therefore, a family of methods, namely, post-Hartree-Fock methods have been introduced to describe the electronic correlation in the molecules on the quantum mechanical level. In these methods, the molecular orbitals obtained from the Hartree-Fock approach are used as the starting point of the calculations, and corrections concerning excited states (which can be described by the Slater determinants) are introduced in the many-body wave functions of the molecules.

In this section, we would like to introduce one of the most popular post-Hartree-Fock methods, namely, configuration interaction. In this method, similar to the other post-Hartree-Fock methods, the Hartree-Fock ground state determinant (single Slater determinant defined in Equation 2.11) is considered, and to take

into account the electronic correlation, new Slater determinants in terms of electronic excitation are added. Such determinants can be constructed as the following.
Assume the Hartree-Fock ground state $|\phi_0\rangle$ where N electrons occupy the lowest molecular orbitals. Then, a singly excited determinant where one electron from the initially occupied orbital i has been promoted to one of the initially unoccupied orbitals a would be described as:

$$|\phi_i^a\rangle = \hat{c}_a^\dagger \hat{c}_i \, |\phi_o\rangle \tag{2.16}$$

where $\hat{c}$ and $\hat{c}^\dagger$ represent annihilation and creation operators respectively.

Similar to the singly excited, one can define doubly excited determinants in terms of the Hartree-Fock ground state and annihilation and creation operators.

$$|\phi_{ij}^{ab}\rangle = \hat{c}_a^\dagger c_b^\dagger \hat{c}_j \hat{c}_i \, |\phi_o\rangle \tag{2.17}$$

where two electrons have been promoted, one from orbital i to orbital a and another from orbital j to orbital b.

Further, one can consider higher order excited determinants in the system i.e. triply, quadruply, ..., n-tuply excited determinants. The number of all the possible determinants that can be considered is [63, 68]

$$\#\text{ possible determinants} = \binom{2L}{N} = \frac{(2L)!}{(2L-N)!N!} \sim \mathcal{O}([2L]^N) \, . \tag{2.18}$$

The many-body wave function in configuration interaction fashion can be expressed as a linear combination of all possible excitations

$$|\psi(t)\rangle = \alpha_0(t) \, |\phi_o\rangle + \sum_{ia} \alpha_i^a(t) \, |\phi_i^a\rangle + \sum_{ijab} \alpha_{ij}^{ab}(t) \, |\phi_{ij}^{ab}\rangle + \ldots \tag{2.19}$$

where the the many-body wave function includes the Hartree-Fock ground state, all singly excited or in other words *one-hole-one-particle* (1h1p) configurations, all doubly excited or *two-hole-two-particle* (2h2p) configurations and higher order excited configurations.

If one considers all the possible excitations to construct the many-body wave function, the result is a *full configuration interaction* (full CI) wave function. The full CI wave function can describe the system precisely, but it is computationally intractable for large systems. The main reason for this is that in the full CI

representation of the many-body wave function, the number of possible excited determinants grows rapidly as the number of basis set functions and electrons increases (see Equation 2.18). For this reason, truncation of the CI space according to the excitation level relative to the reference state is important to save computational resources. The most common approximation to truncate the CI wave function is called *configuration interaction singles and doubles* (CISD) where only single and double excitations, as well as the Hartree-Fock ground state, are considered. In this method, truncation of the CI space and ignoring higher order excitation leads to a significant reduction of the number of determinants that need to be taken into account. The total number of the determinants in this approximation is

$$\#\text{ determinants in CISD} = 2LN + \frac{N(N-1)(2L-N-1)(2L-N)}{4} \tag{2.20}$$

which is significantly smaller than the number of all possible determinants which should be considered in full CI. Note that in Equation 2.20, the first term shows the number of singly excited determinants, and the second term indicates the number of doubly excited determinants.

It is important to note that, the CI method is widely used in ground state [69–72] and time-dependent calculations [73–77]. In the time-dependent studies, there is an issue with selection of the excitations. In this method, to manage the computational resources, a large number of excited determinants which construct the many-body Hilbert space are removed regardless of the importance of those in dynamics. In other words, excited determinants which may play an important role in the dynamics may be artificially removed from the many-body Hilbert space. This restriction may induce large errors in the calculations especially when the governing dynamics in the system are unknown. That is why in the next chapter, we will outline an approach where a truncation of the Hilbert space has been done in a better suited manner to study time-dependent phenomena in molecules.

Matrix Product States

3

3.1 Introduction

In the pervious chapter, we have seen that the main challenge in the numerical study of molecules as quantum many-body systems is the large number of degrees of freedom. We have also seen that, in this kind of systems, the dimension of the Hilbert space (number of degrees of freedom) grows factorially with the system size. That is why exact diagonalization approaches (eg. Lanczos methods [78]) are strongly restricted to small system size. In addition, we have outlined a family of methods which are designed to simplify the representation of the many-body state. These methods are based on the concept that a limited number of Slater determinants is taken into account, to approximate the many-body state. In these methods, a specific form of the excitations is picked and the calculation is done using this reduced, but fixed Slater determinants. This can be problematic especially when properties are considered time-dependent. When the calculation of the time-dependent quantities is desired, it is possible that the excited determinants which represent the many-body state change with time. Therefore, the space of fixed excitations is not capable of describing the time-evolved many-body state efficiently as it may leave this space. There is a possibility that the excitations involved in the dynamics may change after some femtosecond.

To avoid this issue, we need an approach that simplifies the representation of the many-body state without cutting any excitations. In this approach, instead of the cutting configurations from the many-body Hilbert space, electronic correlations are considered and the entanglement from the many-body state dynamically is cut. Generally, not all electrons of a system are strongly correlated to each other, and cutting the Hilbert space regarding the correlation and entanglement can be a valid approximation. This approach is taken when representing the many-body state as a matrix product state [79–82].

In the following chapter, firstly, the matrix product state in the context of quantum chemistry will be introduced. Furthermore, we will introduce the area law to discuss the validity of the matrix product state approach in terms of the properties of the desired system. In addition, graphical representations

of the matrix product state will be introduced. The latter will make it easier to keep track of the multitude of matrices involved in the computations. Furthermore, matrix product operators will be introduced and discussed. Finally, symmetry adaption of the matrix product states will be discussed. Exploiting the symmetries of the quantum chemical Hamiltonian leads to a reduction of the dimension of the many-body Hilbert space and to a simplification of the matrix product state representation of the many-body state, leading to significant computational advantage.

3.2 Definitions and Properties

In quantum many-body physics, *Tensor networks* (TN) appear as a natural tool for representing quantum many-body states with a moderate number of parameters [83, 84]. This is realized via the compression of the originally large Hilbert space by limiting bond dimensions, while preserving relevant physics [85]. One of the most famous tensor network is the *matrix product states* (MPS), which is closely related to the *Density Matrix Renormalization Group* (DMRG) [24]. [1] As we mentioned before, an MPS is an efficient approximation for a general weakly-entangled quantum state. It has already been shown to be a successful approximation for one-dimensional systems in condensed matter physics [24, 88–92]. Nowadays, it has been widely used to investigate atomic or molecular systems [45, 93–98]. In the following, we introduce the idea behind it and discuss some of its properties.

[1] DMRG is a numerical variational method to obtain the ground state of many-body systems with high accuracy [24]. In the initial algorithm of DMRG which was proposed by White, the MPS approach does not directly appear. Later, people used MPS formulation to represent many-body states in DMRG variational algorithms [82, 86, 87].

The time-dependent many-body state of a molecule in Equation 2.19 can be rewritten in the occupation number representation of a basis of L orthonormal orbitals [45]:

$$|\psi(t)\rangle = \sum_{n_{1\uparrow}n_{1\downarrow}\cdots n_{L\uparrow}n_{L\downarrow}} c_{n_{1\uparrow}n_{1\downarrow}\cdots n_{L\uparrow}n_{L\downarrow}}(t)\,|n_{1\uparrow}n_{1\downarrow}\cdots n_{L\uparrow}n_{L\downarrow}\rangle\,, \tag{3.1}$$

where $n_{i\uparrow} \in \{0,1\}$ ($n_{i\downarrow} \in \{0,1\}$) is the number of up (down) electrons in the orbital i, the coefficient tensor [2] $c_{n_{1\uparrow}n_{1\downarrow}\cdots n_{L\uparrow}n_{L\downarrow}}(t)$ holds the time-dependent expansion coefficients, and $|n_{1\uparrow}n_{1\downarrow}\cdots n_{L\uparrow}n_{L\downarrow}\rangle$ are the occupation number basis states. The orbital basis may be molecular orbitals, atomic orbitals, or any other set of orthogonal orbitals. As we saw in the pervious chapter, the factorially growing number of possible determinants makes working with $|\psi(t)\rangle$ challenging, as it requires too many coefficients to store and handle for medium to large sets of orbitals. The coefficient tensor in Equation 3.1 can be exactly decomposed into a sequence of lower rank tensors by a *singular*

[2] It is a tensor of rank 2L.

value decomposition (SVD) [99]. In a first step, the coefficient tensor should be reshaped into a matrix:

$$c_{n_{1\uparrow}n_{1\downarrow}n_{2\uparrow}n_{2\downarrow}\cdots n_{L\uparrow}n_{L\downarrow}}(t) = c_{(n_{1\uparrow}n_{1\downarrow});(n_{2\uparrow}n_{2\downarrow}\cdots n_{L\uparrow}n_{L\downarrow})}(t). \tag{3.2}$$

Applying SVD on this matrix gives:

$$\begin{aligned} c_{(n_{1\uparrow}n_{1\downarrow});(n_{2\uparrow}n_{2\downarrow}\cdots n_{L\uparrow}n_{L\downarrow})}(t) = &\sum_{a_1} U_{(n_{1\uparrow}n_{1\downarrow});a_1}(t) S_{a_1;a_1}(t) \\ &\times V_{a_1;(n_{2\uparrow}n_{2\downarrow}\cdots n_{L\uparrow}n_{L\downarrow})}(t). \end{aligned} \tag{3.3}$$

By defining

$$A_{a_1}^{n_{1\uparrow}n_{1\downarrow}}(t) = U_{(n_{1\uparrow}n_{1\downarrow});a_1}(t) \tag{3.4}$$

$$\tilde{c}_{a_1;(n_{2\uparrow}n_{2\downarrow}\cdots n_{L\uparrow}n_{L\downarrow})}(t) = S_{a_1;a_1}(t) V_{a_1;(n_{2\uparrow}n_{2\downarrow}\cdots n_{L\uparrow}n_{L\downarrow})}(t) \tag{3.5}$$

and reshaping and decomposing $\tilde{c}_{a_1;(n_{2\uparrow}n_{2\downarrow}\cdots n_{L\uparrow}n_{L\downarrow})}(t)$ with a SVD as follows,

$$\tilde{c}_{a_1;(n_{2\uparrow}n_{2\downarrow}n_{3\uparrow}n_{3\downarrow}\cdots n_{L\uparrow}n_{L\downarrow})}(t) = \tilde{c}_{(a_1 n_{2\uparrow}n_{2\downarrow});(n_{3\uparrow}n_{3\downarrow}\cdots n_{L\uparrow}n_{L\downarrow})}(t) \tag{3.6}$$

$$= \sum_{a_2} U_{(a_1 n_{2\uparrow}n_{2\downarrow});(a_2)}(t) \tag{3.7}$$

$$\times \tilde{c}_{a_2;(n_{3\uparrow}n_{3\downarrow}\cdots n_{L\uparrow}n_{L\downarrow})}(t),$$

the coefficient tensor would be written as:

$$\begin{aligned} c_{n_{1\uparrow}n_{1\downarrow}n_{2\uparrow}n_{2\downarrow}\cdots n_{L\uparrow}n_{L\downarrow}}(t) = &\sum_{a_1 a_2} A_{a_1}^{n_{1\uparrow}n_{1\downarrow}}(t) A_{a_1;a_2}^{n_{2\uparrow}n_{2\downarrow}}(t) \\ &\times \tilde{c}_{a_2;(n_{3\uparrow}n_{3\downarrow}\cdots n_{L\uparrow}n_{L\downarrow})}(t), \end{aligned} \tag{3.8}$$

where $A_{a_1;a_2}^{n_{2\uparrow}n_{2\downarrow}}(t) = U_{(a_1 n_{2\uparrow}n_{2\downarrow});a_2}(t)$. The tensor $\tilde{c}_{a_2;(n_{3\uparrow}n_{3\downarrow}\cdots n_{L\uparrow}n_{L\downarrow})}(t)$ in Equation 3.8 can be reshaped and decomposed with a subsequent SVD. By repeating this procedure L-2 times, the coefficient tensor can be exactly rewritten as:

$$c_{n_{1\uparrow}n_{1\downarrow}\cdots n_{L\uparrow}n_{L\downarrow}}(t) = \sum_{a_1 a_2 \cdots a_{L-1}} A_{a_1}^{n_{1\uparrow}n_{1\downarrow}}(t) \cdots A_{a_{L-1}}^{n_{L\uparrow}n_{L\downarrow}}(t), \tag{3.9}$$

$$= A^{n_{1\uparrow}n_{1\downarrow}}(t) \cdots A^{n_{L\uparrow}n_{L\downarrow}}(t), \tag{3.10}$$

where $A^{n_{1\uparrow}n_{1\downarrow}}(t)$ is a row vector, $A^{n_{i\uparrow}n_{i\downarrow}}(t)$ for $1 < i < L$ is a matrix, and $A^{n_{L\uparrow}n_{L\downarrow}}(t)$ is also a column vector. In Equation 3.9, indices $n_{i\uparrow}n_{i\downarrow}$ correspond to physical indices which characterize a specific electron configuration in a molecular orbital. The other indices (a_i) correspond to virtual or bond indices which have no clear physical meaning. Figure 3.1 graphically represents the

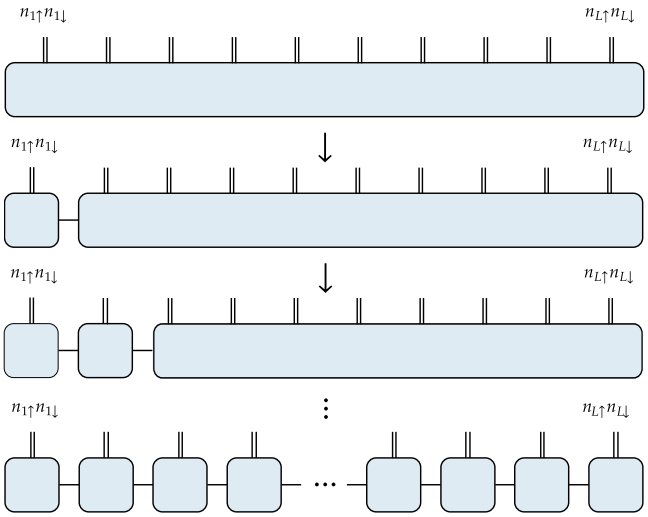

Figure 3.1: Graphical representation of an iterative construction of decomposed coefficient tensor by a sequence of singular value decompositions. Tensors are represented by rectangles, physical indices by open lines, and virtual indices by connected lines.

mentioned iterative construction of the decomposed coefficient tensor. As already shown, this sequence of matrix products reproduces the original coefficient tensor $c_{n_{1\uparrow}n_{1\downarrow}\cdots n_{L\uparrow}n_{L\downarrow}}(t)$. The preliminary advantage of this decomposition is storing all coefficients factorized in 4L vectors and matrices instead of storing them in a large tensor. There is no approximation behind this decomposition and such a decomposition is always possible by sequentially applying SVD on the coefficient tensor. The complete MPS representation of the many-body state is written as:

$$|\psi(t)\rangle = |\psi(t)\rangle_{MPS} \tag{3.11}$$

$$= \sum_{n_{1\uparrow}n_{1\downarrow}\cdots n_{L\uparrow}n_{L\downarrow}} A^{n_{1\uparrow}n_{1\downarrow}}(t)\cdots A^{n_{L\uparrow}n_{L\downarrow}}(t)\,|n_{1\uparrow}n_{1\downarrow}\cdots n_{L\uparrow}n_{L\downarrow}\rangle \tag{3.12}$$

including all Slater determinants $|n_{1\uparrow}n_{1\downarrow}\cdots n_{L\uparrow}n_{L\downarrow}\rangle$. At this point, there is no computational advantage compared to handling the coefficient tensor in Equation 3.1. The main idea of MPS is finding smaller matrices $\widetilde{A}^{n_{i\uparrow}n_{i\downarrow}}(t)$ that substitute for the decomposition matrices with little error. The smaller matrices can be made from the D largest singular values of $A^{n_{i\uparrow}n_{i\downarrow}}(t)$ ($S_{a_i;a_i}(t)$), decreasing the exponential scaling of the matrix dimension to some fixed value D. The dimension D of the reduced matrices is called the MPS bond or virtual dimension. This approach allows to reduce the dimension of the decomposition matrices, while the sequence of reduced matrix products $\tilde{A}^{n_{1\uparrow}n_{1\downarrow}}(t)\tilde{A}^{n_{2\uparrow}n_{2\downarrow}}(t)\cdots\tilde{A}^{n_{L\uparrow}n_{L\downarrow}}(t) \approx c_{n_{1\uparrow}n_{1\downarrow}\cdots n_{L\uparrow}n_{L\downarrow}}(t)$ still gives a quasi optimal representation of the coefficient tensor[100]. The singular value spectrum decays quickly in most physical situations, especially when the entanglement in $|\psi(t)\rangle$ is limited or short-ranged[82].

3.3 Entanglement and Area Law

In the previous section, we introduced the MPS approach as a sequential decomposition of the coefficient tensor in Equation 3.1 and we highlighted that by limiting the MPS bond dimension (D), the number of degrees of freedom could be reduced to an amount that does not increase exponentially with system size. This feature originates from a theory which is called *area law* [101]. The area law states that, for systems with short ranged-interaction and a gapped ground state, the *entanglement entropy* [3] between the respective ground states of two subsystems of the system is proportional to the area of the boundary between them. It means, only the intersection surface of the two subsystems has an influence on the entanglement entropy and the size of the subsystems does not directly affect it. However, a general state of the many-body Hilbert space does not obey the area law, by having an entanglement entropy scaling with the size of the two subsystems. For the ground state, one only wants to focus on states where the entanglement entropy is not dependent on the size of the subsystems. Considering states which obey the area law (area law states) leads to a significant reduction of the degrees of freedom for ground state calculations.

[3] Entanglement entropy is a quantity to measure the quantum entanglement for a many-body quantum state. The entanglement entropy between subsystems A and B of the system can be quantified by the von Neumann entropy $S_{A|B} = -\mathrm{Tr}_A\left[\rho_A \log \rho_A\right] = -\mathrm{Tr}_B\left[\rho_B \log \rho_B\right]$ where ρ_A (ρ_B) is the reduced density matrix of the quantum state for the respective subsystem A (B) [102].

For one-dimensional systems, the area of the boundary between two subsystems is constant and the area does not depend on the size of the subsystems. Therefore, regarding to the area law the entanglement entropy is constant too. Hence, ground states live in a manifold of the many-body Hilbert space which shows a constant entanglement entropy, and it frequently corresponds to a tiny corner of many-body Hilbert space. In other words, entanglement entropy of the gapped one-dimensional system is bounded by a constant and there is a particular bond dimension D where MPS can exactly represent the manifold of the area law state. By restricting the dimension of the matrix in the MPS, we neglect states which do not obey the area law and we reduce the computational cost to use the many-body state representation [47, 85].

As already mentioned, the area law is only valid for systems with short-ranged interaction and there is no guarantee that MPS with restricted bond dimension is a reliable representation of the many-body state of quantum chemical systems. For two reasons the Hamiltonian of quantum chemical systems has a long-ranged interaction. First, electron-electron interaction in different orbitals is inherently long-ranged and second, mapping delocalized molecular orbitals into the one-dimensional shape of a sequence of matrix products, makes the quantum chemical Hamiltonian a long-ranged one.

In addition, the area law does not make any assumptions about the time-evolution of the entanglement and it is limited to the gapped ground state. Therefore, in time-dependent conditions, there is the possibility that the many-body state leaves the part of the Hilbert space we are able to handle using MPS method. It means that by time evolving, systems may leave the part of the Hilbert space where MPS are unable to catch. This issue is called runaway error [33]. Although this seems like an acute problem and could restrict case study to the short-time behavior, there exist a couple of concepts to reduce the impact of that [47].

Despite the aforementioned points, MPS demonstrates high efficiency to deal on long-ranged systems as well as time-dependent situations. MPS has widely been used to study quantum chemical systems with long-range interaction to predict different physical properties ranging from ground states to excited states [103–108]. As well as long-ranged systems, MPS have been successful to characterize time-dependent many-body states ranging from condensed matter physics aspects [31, 33, 109–111] to quantum chemical phenomena [45, 108, 112–114].

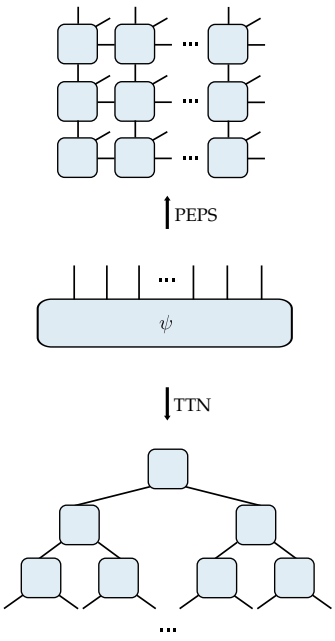

Figure 3.2: Conceptual tensor network decomposition of many-body state ψ in terms of two most famous ways, PEPS and TTN.

[4] The type of shapes does not have any physical meaning, and generelay different type of shapes have been used to discriminate tensors with different quantities. In this thesis we use rectangles to illustrate tensros.

3.4 Graphical Notation

As it has already been mentioned, the MPS approach is a special case of the more general concept of tensor networks. Tensor networks also cover high dimensional decomposition of the many-body state such as *projected entanglement pair states* (PEPS) [85, 115, 116], *tree-tensor networks* (TTN) [117–119], and *multi-scale entanglement renormalization ansatz* (MERA) [120, 121]. To give the reader an idea how these methods work, Figure 3.2 conceptually shows how the quantum many-body state ψ could be represented (or approximated) using tensor networks in different ways.

To be able to properly understand tensor network based algorithms, being familiar with the idea behind the tensor network concept and its notation is unavoidable. In addition, understanding the analytical formulas of tensor networks, due to the large number of indices and sums, is usually complicated and unclear. Thus, it is strongly recommended to use a graphical representation. Here, tensors are represented by shapes [4] and free indices are represented by lines which are called bonds in the following and connect to the shapes. Figure 3.3 illustrates tensors of various ranks. A scalar, or rank 0 tensor, has no free indices and can be represented by a rectangle without any connected

line. A vector, or rank 1 tensor, has one free index and can be represented by a rectangle with one connected line. A matrix, or rank 2 tensor, has two free indices and can be represented by a rectangle with two connected lines. Finally, a rank n tensor has n free indices and can be represented by a rectangle with n connected lines.

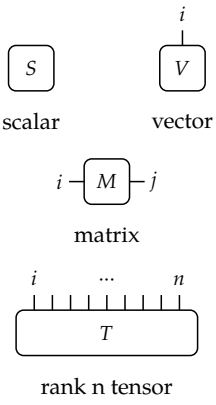

Figure 3.3: Graphical representation of a scalar, a vector, a matrix, and a rank n tensor. A scalar is depicted as a rectangle without any connected lines. A matrix is depicted as a rectangle whit one connected line. A vector is depicted as a rectangle with two connected lines, and a rank n tensor is depicted as a rectangle with n connected lines.

The graphical representation is extremely beneficial to show tensor operations. For example, the trace of a matrix can be expressed as

$$\mathrm{Tr}(M) = \sum_i M_{ii} = \quad , \tag{3.13}$$

where a closed bond represents a sum over an index. It is apparent that the result is a scalar, since it does not have any free bond. Another instructive example which could be visualized by this notation is matrix multiplication $C = A.B$

$$C_{ij} = \sum_k A_{ik} B_{kj} = \quad i \; A \; k \; B \; j \tag{3.14}$$

where the result of a matrix multiplication is again a matrix. There exist two open bonds and one closed bond.

In addition, the MPS representation of the many-body state (Equation 3.12) can be illustrated using the graphical notation as:

$$|\psi\rangle_{MPS} = \sum_{n_{1\uparrow} n_{1\downarrow} \cdots n_{L\uparrow} n_{L\downarrow}} \quad A[1] \; A[2] \; \cdots \; A[L] \quad |n_{1\uparrow} n_{1\downarrow} \cdots n_{L\uparrow} n_{L\downarrow}\rangle \tag{3.15}$$

where the sequence of matrix products $(A^{n_{1\uparrow} n_{1\downarrow}} A^{n_{2\uparrow} n_{2\downarrow}} \cdots A^{n_{L\uparrow} n_{L\downarrow}})$ is replaced with its graphical representation.

The squared norm of the many-body state in the MPS representation is defined as:

$${}_{MPS}\langle\psi|\psi\rangle_{MPS} = \sum_{n_{1\uparrow} n_{1\downarrow} \cdots n_{L\uparrow} n_{L\downarrow}} A^{*n_{1\uparrow} n_{1\downarrow}} \cdots A^{*n_{L\uparrow} n_{L\downarrow}} A^{n_{1\uparrow} n_{1\downarrow}} \cdots A^{n_{L\uparrow} n_{L\downarrow}} \tag{3.16}$$

and can be rewritten in the graphical notation as

$${}_{MPS}\langle\psi|\psi\rangle_{MPS} = \quad \begin{matrix} A[1] & A[2] & \cdots & A[L] \\ A[1] & A[2] & \cdots & A[L] \end{matrix} \quad . \tag{3.17}$$

In the above notation, the orthonormality of the occupation number basis and

the summation rule for the closed bonds were used. Also, since the result of ${}_{MPS}\langle\psi|\psi\rangle_{MPS}$ is a scalar, hence, there is no open bond in the graphical representation of the Equation 3.17.

3.5 Matrix Product Operator

Now we want to introduce the concept of a *matrix product operator* (MPO) and its similarity with the matrix product states. An MPO is an extension of a matrix product representation to operators [122].

By successive decomposition of the coefficients characterizing the operator, MPO generation can be performed equivalently to the MPS method. If we have an operator which is represented in occupation number basis

$$\hat{O}_{MPO} = \sum_{n_{1\uparrow}n_{1\downarrow}\cdots n_{L\uparrow}n_{L\downarrow}} O^{n_{1\uparrow}n_{1\downarrow}\cdots n_{L\uparrow}n_{L\downarrow}}_{n'_{1\uparrow}n'_{1\downarrow}\cdots n'_{L\uparrow}n'_{L\downarrow}} |n_{1\uparrow}n_{1\downarrow}\cdots n_{L\uparrow}n_{L\downarrow}\rangle\langle n'_{1\uparrow}n'_{1\downarrow}\cdots n'_{L\uparrow}n'_{L\downarrow}| \ , \tag{3.18}$$

then we can decompose the rank $4L$ tensor $O^{n_{1\uparrow}n_{1\downarrow}\cdots n_{L\uparrow}n_{L\downarrow}}_{n'_{1\uparrow}n'_{1\downarrow}\cdots n'_{L\uparrow}n'_{L\downarrow}}$ as a product of lower rank tensors like we did for an MPS. Therefore, the operator in the MPO representation can be written

$$\begin{aligned}\hat{O}_{MPO} &= \sum_{n_{1\uparrow}n_{1\downarrow}\cdots n_{L\uparrow}n_{L\downarrow}} O[1]^{n_{1\uparrow}n_{1\downarrow}}_{n'_{1\uparrow}n'_{1\downarrow}}\cdots O[L]^{n_{L\uparrow}n_{L\downarrow}}_{n'_{L\uparrow}n'_{L\downarrow}} |n_{1\uparrow}n_{1\downarrow}\cdots n_{L\uparrow}n_{L\downarrow}\rangle\langle n'_{1\uparrow}n'_{1\downarrow}\cdots n'_{L\uparrow}n'_{L\downarrow}| \\ &= \sum_{\substack{n_{1\uparrow}n_{1\downarrow}\cdots n_{L\uparrow}n_{L\downarrow}\\ n'_{1\uparrow}n'_{1\downarrow}\cdots n'_{L\uparrow}n'_{L\downarrow}}} \quad \cdots \quad |n_{1\uparrow}n_{1\downarrow}\cdots n_{L\uparrow}n_{L\downarrow}\rangle\langle n'_{1\uparrow}n'_{1\downarrow}\cdots n'_{L\uparrow}n'_{L\downarrow}| \ ,\end{aligned} \tag{3.19}$$

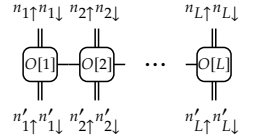

where (similarly to MPS representation) $O[1]^{n_{1\uparrow}n_{1\downarrow}}_{n'_{1\uparrow}n'_{1\downarrow}}$ is a row vector, $O[i]^{n_{i\uparrow}n_{i\downarrow}}_{n'_{i\uparrow}n'_{i\downarrow}}$ are matrices and, $O[L]^{n_{L\uparrow}n_{L\downarrow}}_{n'_{L\uparrow}n'_{L\downarrow}}$ is a column vector. The product of the matrices in Equation 3.19 precisely reconstructs the matrix elements of $O^{n_{1\uparrow}n_{1\downarrow}\cdots n_{L\uparrow}n_{L\downarrow}}_{n'_{1\uparrow}n'_{1\downarrow}\cdots n'_{L\uparrow}n'_{L\downarrow}}$. In other words, in prefect analogy to the non-truncated MPS representation of the many-body state (Equation 3.12), the MPO representation of the of a many-body operator is mathematically exact, and does not cause any error.

[5] Because most operators are extremely sparse

Although dealing with the many-body operators is not usually challenging [5], but bringing those to the MPO representation is beneficial. One of the advantages of the MPO is that it can be applied efficiently to a matrix product

state. For example, the application of a matrix product operator to a matrix product state is done as:

$$\begin{aligned}
\hat{O}_{MPO}\,|\psi\rangle_{MPS} &= \sum_{n_{1\uparrow}n_{1\downarrow}\cdots n_{L\uparrow}n_{L\downarrow}} \left(O[1]^{n_{1\uparrow}n_{1\downarrow}}_{n'_{1\uparrow}n'_{1\downarrow}} \cdots O[L]^{n_{L\uparrow}n_{L\downarrow}}_{n'_{L\uparrow}n'_{L\downarrow}} \right) \\
&\times \left(A[1]^{n'_{1\uparrow}n'_{1\downarrow}} \cdots A[L]^{n'_{L\uparrow}n'_{L\downarrow}} \right) |n_{1\uparrow}n_{1\downarrow}\cdots n_{L\uparrow}n_{L\downarrow}\rangle \qquad (3.20) \\
&= \sum_{\substack{n_{1\uparrow}n_{1\downarrow}\cdots n_{L\uparrow}n_{L\downarrow} \\ n'_{1\uparrow}n'_{1\downarrow}\cdots n'_{L\uparrow}n'_{L\downarrow}}} \left(O[1]^{n_{1\uparrow}n_{1\downarrow}}_{n'_{1\uparrow}n'_{1\downarrow}} A[1]^{n'_{1\uparrow}n'_{1\downarrow}} \right) \cdots \\
&\times \left(O[L]^{n_{L\uparrow}n_{L\downarrow}}_{n'_{L\uparrow}n'_{L\downarrow}} A[L]^{n'_{L\uparrow}n'_{L\downarrow}} \right) |n_{1\uparrow}n_{1\downarrow}\cdots n_{L\uparrow}n_{L\downarrow}\rangle \qquad (3.21) \\
&= \sum_{n_{1\uparrow}n_{1\downarrow}\cdots n_{L\uparrow}n_{L\downarrow}} B[1]^{n_{1\uparrow}n_{1\downarrow}} \cdots B[L]^{n_{L\uparrow}n_{L\downarrow}} |n_{1\uparrow}n_{1\downarrow}\cdots n_{L\uparrow}n_{L\downarrow}\rangle \qquad (3.22)
\end{aligned}$$

or in graphical notation:

$$\hat{O}_{MPO}\,|\psi\rangle_{MPS} = \sum_{n_{1\uparrow}n_{1\downarrow}\cdots n_{L\uparrow}n_{L\downarrow}}$$

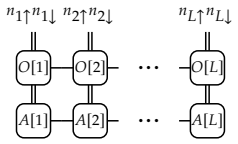

$$|n_{1\uparrow}n_{1\downarrow}\cdots n_{L\uparrow}n_{L\downarrow}\rangle \qquad (3.23)$$

$$= \sum_{n_{1\uparrow}n_{1\downarrow}\cdots n_{L\uparrow}n_{L\downarrow}}$$

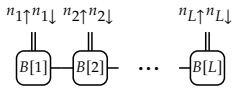

$$|n_{1\uparrow}n_{1\downarrow}\cdots n_{L\uparrow}n_{L\downarrow}\rangle \qquad (3.24)$$

where $B[i]^{n_{i\uparrow}n_{i\downarrow}} = \sum_{n'_{1\uparrow}n'_{1\downarrow}\cdots n'_{L\uparrow}n'_{L\downarrow}} O[i]^{n_{i\uparrow}n_{i\downarrow}}_{n'_{i\uparrow}n'_{i\downarrow}} A[i]^{n'_{i\uparrow}n'_{i\downarrow}}$. It is clear, by applying the MPO to a MPS that the form of the new MPS is invariant, but the matrix size was increased. It means that if the MPO representation of the many-body operator has a bond dimension of D_O and the MPS representation of the many-body state has bond dimension of D_A, then the resulting MPS has bond dimension of $D_O \cdot D_A$ which is tremendously larger than the initial bond dimension. [6] Here again, one can apply SVD on the resulting MPS to reduce the bond dimension, but the necessary truncation steps spoil the result of direct application of operators in MPO representation. For this reason, people use the variational operator application as a feasible solution to this issue [33, 45]. In the next chapter, we will introduce that and will show how one can apply an MPO to an MPS without increasing the bond dimension of the result.

[6] The MPO representation of the quantum chemical Hamiltonian scales like $\mathcal{O}(L^2)$ with system size L. On the other hand, the computational cost for operator application scales like $\mathcal{O}(LD_O^2D_A^2)$. Therefore, we acquire $\mathcal{O}(L^5D_A^2)$ as the cost for application of the Hamiltonian to the quantum many-body state [122].

3.6 Symmetry Adaption of Matrix Product States

Generally, symmetries of the physical systems play an important role in quantum mechanics. Considering the symmetries of the system enables us to write the many-body Hamiltonian of the system in a block diagonal form and thus to significantly reduce the dimension of the many-body Hilbert space. Consequently, it leads to a notable reduction of the required computational resources to store the data of the many-body state. Therefore, combining the symmetries of the molecular system with the MPS approach offers remarkable computational advantage. In the following section, we discuss how to exploit the symmetries of the molecular system to reduce the dimensionality of the many-body Hilbert space and therefore simplify the MPS representation of the many-body state.

When the Hamiltonian of a system is invariant under a symmetry generation operator $\hat{O}$, it has block-diagonal structure if it written in terms of eigenvectors of the operator $\hat{O}$. This is a result of

$$[\hat{H}, \hat{O}] = 0 \,. \tag{3.25}$$

The blocks of the Hamiltonian have associated quantum numbers (eigenvalues of the operator $\hat{O}$). These are called the good quantum numbers of the system. In general, a subspace of the many-body Hilbert space can be constructed by considering the many-body states with fixed symmetry quantum numbers. When one focuses on states with fixed quantum numbers, the many-body Hilbert space can be reduced to subspaces with a fixed quantum number. It is also worth to mention that the good quantum numbers of the system are conserved quantities and, in the time-evolution of the system, do not change with time. It means that if the initial state of the system is chosen from one of the subspaces (with fixed quantum numbers), the time-evolved state permanently remains in this subspace of the Hilbert space.

Essentially, the symmetry group of the molecular system Hamiltonian is $U(1) \otimes SU(2) \otimes P$ or in other words, electron number symmetry, total spin symmetry, and molecular point group symmetry [94]. It is worthwhile to note that the first mentioned symmetry is abelian whereas the second one is non-abelian and the last one, the molecular point group, can be either the abelian or non-abelian with respect to the corresponding symmetry operators.

As we discussed earlier, utilizing the symmetry of the system leads to reduction of the dimension of the many-body Hilbert space and consequently simplifies

the MPS representation of the many-body state. In the following, we want to discuss how the above-mentioned symmetry of the molecular Hamiltonian offers computational advantage in the MPS representation of the many-body state.

Let us start with the electron number symmetry. Since, the number of the electrons is conserved in the molecular system, the molecular Hamiltonian commutes with the total electron number operator.

$$[\hat{H}, \hat{N}] = [\hat{H}, \sum_i (\hat{n}_{i\uparrow} + \hat{n}_{i\downarrow})] = 0 \,. \tag{3.26}$$

Based on the above commutator, we can find a common basis for Hamiltonian and total electron number where the electron number operator is diagonal and the Hamiltonian is block diagonal. If one choses the occupation number basis which consists of eigenvectors of the total electron number operator to represent the Hamiltonian, then the Hamiltonian becomes block diagonal. Each block corresponds to a different number of the electrons in the system $\cdots, N-1, N, N+1, \cdots$ (see Figure 3.4). Generally, we can take advantage of the block diagonal structure of Hamiltonian to fix the number of electrons and thus only solve the block corresponding to that number, neglecting the other blocks.

By restricting the sum over all possible determinants in the complete many-body state to determinants where $\sum_i (n_{i\uparrow} + n_{i\downarrow}) = N$, one can use the total electron number symmetry to prune the complete many-body state.

$$|\psi(t)\rangle_N = \sum_{\substack{n_{1\uparrow} n_{1\downarrow} \cdots n_{L\uparrow} n_{L\downarrow} \\ \sum_i (n_{i\uparrow} + n_{i\downarrow}) = N}} c_{n_{1\uparrow} n_{1\downarrow} \cdots n_{L\uparrow} n_{L\downarrow}}(t) \, |n_{1\uparrow} n_{1\downarrow} \cdots n_{L\uparrow} n_{L\downarrow}\rangle \,. \tag{3.27}$$

Here, the second condition in the summation removes all the states with electron number unequal to N from the complete many-body state. Therefore, the many-body Hilbert space is reduced to the subspace where $\sum_i (n_{i\uparrow} + n_{i\downarrow}) = N$ is valid.

Furthermore, one can apply the electron number symmetry on the MPS representation of the many-body state to take its advantage. There is no restriction to choose the virtual basis to express the tensors $A[i]$ in Equation 3.15. Therefore, it is possible to write the MPS tensors in the basis of electron number eigenstates. If one expresses the MPS tensors in this basis, some

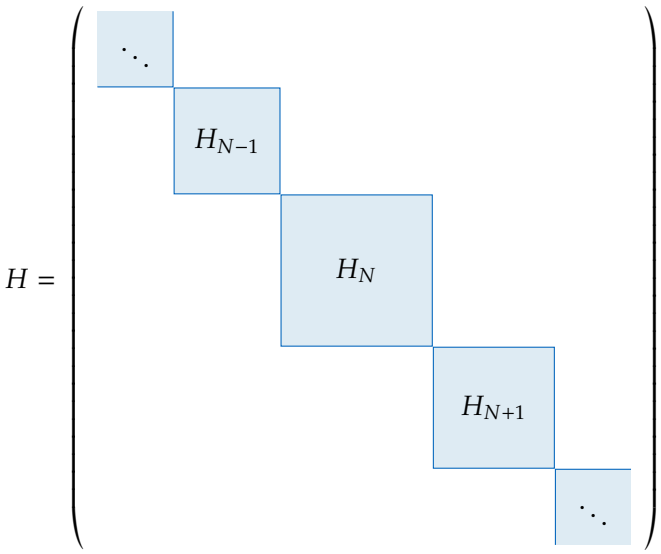

Figure 3.4: Graphical representation of the many-body Hamiltonian in the occupation number basis consisting of the eigenvectors of the total electron number operator. In this representation, the many-body Hamiltonian has block diagonal structure where each block corresponds to one respective eigenvalue of the electron number operator.

adaption in terms of the physical and virtual bonds are required as follows.

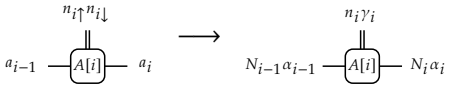

(3.28)

Here, N_i indicates the number of the electrons that occupy the orbitals 1 to i. $n_i \in \{0, 1, 2\}$ shows the occupation number of the orbital i. α_i and γ_i are the free indices. Note that γ_i includes the additional information about the orbitals such as spin and irreducible representation of the orbital i which will be discussed in future. So far, we have seen that to utilize the total electron number symmetry in MPS representation of the many-body state, the representation of the tensor $A[i]$ in the basis of electron number eigenstates is essential and it is not possible unless one makes adaptations of the physical and virtual bonds of the MPS tensors to the electron number basis. This adaptation leads to local electron number conservation in indices of the physical and virtual bonds. It means, the number of the electrons to the right of orbital i, N_i should be equal to sum of number of electrons in orbital i, n_i and number of the electrons to the left of orbital i, N_{i-1} i.e. $N_i = n_i + N_{i-1}$. This local conservation would be demonstrated in terms of the delta function straightforwardly.

$$A[i]^{n_i\gamma_i}_{N_{i-1}\alpha_{i-1},N_i\alpha_i} = A^{'}[i]^{n_i\gamma_i}_{N_{i-1}\alpha_{i-1},N_i\alpha_i}\delta_{N_i,n_i+N_{i-1}} \tag{3.29}$$

or in graphical notation:

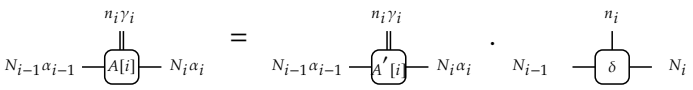

(3.30)

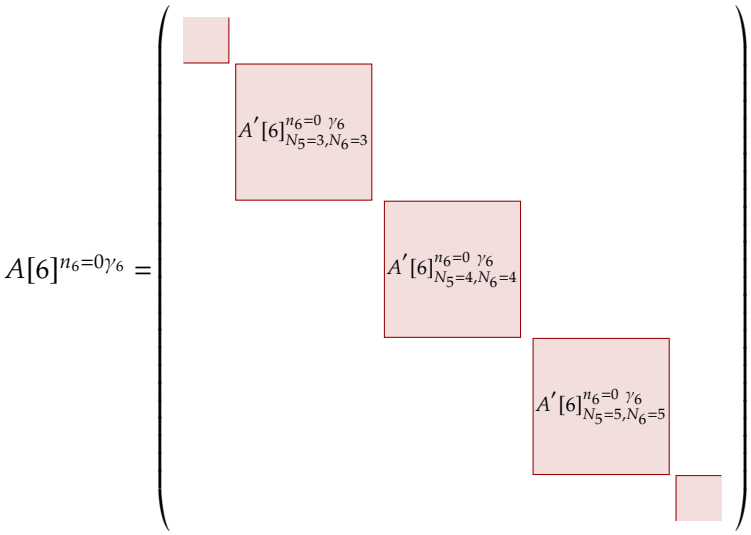

Figure 3.5: Schematic representation of the MPS tensor $A[6]^{n_6=0\gamma_6}$ in the electron number basis. According to Equation 3.29, this matrix has block diagonal structure. Using electron number symmetry provides the benefit that one only needs to store blocks A'.

For example, assume the situation where orbital $i = 6$ is empty ($n_6 = 0$) then according to Equation 3.29, the matrix element of the $A[6]^{n_6=0\gamma_6}$ at a given bond index is different from zero if $N_6 = N_5$. It means in this situation, the tensor $A[6]$ has block diagonal form where blocks consist of $A'[6]^{n_6=0\ \gamma_6}_{N_5,N_6}$ (see Figure 3.5). Generally, when one considers the electron number symmetry, the form of the MPS tensors $A[i]$ is simplified and it takes on a block structure. Therefore, to construct $A[i]$ it is only required to have non-zero elements $A'[i]$ which is computationally beneficial.

In addition to the electron number symmetry one can benefit from geometrical symmetry of the molecular system to reduce the subspace of the many-body Hilbert space and simplify the MPS representation of the many-body state. Generally, such a geometrical symmetry is described in terms of the symmetry point groups. A molecular symmetry point group consists of symmetry operations, which leave the molecular geometry invariant, and a binary operation, which describes the application of paired symmetry operations. These symmetry operations are for example n-fold rotational axis C_n, mirroring through a plain σ , and the identity operation E. If such symmetry operators do not commute with one another, then the corresponding molecular symmetry point group is non-abelian. In other words, in the non-abelian group, the result of applying paired symmetry operators depends on the order of operations. Usually, implementation of the non-abelian symmetries is more challenging and that is why in the CheMPS2 package [93] only abelian point group symmetries P with real-valued *character tables* are considered, i.e.

$$P \in \{C_1, C_i, C_2, C_s, D_2, C_{2v}, C_{2h}, D_{2h}\} \tag{3.31}$$

Therefore, all the symmetries which are exploited in the Hamburg CheMPS2 extension are abelian except for spin symmetry.

Before discussing the utilization of the point group symmetry in the MPS approach, let us introduce the concept of *irreducible representations* (irreps). As we previously mentioned, molecular geometries can be described in terms of a point group that consists of all operations that leave the form of the molecule invariant. Furthermore, electronic density, which is constructed from the molecular orbitals, follows the symmetry properties of the molecule. It means that the molecular orbitals are invariant under the operations of the point group of the molecule despite the fact that they are free to change their sign. In general, the molecular orbitals can be classified with respect to their behavior under operations of the point group of the molecule in terms of their irreps. For example, C_{2v} point group which includes the identity E, a two-fold rotation C_2 and two vertical mirroring symmetries at the xz plane $\sigma_v(xz)$ and yz plane $\sigma_v(yz)$ contains four irreps A_1, A_2, B_1, and B_2. As we noted the molecular orbitals with same irrep have similar behavior under the operations of the point group. For instance, the sign of the molecular orbitals with irrep A_1 under any operation of the C_{2v} point group does not alter or the sign of the molecular orbitals with irrep B_1 will be changed if C_2 operation or $\sigma_v(yz)$ are applied. The general behavior of the molecular orbitals with different irreps under the operations of the point groups is summarized in the character tables [123].

We know that the complete many-body state can be expanded in terms of the occupation number basis states and that the electronic density in the molecule obeys its geometrical symmetry properties. It means that the complete many-body state also follows the symmetry properties of the molecule or in other words, it can be attributed to a fixed irrep and, if it is only constructed from Slater determinants of one irrep, precisely behaves like an irrep. Generally, the irrep of the Slater determinant is depended on the direct product of the irrep of the orbitals which are singly occupied in the slater determinant. Consequently, the irrep I of Slater determinant $|n_{1\uparrow}n_{1\downarrow}\cdots n_{L\uparrow}n_{L\downarrow}\rangle$ is given by

$$I = \bigotimes_i \bar{I}_i \tag{3.32}$$

where the I_i represent the irrep of the single occupied orbital i. We have to note that the outcome of the multiplication of the different irreps of a symmetry point group is shown in the *multiplication table* [123] and one can extract the irrep of the given determinant by using these tables.

Similar to the electron number symmetry, exploiting the point group symmetry leads to a reduction of the complete many-body Hilbert space to a smaller subspace of it. It means, when the irrep of the many-body state is fixed, then sum over all possible determinants in Equation 3.27 reduces to the determinants which conform the irrep of the many-body state.

$$|\psi(t)\rangle_{NI} = \sum_{\substack{n_{1\uparrow}n_{1\downarrow}\cdots n_{L\uparrow}n_{L\downarrow} \\ \sum_i (n_{i\uparrow}+n_{i\downarrow})=N \\ \otimes_i I_i = I}} c_{n_{1\uparrow}n_{1\downarrow}\cdots n_{L\uparrow}n_{L\downarrow}}(t)\,|n_{1\uparrow}n_{1\downarrow}\cdots n_{L\uparrow}n_{L\downarrow}\rangle \tag{3.33}$$

Moreover, using the irrep of the many-body state results in decomposing the bond of the MPS tensor in terms of the irrep of the orbitals. It implies that if one utilizes the irrep of the many-body state, then the virtual and physical bonds of the MPS tensors should be adapted in terms of the irrep of the orbitals, and every bond gets an additional degree of of freedom which determines the irrep. This bond adaption together with the electron number degree of freedom can be illustrated as follows

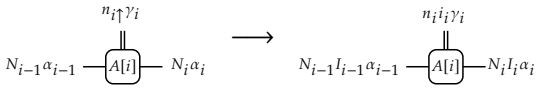

(3.34)

where, as before, γ_i is a free index which includes the information about the spin of orbital i.

Furthermore, after adaption of the virtual and physical bonds of the MPS tensors in terms of the irrep of orbitals, one can employ the delta function to represent the local conservation of the irrep of orbitals and simplify the representation of the MPS tensors $A[i]$ in Equation 3.29 as

$$A[i]^{n_i i_i \gamma_i}_{N_{i-1}I_{i-1}\alpha_{i-1},N_i I_i \alpha_i} = A^{'}[i]^{n_i i_i \gamma_i}_{N_{i-1}I_{i-1}\alpha_{i-1},N_i I_i \alpha_i} \delta_{N_i, n_i + N_{i-1}} \delta_{I_i, i_i \otimes I_{i-1}} \tag{3.35}$$

or in graphical notation:

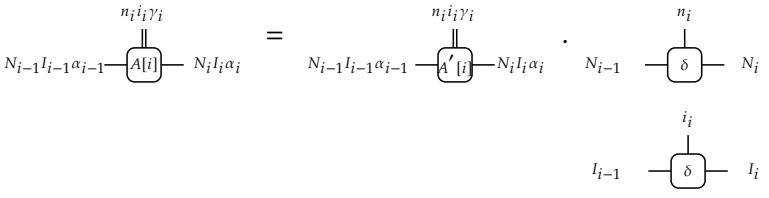

(3.36)

In this case, similar to the electron number symmetry, one can separate the MPS tensors $A[i]$ into the blocks that follow local conservation of the irrep of orbitals which is imposed by the delta function in Equation 3.35. For example,

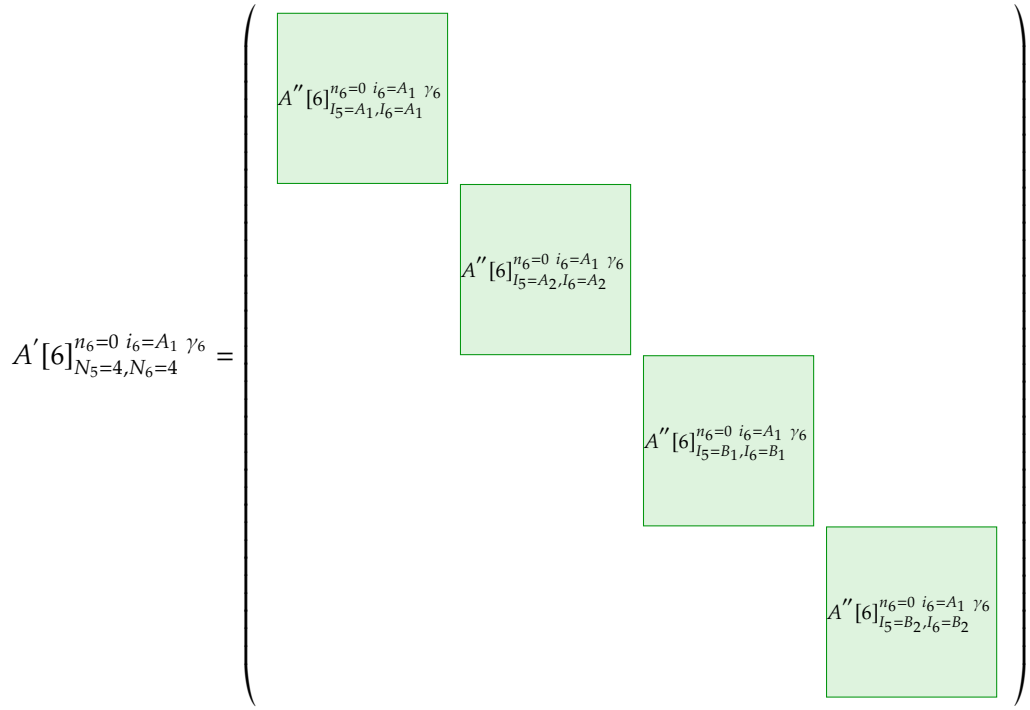

Figure 3.6: Schematic representation of the $A'[6]^{n_6=0\ i_6=A_1\ \gamma_6}_{N_5=4,N_6=4}$ Here, we assumed the given molecule exhibits the C_{2v} point group and orbital $i = 6$ belongs to the A_1 irrep which is the trivial irrep of the C_{2v} point group. Therefore, regarding to the local conservation of the irrep of the orbitals ($I_6 = i_6 \otimes I_5$) and multiplication table of the C_{2v} point group, it takes on a diagonal block structure.

Figure 3.6 shows the schematic representation of the $A'[6]^{n_6=0\ i_6=A_1\ \gamma_6}_{N_5=4,N_6=4}$, which is one of the symmetry blocks of $A[6]^{n_6=0\gamma_6}$ (see Figure 3.6). Here, we assumed the given molecule exhibits the C_{2v} point group and orbital $i = 6$ belongs to the A_1 irrep which is the trivial irrep of the C_{2v} point group. Therefore, regarding to the local conservation of the irrep of the orbitals ($I_6 = i_6 \otimes I_5$) and multiplication table of the C_{2v} point group with respect to the partial irreps left and right to this site, the MPS tensor $A'[6]^{n_6=0\ i_6=A_1\ \gamma_6}_{N_5=4,N_6=4}$ takes on a block diagonal structure.

So far, we have seen that utilizing two kinds of the abelian symmetries, electron number symmetry and symmetry of the molecule, results in a reduction of the many-body Hilbert space and consequently simplifies the representation of the entire many-body state. We have used the advantages of the corresponding quantum numbers which are conserved locally in MPS representation of the many-body state to reduce the complexity of the MPS representation and rewrite the MPS tensors $A[i]$ in terms of the blocks. In addition, to exploit the spin symmetry, one can take advantages of this fact that the quantum chemistry Hamiltonian commutes with all the spin operators and therefore the Hamiltonian and spin operators have common eigenstates. Thus, if one finds the eigenbasis of the spin operators S^2 and S_z and represents, the Hamiltonian in this basis, then it will have block diagonal structure where each block corresponds to one eigenvalue of the spin operators, respectively we stress again that, similarly to the electron number symmetry and molecular symmetry,

we can focus on the subspace of the many-body Hilbert space by using spin symmetry and representing the Hamiltonian in the spin operator eigenvector basis, but we should be aware of the fact that S_z is conserved locally while S^2 contains different orbitals.

As we have already mentioned, all the symmetries which are exploited in the Hamburg CheMPS2 extension are abelian except the spin symmetry. The implementation of non-abelian symmetries is challenging, and some tricks are required. In the CheMPS2 code, a theory by McCulloch and Gulacsi [124–126] is employed to implement the total spin symmetry. In this method, the *Wigner-Eckart theorem* [127, 128] is used to decompose the MPS tensors which have already been expressed in the eigenbasis of the spin operators. Therefore, utilizing this theory, one can straightforwardly write the virtual and physical bonds of the MPS tensors in terms of the eigenbasis of the spin operators as

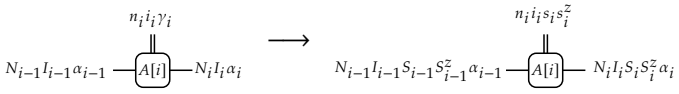

(3.37)

and decompose those in terms of the Wigner-Eckart theorem

$$A[i]^{n_i i_i s_i s_i^z}_{N_{i-1} I_{i-1} S_{i-1} S_{i-1}^z \alpha_{i-1}, N_i I_i S_i S_i^z \alpha_i} = A'[i]^{n_i i_i s_i}_{N_{i-1} I_{i-1} S_{i-1} \alpha_{i-1}, N_i I_i S_i \alpha_i} \delta_{N_i, n_i + N_{i-1}} \delta_{I_i, i_i \otimes I_{i-1}} \times \langle S_{i-1} S_{i-1}^z s_i s_i^z | S_i S_i^z \rangle \tag{3.38}$$

where $\langle S_{i-1} S_{i-1}^z s_i s_i^z | S_i S_i^z \rangle$ are the *Clebsch-Gordan coefficients* [129].

It is noteworthy that in Equation 3.38, the tensor $A'[i]$ does not depend on the spin projection quantum numbers which leads to the introduction of block-sparsity in MPS tensors and reduces their dimension remarkably.

Additionally, we have to mention that, if one considers all the symmetries of the quantum chemistry Hamiltonian, then the physical basis state of orbital i can be represented as [47, 130]

$$n_i i_i s_i s_i^z = \begin{cases} |n_i = 0, i_i = I_0, s_i = 0, s_i^z = 0\rangle \\ |n_i = 1, i_i = I_i, s_i = \frac{1}{2}, s_i^z = \frac{1}{2}\rangle \\ |n_i = 1, i_i = I_i, s_i = \frac{1}{2}, s_i^z = -\frac{1}{2}\rangle \\ |n_i = 2, i_i = I_0, s_i = 0, s_i^z = 0\rangle \end{cases} \tag{3.39}$$

where I_0 denotes the trivial irrep of point group P.

In this section we have seen that exploiting symmetries of the quantum chemistry Hamiltonian, namely electron number, the point group, and the total spin symmetry, provides a systematic method to simplify the MPS structure and reduces the dimension of the many-body Hilbert space of interest. Utilizing these symmetries makes it possible for us to define reduced MPS tensors where physical and virtual basis states are eigenstates of the electron number and spin operator as well as a fixed irrep.

Time-Evolution of Matrix Product States

4

4.1 Introduction

In the previous chapter, we have listed the different concepts of the MPS and seen how they can help us in representing many-body states. Also, we outlined their properties in terms of entanglement. Further, we saw how utilizing symmetries of the Hamiltonian simplifies the MPS structure and offers computational advantages. Now, in this chapter, we want to introduce time-evolution methods which can be utilized to find the dynamics of the many-body state using MPS representation.

The underlying differential equation to investigate the dynamics in the quantum systems is the time-dependent Schrödinger equation. It can be written for a many-body system in MPS representation:

$$i\hbar\frac{\partial}{\partial t}\left|\psi(t)\right\rangle_{MPS} = \hat{H}\left|\psi(t)\right\rangle_{MPS} \ . \tag{4.1}$$

The formal solution to this equation is given by applying the time-evolution operator. If the initial state at time t_0 is known, then the time-evolved state at time t is:

$$\left|\psi(t)\right\rangle_{MPS} = e^{\frac{-i}{\hbar}\hat{H}\delta t}\left|\psi(t_0)\right\rangle_{MPS} \tag{4.2}$$

where $\delta t = t - t_0$ and H is the time-independent Hamiltonian.

Generally, finding a representation of the time-evolution operator is not straightforward and it is still the main challenge in time-dependent quantum mechanics. Various methods have been developed to solve the time-dependent Schrödinger equation using the MPS approach [31, 33, 110], however, only a few can be applied to quantum chemical systems due to the long-range interaction.

In the following chapter, we would like to review some of these methods and in particular their disadvantages briefly and finally we will introduce the Krylov space time-evolution method. The latter is one of the general time-evolution methods to solve the time-dependent Schrödinger equation and is the heart of the time-dependent MPS approach that is used through this thesis. In Section

3.5, we have seen that the direct application of an MPO on an MPS results in a massive increase of the bond dimension of the yield MPS, and applying SVD is necessary to reduce the bond dimension of the resulting MPS. Although applying the SVD on the resulting MPS leads to a reduction of the MPS bond dimension, the truncation of the resulting MPS spoils the outcome of the direct application of operators in MPO representation. Thus, we need a more effective method to apply an MPO on an MPS where the bond dimension of the MPS representation of the resulting many-body state is limited without introducing significant error. Moreover, in the implementation of the time-evolution of the MPS, we need to perform other operations on the MPS and as we discussed before, performing this kind of operations naively is not efficient. For these reasons, we will discuss the variational optimization of matrix product states in more detail and finally, we will present some tricks to improve the performance of the variational method.

4.2 Krylov Space Time-Evolution of Matrix Product States

As we have already mentioned, there are a lot of methods which have been developed to solve the time-dependent Schrödinger equation that is presented in the MPS representation, but, due to the long-ranged interaction which is present in quantum chemical systems only a few of those can be applied in such systems.

For example, the *time-evolving block decimation* (TEBD) method [131], which is one of the most popular time-evolution methods used for MPS, is not applicable in quantum chemical systems. If one can write the Hamiltonian of the system in form of a sum of individual terms $\hat{H} = \sum_i \hat{h}_{i,i+1}$, then the corresponding time-evolution operator can be expressed approximately as product of local exponentials $e^{\frac{-i}{\hbar}\hat{h}_{i,i+1}t/2}$. This procedure is also known as *Lie-Trotter-Suzuki* [132, 133] decomposition of the time-evolution operator. Obviously, this decomposition is only possible if the Hamiltonian is short-ranged.

An alternative method for TEBD to deal with long-ranged interaction is the *time-dependent variational principle* (TDVP) [36, 134, 135] where the time-dependent Schrödinger equation is projected to the tangent space of the MPS manifold at the time [1] t and the resulting equation is solved for each individual tensor $A[i]$ in the MPS representation of the many-body state $|\psi(t)\rangle_{MPS}$. Finally, to obtain

[1] $\hat{H}\,|\psi(t)\rangle_{MPS}$ is not in the tangent space of the MPS manifold, and projecting this state to the MPS manifold ensures that the time-evolved state never leaves the manifold.

the time-evolved state, sweeps on the local sites of the system are required. It is worth mentioning that even thought this approach can be applied to long-ranged systems, its performance detracts for systems with non-local interaction [136].

The two methods mentioned above are originally developed for MPS. They use general properties of the tensor networks and operate on local tensors in MPS representation instead of treating total MPS. However, it has been shown that, discussed approaches are very efficient when studying systems with limited entanglement and electronic interaction [36, 134, 135, 137, 138]. In the recent years, those have been applied to chemical systems [42–44, 46, 139].

Another approach to handle time-evolution for quantum chemistry application is using general methods. In this approach, the special localized structure of the MPS representation is ignored and one can apply general time-evolution methods to the many-body wave function directly. Two of such methods, namely the *fourth-order Runge-Kutta* [2] approach and the *Krylov space* time-evolution, have already been implemented in Hamburg CheMPS2 extension code by Frahm [45, 47]. His studies showed that both methods are able to describe the dynamics of electrons following ionization in quantum chemical systems with reasonable accuracy. Also, he showed that the Krylov space time-evolution method brings more advantages in comparison with the fourth-order Runge-Kutta method, due to its unitarity properties [3]. Because of the considerable advantages of Krylov space time-evolution method and also its flexibility in the adaption to MPS, we use this method through this thesis. Therefore, we introduce it in more details in the following.

[2] The Runge-Kutta method [140, 141] is one of the methods for numerical solution of ordinary differential equations e.g. time-dependent Schrödinger equation. Of a multitude of higher and lower order Runge-Kutta methods, the fourth order method turns out to be the most efficient one.

[3] Runge-Kutta method is based on the finite expansion of the time-evolution operator in Equation 4.2. That is why it fails in non-unitarily performing time-evolution. Therefore, the norm of the time-evolved state is not conserved and will change with time. Due to the incurred error which scales like $\mathcal{O}(\delta t^5)$, a careful choice of the discrete time step size δt is critical for this method.

Krylov space time-evolution [142–145] is one of the general time-evolution methods to solve the time-dependent Schrödinger equation. This powerful method is based on Lanczos [146] reduction of the full many-body Hilbert space to a smaller vector subspace which is called Krylov space. This subspace is defined by the successive application of the Hamiltonian to the initial vector [147]. The many-body state in the MPS representation ($|\psi(t)\rangle_{MPS}$) is set as an initial state. In this case, the Krylov space of dimension N_K is defined as:

$$\mathcal{K} = span(\{|\psi(t)\rangle_{MPS}, \hat{H}|\psi(t)\rangle_{MPS}, \hat{H}^2|\psi(t)\rangle_{MPS}, \cdots, \hat{H}^{N_K}|\psi(t)\rangle_{MPS}\}). \tag{4.3}$$

Orthogonalization of the Krylov basis can be achieved by applying the *Gram-*

Schmidt procedure to the Krylov vectors in Equation 4.3

$$|\phi^{k+1}\rangle_{MPS} = \hat{H}\,|\phi^{k}\rangle_{MPS} - \sum_{j\leq k} \frac{{}_{MPS}\langle\phi^{j}|\,\hat{H}\,|\phi^{k}\rangle_{MPS}}{{}_{MPS}\langle\phi^{j}|\phi^{j}\rangle_{MPS}}\,|\phi^{j}\rangle_{MPS}\,. \tag{4.4}$$

The state evolved after a time step δt can be constructed as a superposition of the basis vectors of the Krylov space $|\phi^{k}\rangle_{MPS}$. In the following, we will try to show how one can derive the time-evolved MPS within the Krylov space.

Generally, the time-dependent many-body state (in MPS representation) can be projected onto the Krylov space as:

$$|\psi(t)\rangle_{MPS} = \sum_{k=0}^{N_K-1} a_k(t)\,|\phi^{k}\rangle_{MPS}\,. \tag{4.5}$$

Here, $a_k(t)$ are the time-dependent coefficients. This projection of the complete Hilbert space to a smaller Krylov space decreases the computational effort significantly. Time-evolution of the many-body state can be obtained by the solution of the Schrödinger equation in this reduced space. Inserting Equation 4.5 in the time-dependent Schrödinger equation (Equation 4.1) and multiplying both sides from the left with $\langle\phi_k|$, leads to an eigenvalue problem as:

$$i\hbar \sum_{k=0}^{N_K-1} {}_{MPS}\langle\phi^{j}|\phi^{k}\rangle_{MPS}\,\frac{\partial}{\partial t}a_k(t) = \sum_{k=0}^{N_K-1} a_k(t)_{MPS}\langle\phi^{j}|\,\hat{H}\,|\phi^{k}\rangle_{MPS} \tag{4.6}$$

which can be rewritten in the compact form

$$i\hbar S\frac{\partial}{\partial t}a = Ha \tag{4.7}$$

where overlap matrix S and Hamiltonian matrix H are defined as

$$S_{jk} = {}_{MPS}\langle\phi^{j}|\phi^{k}\rangle_{MPS} \tag{4.8}$$

$$H_{jk} = {}_{MPS}\langle\phi^{j}|\,\hat{H}\,|\phi^{k}\rangle_{MPS}\,. \tag{4.9}$$

The exact solution of Equation 4.7 is, of course

$$a(t) = \exp\left(-i\frac{\delta t}{\hbar}S^{-1}H\right)a(t_0). \tag{4.10}$$

By Substituting Equation 4.10 into Equation 4.5, it is possible to get the

time-evolved many-body state (in MPS representation).

$$|\psi(t)\rangle_{MPS} = \sum_{k=0}^{N_K-1} \exp\left(-i\frac{\delta t}{\hbar} S^{-1} H\right) a_k(t_0)\,|\phi^k\rangle_{MPS}\,. \tag{4.11}$$

Considering boundary conditions at initial time t_0 gives rise to $a_k(t_0) = \delta_{k,0}$. Therefore, Equation 4.11 can be written as

$$|\psi(t)\rangle_{MPS} = \sum_{k=0}^{N_K-1} \left[\exp\left(-i\frac{\delta t}{\hbar} S^{-1} H\right)\right]_{k,0} |\phi^k\rangle_{MPS} \tag{4.12}$$

where, $[.]_{k,0}$ denotes the elements at the k-th row and 0-th column of the exponential matrix.

We saw how one can construct the time-evolved many-body state in terms of Krylov vectors. Also, both approaches, using orthogonal and non-orthogonal basis, have advantages and disadvantages. For example, it has been shown that using non-orthogonal basis improves performance of the MPS time-evolution approach, but this improved performance is limited to special cases. Generally, if the initial Krylov vector is close to an eigenvector of the Hamiltonian, employing orthogonal Krylov vectors from Equation 4.4 is more stable. In this case, the non-orthogonal Krylov vectors tend to become linearly dependent, which causes a large numerical error when calculating the inverse of overlap matrix S^{-1} in Equation 4.12. Hence, time-evolution method based on the non-orthogonal Krylov vectors should be employed cautiously [45].

4.3 Variational Optimization of Matrix Product States

As we have already seen in Section 3.5, direct application of the MPO on the MPS leads to a significant increase in the dimension of the resulting MPS. It is also pointed out that we need to truncate the MPS to reduce the bond dimension of the resulting MPS which could induce huge error and spoil the result. In this section, we want to describe a more effective method to apply an MPO on an MPS. The method, we will introduce is based on the variational optimization of a many-body state in MPS representation, MPO applications are being performed while simultaneously the bond dimension of the MPS representation of the resulting many-body state is being limited.

Firstly, let us suppose application of the many-body operator $\hat{O}$ on many-body

state, in MPO and MPS representation respectively, results in a new many-body state i.e. $|C\rangle_{MPS} = \hat{O}\,|A\rangle_{MPS}$. Now, instead of performing the direct application followed by truncation, we try to seek the global minimum of the Lagrangian

$$\mathcal{L}[|C\rangle_{MPS}] = ||\,|C\rangle_{MPS} - \hat{O}\,|A\rangle_{MPS}\,||^2 \tag{4.13}$$

by variation of tensors in $|C\rangle_{MPS}$. In other words, we need to take the first derivative of the Lagrangian with respect of the tensor $C[i]^*$ in ${}_{MPS}\langle C|$ and set it to zero. Which means

$$\begin{aligned}\frac{\partial}{\partial C[i]^*}\mathcal{L}[C] = \frac{\partial}{\partial C[i]^*}\big(\,&{}_{MPS}\langle C|C\rangle_{MPS} - {}_{MPS}\langle C|\hat{O}|A\rangle_{MPS} \\ &- {}_{MPS}\langle A|\hat{O}^\dagger|C\rangle_{MPS} + {}_{MPS}\langle A|\hat{O}^\dagger\hat{O}|A\rangle_{MPS}\,\big) \\ &= 0\end{aligned} \tag{4.14}$$

Equation 4.14 can be simplified by ignoring terms not depending on $C[i]^*$, namely ${}_{MPS}\langle A|\hat{O}^\dagger|C\rangle_{MPS}$ and ${}_{MPS}\langle A|\hat{O}^\dagger\hat{O}|A\rangle_{MPS}$. Therefore one can write it in simpler form.

$$\frac{\partial}{\partial C[i]^*}\mathcal{L}[C] = \frac{\partial}{\partial C[i]^*}\big({}_{MPS}\langle C|C\rangle_{MPS} - {}_{MPS}\langle C|\hat{O}|A\rangle_{MPS}\big) = 0 \tag{4.15}$$

Solving Equation 4.15 leads to a minimization of the entire Lagrangian in Equation 4.13 with respect to $C[i]$, and then brings $|C\rangle_{MPS}$ close to the application of the many-body operator (in MPO representation) to the many-body state (in MPS representation), i.e. $\hat{O}\,|A\rangle_{MPS}$.

Now, with help of the graphical representation, we can understand the derivative in Equation 4.15 more clearly.

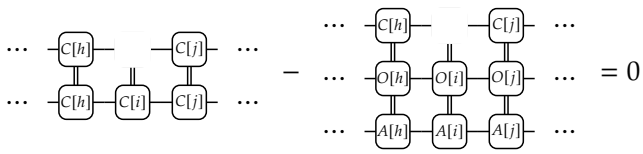

$$= 0 \tag{4.16}$$

where the first sector shows $\frac{\partial}{\partial C[i]^*}\big({}_{MPS}\langle C|C\rangle_{MPS}\big)$ and the second sector shows $\frac{\partial}{\partial C[i]^*}\big({}_{MPS}\langle C|\hat{O}|A\rangle_{MPS}\big)$. Here, due to linear dependency of Equation 4.15 on tensor $C[i]^*$, it disappears when taking the derivative of Equation 4.15.

To solve Equation 4.16, it is beneficial to use the *canonical forms* of MPS representation [82]. One can take advantage of the canonical forms of MPS

representation, which include *(left-) right-normalized matrices* to simplify the first sector of Equation 4.16. Let us assume all matrices located on the left side of the orbital i are left-normalized and all matrices located on the right side of the orbital i are right-normalized. In other words, we assume the MPS $|C\rangle_{MPS}$ is represented in the mixed-canonical form. Therefore, regarding to the *mixed canonical* form of MPS representation, we can simplify Equation 4.16 to

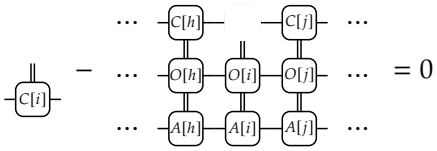

$$= 0 \tag{4.17}$$

which can be rearranged to

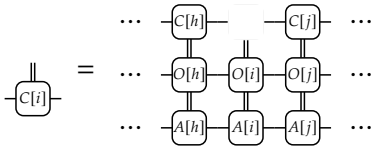

$$= \tag{4.18}$$

Here, we used normalization properties of the many-body state in MPS representation to convert Equation 4.15 to the linear equation Equation 4.18. Generally, one can find the minimum of the Lagrangian in Equation 4.13 for the specific tensor $C[i]$ by solving Equation 4.18.

In general, it is very likely that solving Equation 4.18 does not lead to finding the global minimum of the Lagrangian in Equation 4.13. The reason is that the solution of Equation 4.15 for one of the orbitals, namely orbital i, depends on the other tensors. To avoid getting stuck in a local minimum and approach the global minimum, it is essential to also optimize the other tensors in the MPS $|C\rangle_{MPS}$. In the Hamburg CheMPS2 extension code, this is done in the form of *sweeps*, [4] where the process performed on orbital i should be repeated for the next tensor $i+1$ in the MPS $|C\rangle_{MPS}$ and all following. In this way, until one reaches convergence to the desired accuracy, MPS $|C\rangle_{MPS}$ is optimized variationally. It should be noted that the bond dimension of the MPS $|C\rangle_{MPS}$, in contrast to the direct application, does not change during the optimization process. That is why the optimization performed in the fixed manifold of a many-body Hilbert space which makes this procedure more efficient compared to the direct application.

In addition, this procedure enables us to also perform other operations. Mainly, we can use the variational method to add two or even more MPS in a single optimization step. For example, the Lagrangian which corresponding to the

[4] The concept of the sweep is firstly introduced in DMRG variational algorithm[24]. In this algorithm, one makes effort to minimize the Lagrangian

$$\mathscr{L}[\psi] = \langle\psi|\hat{H}|\psi\rangle - \lambda\,\langle\psi|\psi\rangle$$

to find the ground state. Sweeping procedure is an essential part of the variational algorithm to find the minimum of the above Lagrangian.

sum of two many-body states in MPS representation $|A\rangle_{MPS}$ and $|B\rangle_{MPS}$ reads

$$\mathscr{L}[C] = || \, |C\rangle_{MPS} - (|A\rangle_{MPS} + |B\rangle_{MPS})||^2 \tag{4.19}$$

Here, seeking the global minimum of the Lagrangian in Equation 4.19 leads to a procedure that is again similar to what was explained earlier for the operator application. In other words, for adding two MPS, the linear equation to solve is given by

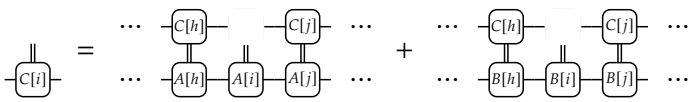

(4.20)

Here, analogously to the operator application, the normalization property of the many-body state in MPS representation is used to simplify the left hand side of Equation 4.20. Also, employing sweeps is required to make sure to approach global minimum. Another benefit of the variational approach is that it allows to combine different operations into one. For instance, in the time-evolution methods that have been covered in Section 4.2, combinations of the operator applications with sums of MPS appear frequently. To handle this kind of combination of simultaneous operations , one needs to minimize a more complicated Lagrangian such as

$$\mathscr{L}[C] = || \, |C\rangle_{MPS} - \left(\hat{H}^N \, |p\rangle_{MPS} + \sum_q |q\rangle_{MPS}\right)||^2 \tag{4.21}$$

with respect the tensor $C[i]^*$ in $|C\rangle_{MPS}$. Furthermore, variational optimization introduces a small computational cost compared to direct application. For instance, the complexity of adding two MPS with bond dimension D in the variational method is $\mathcal{O}(LD^3)$ per sweep, and the complexity of applying of the MPO in quantum chemistry to an MPS is $\mathcal{O}(L^4D^2 + L^3D^3)$ per sweep [94] which is one order smaller in system size (L) compared to the direct application (see Section 3.5).

4.4 Improvement of Variational Optimization Procedure

As we have already noted, the variational optimization procedure used to minimize the Lagrangian mentioned above (for example Lagrangian in Equation

4.21) is similar to the DMRG variational algorithm. In DMRG algorithm one makes effort to minimize a Lagrangian to obtain the ground state energy. Additionally, it has been shown that if the MPS bond dimension D is inadequately large, the DMRG algorithm can get stuck in a local minimum [148]. On the other hand, we know that the bond dimension cannot be increased indefinitely in practice. Therefore, it is important to utilize some strategies to increase the performance of the variational optimization procedure. Since the latter is similar to the DMRG algorithm, we can implement the strategies normally used to enhance the performance of the DMRG algorithm. Therefore, in the following we will describe some considerations to improve the variational optimization algorithm.

4.4.1 Two-Site Object

So far, we described the optimization procedure of a *one-site object* (optimization with respect to the single tensor $C[i]$) , however, in the the Hamburg CheMPS2 extension code the optimization procedure has been implemented with respect to *two-site objects*. It means, instead of taking the derivative with respect to a single tensor $C[i]^*$, pairs of neighboring tensors e.g. $C[i]^* C[i+1]^*$ are employed in the variational optimization procedure. This approach was inspired by the two-site DMRG algorithm [88, 94] which has better performance in comparison to the one-site version due to larger variational freedom [130, 149].

In the MPS formalism a two-site object or in other words, two-site tensor can be constructed as [5]

$$S[i,i+1]^{n_{i\uparrow} n_{i\downarrow} n_{i+1\uparrow} n_{i+1\downarrow}}_{a_{i-1};a_{i+1}} = \sum_{a_i} C[i]^{n_{i\uparrow} n_{i\downarrow}}_{a_{i-1};a_i} \; C[i+1]^{n_{i+1\uparrow} n_{i+1\downarrow}}_{a_i;a_{i+1}} \tag{4.22}$$

which is illustrated using graphical notation as [6]

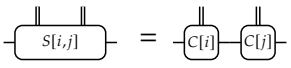

(4.23)

For example, if one wants to find the global minimum of the Lagrangian in Equation 4.13 in two-site object fashion, the first derivative with respect to the $S[i,j]^*$ should be taken. This means,

$$\frac{\partial}{\partial S[i,j]^*} \mathcal{L}[S] = \frac{\partial}{\partial S[i,j]^*} \left({}_{MPS}\langle C|C\rangle_{MPS} - {}_{MPS}\langle C|\hat{O}|A\rangle_{MPS} \right) = 0 \tag{4.24}$$

should be solved to obtain the global minimum of the corresponding Lagrangian. Similar to Equation 4.18, Equation 4.24 can be illustrated in the

[5] Without loss of generality, we ignore the symmetry adaption of the physical and virtual basis of the MPS tensors in the following.

[6] For simplicity, we assume $j = i+1$

graphical representation.

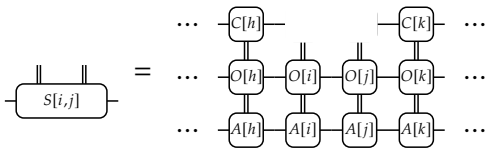

(4.25)

Here, analogous to the process that gave rise to the Equation 4.18 and Equation 4.20, we use the normalization property of an MPS to simplify the right-hand side of Equation 4.25. Also, similar to the one-site case, solving the resulting linear equation leads to a minimization of the Lagrangian. It is important to clarify that by constructing a two-site tensor $S[i,j]^{n_{i\uparrow}n_{i\downarrow}n_{j\uparrow}n_{j\downarrow}}_{a_i;a_j}$ in Equation 4.22, the number of degrees of freedom increases four times in comparison to the one-site case. This is due to the unrestricted combination of the physical indices $n_{i\uparrow}n_{i\downarrow}$ and $n_{j\uparrow}n_{j\downarrow}$. After solving the linear equation, the two-site tensor has to be factorized into two one-site object to recover MPS form. This can be done using the SVD of $S[i,j]^{n_{i\uparrow}n_{i\downarrow}n_{j\uparrow}n_{j\downarrow}}_{a_{i-1};a_j}$ as

$$S[i,j]^{n_{i\uparrow}n_{i\downarrow}n_{j\uparrow}n_{j\downarrow}}_{a_{i-1};a_j} = \sum_{\kappa} U_{(a_{i-1}n_{i\uparrow}n_{i\downarrow});\kappa}\lambda_{\kappa;\kappa}V^{\dagger}_{\kappa;(n_{j\uparrow}n_{j\downarrow}a_j)} \tag{4.26}$$

$$= \sum_{\kappa} C[i]^{n_{i\uparrow}n_{i\downarrow}}_{a_{i-1};\kappa}\lambda_{\kappa;\kappa}C[j]^{n_{j\uparrow}n_{j\downarrow}}_{\kappa;a_j} \tag{4.27}$$

4.4.2 Numerical Random Noise

Although the two-site procedure of variational operations improves the overall MPS performance, it is still possible that this algorithm gets stuck in a local minimum. To help protect the two-site algorithm from this problem, it is suggested to use numerical noise [148, 150]. [7] In Section 3.6 we have seen that if one considers symmetries of the molecular system and combines these symmetries with the MPS approach, then MPS tensors $A[i]$ in the MPS representation of the many-body state can be constructed as a block matrix where each block is associated with a certain quantum number of the system. On the other hand, from the pervious section we know that the two-site object $S[i,j]$ is easily constructed from one-site tensors (see Equation 4.22). Hence, two-site object $S[i,j]$ also can be interpreted as block matrix. During sweep procedure, it is most likely that some of the symmetry blocks are lost and cannot be restored easily, due to the self-consistent nature of the sweeping stage in the variational optimization algorithm. Therefore, it is urgent to add a small amount of noise to $S[i,j]$ at each step just before it is decomposed in order to restore the missing symmetry block in the last step

[7] Employing numerical noise is also beneficial to improve one-site algorithm [149], but since calculations throughout this thesis are based on two-site algorithms, we will focus on the application of numerical noise in two-site algorithms.

of the sweep procedure. Nowadays, the numerical noise concept mentioned above is widely used to enhance the performance of the DMRG algorithms and consequently its convergence rate [151–155]. Thus, we expect that adding noise improves the performance. The effect of random noise on the performance of the optimization procedure as the heart of the time-dependent MPS approach will be discussed practically in the next chapter.

In the Hamburg CheMPS2 extension code, a small random number is used as noise to improve the optimization procedure. This noise is bounded in magnitude by 0.5 γ_{noise} where γ_{noise} is the noise prefactor and defines the amplitude of the noise added.

4.4.3 Sweep Schedule and Consecutive Instructions

In addition to the two-site tensor and adding numerical random noise, performing sweeps with different parameters can help to increase the efficiency of the variational optimization procedure. For example, it is predicted that if one chooses the noise amplitude too large, it is possible that the procedure is not able to find an optimal MPS, therefore it is important to reduce the noise to a small value or turn it off during the last few sweeps [156]. Further, it is suggested that using small bond dimensions in the initial sweeps and then increasing it in the later ones speeds up convergence [157].

For these reasons, to ensure obtaining converged results, sweep schedule with different MPS bond dimension and numerical noise is commonly employed in DMRG based calculations [93, 151, 155, 158–161]. In the CheMPS2 code, this procedure is accounted for in terms of the *consecutive instructions* where each instruction contains a number of sweeps, the MPS bond dimension, and the noise prefactor.

For instance, the calculations throughout this thesis are done with three instructions where the first contains one sweep and second and last one

	Instruction 1	Instruction 2	Instruction 3
Number of Sweeps	1	2	2
Bond Dimension	D	D	D
Noise Prefactor	γ_1	γ_2	γ_3

Table 4.1: The sweep schedule used throughout this thesis. The calculations are done with three instructions where the first contains one sweep and second and last one include two sweeps. We fix the bond dimension D to be the same for all the instructions whereas the noise prefactor γ_{noise} is variable through the different instructions

include two sweeps. It should be noted that we fix the bond dimension D to be the same for all the instructions whereas the noise prefactor γ_{noise} is variable and will be reported as noise prefactor = $\gamma_1, \gamma_2, \gamma_3$ wherever it is necessary. The sweep schedule used throughout this thesis is summarized in Table 4.1.

5 Numerical Aspect of Electron Dynamics in Core Ionized Silicon Tetrafluoride

5.1 Introduction

After we have introduced the concept and properties of the MPS representation of the many-body states in quantum chemical systems and discussed the time-evolution of MPS, especially the variational optimization approach and the parameters and properties that can improve its performance, we are now in the position to apply our understanding of the MPS approach to treat the correlated electron dynamics in a molecule that has been ionized.

In this chapter, we apply the MPS approach to study electron dynamics in the silicon tetrafluoride, SiF_4 molecule. We investigate the ionization of the core orbital of silicon tetrafluoride, namely the $2p$ orbital of the silicon atom. To assess the validity of the resulting dynamics, it is necessary to do the convergence test in terms of the MPS bond dimension. In other words, we should vary the bond dimension, to ensure that the dynamics is stable in terms of the Hilbert space covered by the MPS representation. Firstly, we perform the convergence test for two kinds of the ordering of the orbitals, namely orbital ordering based on the irreducible representations and based on the so-called Fiedler vector of the exchange matrix. Afterwards, we discuss how the ordering of the orbitals based on the Fiedler vector leads to an enhanced convergence rate of the MPS approach in terms of the bond dimension. Unlike the ordering based on the irreducible representations, the MPS bond dimensions within a computationally accessible range are sufficient to resolve the dynamics. Finally, we investigate the role of numerical noise and orbital ordering in the resulting dynamics as another critical parameter in the performance of the MPS approach.

5.2 Electron Dynamics in Core Ionized Silicon Tetrafluoride

Silicon tetrafluoride has tetrahedral molecular geometry, where silicon is the central atom and four fluorine atoms are located at the corners of a tetrahedron (see Figure 5.1). With a tetrahedral structure, silicon tetrafluoride has T_d point group symmetry, which is a non-abelian symmetry group. As we have already mentioned, the Hamburg CheMPS2 extension is only able to support abelian points groups, therefore, the molecule is described in terms of one of its abelian subgroups C_{2v}. Furthermore, we employ an effective core potential, as it is widely used to decrease the number of the active electrons treated in the ab initio calculations [23, 57, 162–165], to describe core electrons of fluorine atoms. In this study, we use the Stuttgart/Cologne pseudopotential [166], where 2 electrons from each of the fluorine atoms are removed. We also use the associated Gaussian basis sets for the fluorine atoms, that were designed particularly for the desired effective core potential, and the so-called 6-31G basis set [167] for silicone atom. Consequently, we describe the silicone tetrafluoride molecule using 42 electrons in a set of 45 orbitals.

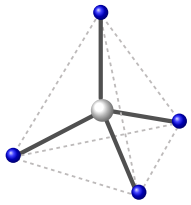

Figure 5.1: Silicon tetrafluoride molecule at its equilibrium geometry. Silicon tetrafluoride has tetrahedral molecular geometry, where silicon is the central atom and four fluorine atoms are located at the corners. The geometry is optimized on the Hartree-Fock level, using the Stuttgart/-Cologne pseudopotential and associated Gaussian basis set for the fluorine atoms and 6-31G basis set for silicon atom.

The starting point of our study is the neutral silicon tetrafluoride molecule in its Hartree-Fock (uncorrelated) ground state $|\phi_0\rangle$. To perform the SCF calculation on the Hartree-fock level and obtain molecular orbitals as well as an optimized molecular geometry, we use the quantum chemistry program package Molpro[168]. In this case, there are only two parameters to optimize, the Si-F distance ($\overline{SiF}$) and the F-Si-F bond angle ($\widehat{FSiF}$). Performing geometry optimization on the Hartree-Fock level with the above mentioned effective core potential and basis sets results in $\overline{SiF} = 1.62$Å and $\widehat{FSiF} = 109.47°$. Figure 5.1 represents the SiF_4 molecule at equilibrium geometry.

To prepare the initial state, we suddenly remove one electron from the $2p$ orbital of the silicon atom in SiF_4 on Hartree-Fock level as follows:

$$|\psi(t_0)\rangle = \hat{c}_{Si_{2p}} |\phi_0\rangle \tag{5.1}$$

Here, $\hat{c}_{Si_{2p}}$ indicates an annihilation operator that annihilates one electron from the $2p$ orbital of the silicon atom. $|\phi_0\rangle$ denotes the Hartree-Fock ground state of SiF_4. It is important to note that, in the numerical calculation of this chapter, we chose the hole to be created in $2p$ orbital with irreducible representation A_1, which can be assigned to the p_z orbital, whereas creating a hole in the degenerate orbitals with irreducible representation B_1 and B_2 that can be

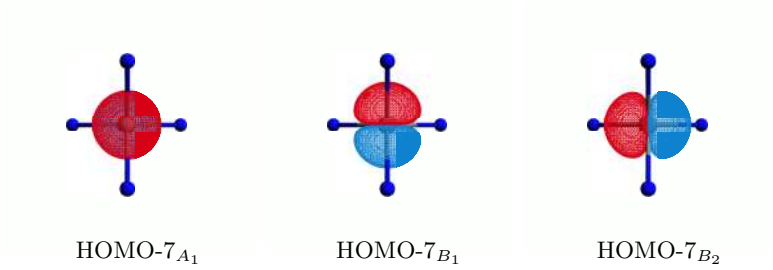

Figure 5.2: Hartree-Fock Molecular orbitals of SiF_4 which correspond to the $2p$ orbitals of the silicon atom with different angular momenta. Molecular orbitals with different angular momentum can be assigned to the different irreducible representations of the C_{2v} point group. For example, HOMO-7$_{A_1}$, HOMO-7$_{B_1}$, and HOMO-7$_{B_2}$ can be assigned to the p_z, p_x, and p_y orbitals respectively

assigned to p_x and p_y orbitals respectively, are physically similar. (see Section A.1)

Furthermore, in the one-body (uncorrelated) fashion, this initial state is still an eigenstate of the Hamiltonian. Therefore, in this picture, the system would not experience any dynamics. However, in the correlated universe, the state $|\psi(t_0)\rangle$ is not an eigenstate of the Hamiltonian including many-body effects, and hence the system will exhibit dynamics driven by the existence of the electronic correlation [15]. We have to note that, using the complete many-body state to describe this dynamics is beyond today's computational resources. For that reason, we are going to employ the MPS approach to resolve the above-mentioned dynamics. As we discussed in Section 4.2, using a non-orthogonal Krylov basis improves the performance of the MPS time-evolution approach, but it is limited to special cases and generally suffers from numerical instability issues. For that reason, we use the orthogonal Krylov space method to propagate the MPS in time. In the following calculations, we use a Krylov space dimension of $N_K = 6$ and time step size of $\delta t = 1as$. Based on the analysis [47] on the performance of the orthogonal Krylov space approach in terms of the Krylov space dimension and time step size, we expect that these parameters give rise to stable time-evolution parameters. Consequently, we only need to vary the bond dimension, to ensure that the dynamics is stable in terms of the part of the Hilbert space covered by the MPS representation.

5.3 Towards the Stable Dynamics

To do the study on the stability of the dynamics in terms of the MPS bond dimension, let us introduce the time-dependent *one electron reduced density*

matrix (OERDM) as follows:

$$\gamma_{ij}(t) = \sum_{\sigma} \langle \psi(t) | \hat{c}^{\dagger}_{i\sigma} \hat{c}_{j\sigma} | \psi(t) \rangle \tag{5.2}$$

where $\hat{c}^{\dagger}_{i\sigma}$ and $\hat{c}^{\dagger}_{i\sigma}$ are annihilation and creation operators respectively. Obviously, time-dependent occupation numbers of the molecular orbitals can be extracted from the diagonal elements of the time-dependent OERDM.

Figure 5.3 indicates the time-evolution of the occupation numbers of the 13 molecular orbitals which are most involved in the dynamics following sudden ionization of the $2p$ orbitals of the silicon atom in the SiF_4 molecule for different bond dimensions in a range between 100 and 160. For all bond dimensions after an extended period of shake-up processes, the initial hole starts to be populated by an electron from an inner valence molecular orbital, and one electron from the outer valence molecular orbitals is excited to virtual orbitals (LUMOs). However, it is obvious that the time-evolution of the occupation numbers of the molecular orbitals do not converge to stable dynamics in this range of bond dimensions and it seems that increasing the bond dimension is required to obtain convergent results. It is also worth mentioning that the complexity of the MPS representation scales like $\mathcal{O}(D^3)$ with the MPS bond dimension [47]. This means, for example, that a two times increase in the bond dimension leads to the computation time eight times larger. Therefore, increasing the bond dimension to achieve stable results is not feasible due to the restriction of computational and time resources.

Furthermore, we mentioned in Section 4.4 that the numerical noise only helps to improve the variational optimization scheme by restoring the missing symmetry blocks in the sweep procedure. It implies that, if the MPS bond dimension is large enough to resolve the valid dynamics in the system, then adding numerical noise at reasonable values does not alter that quantitatively. Figure 5.4 shows the time-evolution of the occupation number of the initial hole for various noise prefactors. This figure indicates that a variation of the noise prefactor alters the filling rate of the initial hole significantly. More specifically, decreasing the noise prefactor leads to an increasing filling rate of the initial hole. Also, it means that the dynamics is not stable with respect to numerical noise. It is another evidence that demonstrates the MPS with a bond dimension within the range of 100 and 160 is not capable of resolving the exact driven dynamics. In other words, within this range of bond dimension, the MPS approach is not able to capture the necessary amount of the electronic correlations to describe the dynamics reliably.

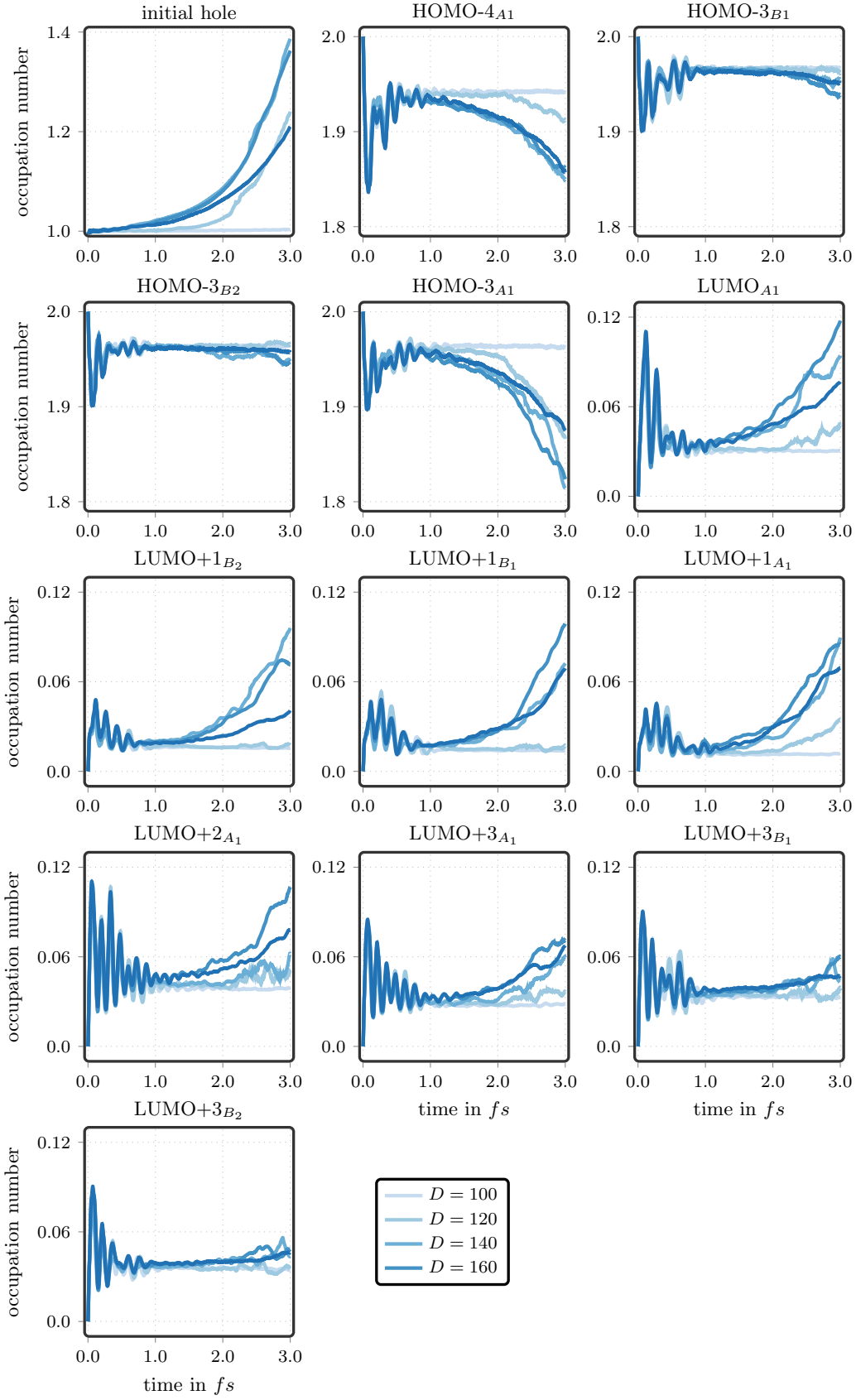

Figure 5.3: Time-evolution of the occupation number of the molecular orbitals which are most involved in the dynamics for various MPS bond dimension. Here irrep orbital ordering is employed and the nosie prefactor = $10^{-3}, 10^{-6}, 0$ is used in the sweep instructions.

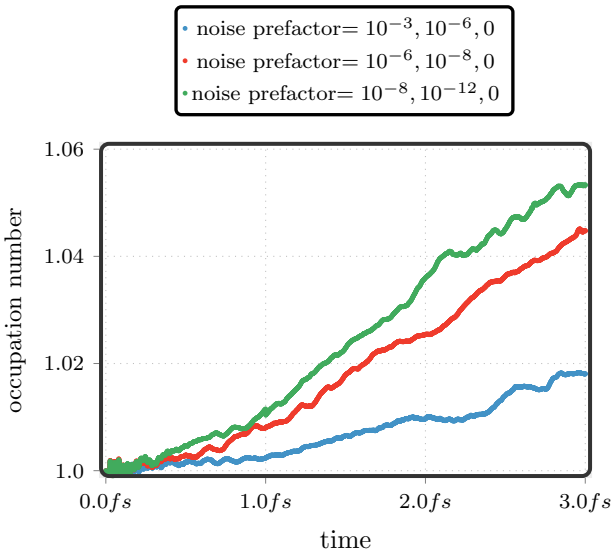

Figure 5.4: Time-evolution of the occupation number of the initial hole for various noise prefactors in the sweep instruction. Here, an MPS bond dimension of $D = 150$ is employed for all calculations.

5.3.1 Influence of Orbital Ordering

Ordering of the orbitals in the MPS representation is crucial for its performance. When one tries to use an MPS approach for three-dimensional molecules, it is necessary to map the orbitals to a one-dimensional lattice or, in other words, choose an ordering to place the orbitals in the one-dimensional chain. Such an orbital ordering should be done such that entanglement between distant orbitals on the lattice is minimized [169, 170]. If one ignores this condition and places the orbitals randomly in the one-dimensional lattice, then the non-local properties of the system are artificially exaggerated or, in the context of electronic correlations, an artificial correlation length is introduced in the system which can be a bad approximation. Hence, in this case, to capture the necessary amount of electronic correlations to describe the dynamics, a relatively large MPS bond dimension is required.

Until now, all the calculations we have presented are based on the ordering of the orbitals according to the orbital symmetry and the orbital energy. In other words, in the MPS representation of the many-body state, firstly, orbitals are ordered concerning their irreducible representation. Within these symmetry sectors, they are ordered according to the orbital energy. Such orbital ordering can give rise to a reduction of the long-range coherence in the system since due to the different irreducible representations, the OERDM is reduced to block-diagonal form i.e. matrix elements of the OERDM are zero for orbitals with different irreducible representation.

As we saw earlier, such orbital ordering is not successful at improving the performance of the MPS representation in the case of the ionization in the

$2p$ orbital of the silicon atom in SiF_4 molecule with reasonable MPS bond dimension. This orbital is a core orbital and ionization from the core orbital can trigger strongly correlated electron dynamics. This means a core ionization corresponds to a strong excitation which leads to fast emerging correlations. Therefore, to describe the correlation-driven dynamics in the system in this case, large MPS bond dimension are still necessary.

We have previously mentioned that ordering the orbitals randomly in the MPS representation, leads to exaggerating the non-local properties of the system and a decline in the performance of the MPS approach. Moreover, we have seen that since ordering orbitals based on the irreducible representations reduces the long-range coherence of the system, it is not beneficial to describe the correlation-driven dynamics in the core ionized SiF_4 molecule. Therefore, to reduce the artificial effects caused by placing the orbitals in the one-dimensional lattice, it is important to place the strongly correlated orbitals close to each other in the one-dimensional chain in the MPS representation to achieve optimal performance.

One way to order orbitals to improve the performance of MPS representation and consequently its convergence rate is based on the minimization of the bandwidth of the *exchange matrix* [171, 172]. In practice, a fast approximate bandwidth minimization is obtained by the so-called *Fiedler vector* [170]. If one assumes the position of the n orbitals on the orbital lattice as a continuos one-dimension variable $\vec{x} = (x_1, x_2, \ldots, x_n)$, then a cost function to measure the distance between orbitals on the lattice can be defined as [156]:

$$F(\vec{x}) = \frac{1}{2} \sum_{i \neq j} K_{ij} \, (x_i - x_j)^2 \tag{5.3}$$

where K_{ij} denotes the elements of the exchange matrix

$$K_{ij} = \int \chi_i^*(r_1)\chi_j(r_1) \frac{e^2}{4\pi\varepsilon_0 \, |r_1 - r_2|} \chi_j^*(r_2)\chi_i(r_2) \, dr_1 dr_2 \, . \tag{5.4}$$

Minimization of the cost function $F(x)$ with respect to the vector of the positions x results in an optimal position of the orbitals or Fiedler vector. We have to note that, in the minimization procedure of the cost function, the following constraints should be imposed in order to fix the translation invariance and

normalization of the solution.

$$\sum_i x_i = 0 \tag{5.5}$$

$$\sum_i x_i^2 = 1 \tag{5.6}$$

Generally, the first constraint is imposed to prevent rigid translation of all positions and the second one (normalization of the solution) is applied to prevent a trivial solution where $\vec{x} = (0, 0, \ldots, 0)$.

To obtain the derived ordering, the cost function in Equation 5.3 can be rewritten as:

$$F(\vec{x}) = x^{\dagger} L x \tag{5.7}$$

with the symmetric and positive Laplacian

$$L = D - K \tag{5.8}$$

Where D is a diagonal matrix with entires[170]:

$$D_{ii} = \sum_j K_{ij} \ . \tag{5.9}$$

Now, minimization of the cost function with respect to the above mentioned constraints is equivalent to finding the second lowest eigenvector of the Laplacian L [173, 174]. Bear in mind that the constant vector $\vec{1} = (1, 1, \ldots, 1)$ is the eigenvector of the L with the smallest eigenvalue, i.e. 0 which is discarded due to the translational invariance constraint (Equation 5.5). Therefore, the second lowest eigenvector of L is the Fiedler vector, the solution to the constrained minimization of $F(\vec{x})$. Sorting the entries of the Fiedler vector then gives the Fiedler ordering.

In the following, we want to study the influence of the ordering of the orbitals based on the Fiedler vector (let us call it Fiedler ordering) and compare the dynamics of electrons with those obtained by ordering of the orbitals based on their irreducible representations (irreps ordering). Figure 5.5 shows the time-evolution of the occupation numbers of the molecular orbitals with irrep ordering in comparison to Fiedler ordering. In contrast to the irrep ordering based results, in the Fiedler ordering case, the initial core hole itself does not participate in the dynamics and the respective occupation number stays unchanged at all times. Moreover, one can see that only three molecular

orbitals significantly contribute to the dynamics (HOMO-4_{A1}, LUMO$_{A1}$, and LUMO+2_{A1}) and it seems that this dynamic is an oscillatory one with a defined period.

Table 5.1 shows the ordering of the orbitals with respect to their irreducible representation and Fiedler vector of the exchange matrix. In the irrep ordering, the orbitals that are dominantly contributing to the dynamics (which are highlighted in bold) are distributed throughout the one-dimensional lattice, whereas in the Fiedler ordering those are placed close to each other at the end of the lattice. For this reason, we believe that HOMO-4_{A1}, LUMO$_{A1}$, and LUMO+2_{A1} are strongly correlated, and by putting those close to each other the artificial correlation length which is introduced in the system is reduced. Therefore, instead of the 13 orbitals (that include the initial hole, and the HOMO-7_{A_1}), which are previously contributed to the dynamics, only three participate in the Fiedler dynamics. Moreover, in the irrep ordering the cost function in Equation 5.3 is equal to $F(\vec{x}) = 12827$ whereas it is reduced to $F(\vec{x}) = 5774$ by Fiedler ordering. As we expected, employing Fiedler ordering minimizes the cost function significantly.

In addition, Fiedler ordering unlike irrep ordering leads to conservation of the norm of the wave function and energy of the system. Figure 5.6 shows the norm of the wave function (left) and the energy of the system as a function of time (right)for irrep and Fiedler ordering. It is obvious that the norm of the wave function and also the energy of the system in the irrep ordering change with time, while in the Fiedler ordering, these parameters are conserved with the desired accuracy.

It is worthwhile to mention that the Fiedler ordering leads to convergent results in terms of the MPS bond dimension. The time-evolution of the occupation numbers of the initial hole plus the three molecular orbitals which mostly contribute to the dynamics for various MPS bond dimensions are depicted in Figure 5.7. One can see that no significant differences occur in the occupation number dynamics of individual molecular orbitals by increasing the MPS bond dimension within the range of $D = 100$ and $D = 160$. In other words, for all these bond dimensions, the resulting dynamics are similar and we can assume that the results resolve the dynamics accurately. It should be noted that, by ordering the orbitals based on the Fiedler vector, the above mentioned artificial long-range property of the system is reduced, and unlike the irrep ordering, an MPS bond dimension $D = \mathcal{O}(100)$ is sufficient to resolve the dynamics triggered by ionization of the core orbital.

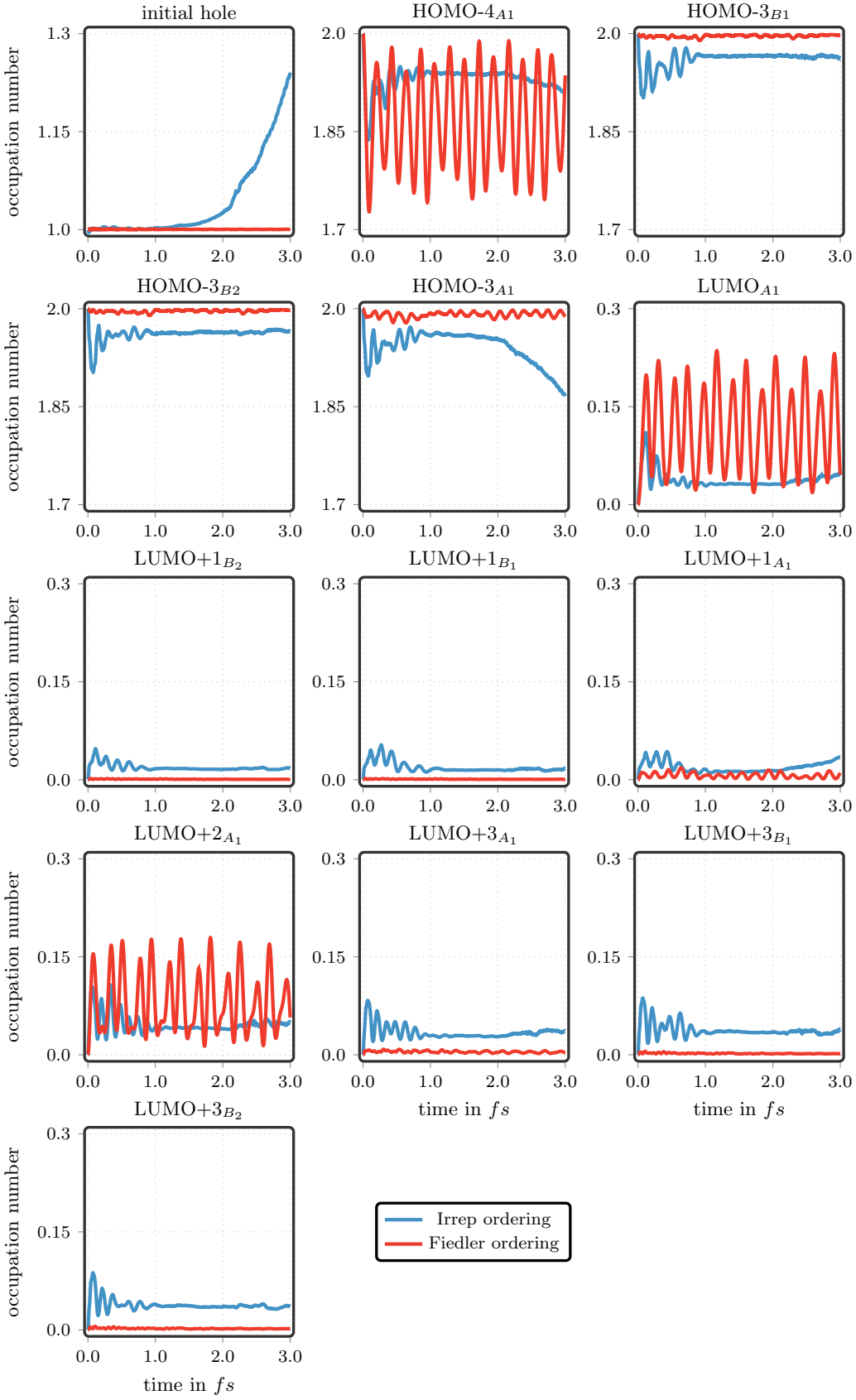

Figure 5.5: Time-evolution of the occupation number of the molecular orbitals which are most involved in the dynamics for normal ordering and Fiedler ordering. Here, an MPS bond dimension of $D = 120$ and the noise prefactor = $10^{-3}, 10^{-6}, 0$ in the sweep instruction are used for all calculations.

site	irrep ordering	Fiedler ordering
1	HOMO-9$_{A_1}$	HOMO-1$_{B_1}$
2	HOMO-8$_{A_1}$	HOMO-7$_{B_2}$
3	**HOMO-7$_{A_1}$**	HOMO-2$_{A_2}$
4	HOMO-6$_{A_1}$	HOMO-3$_{B_1}$
5	HOMO-5$_{A_1}$	LUMO+4$_{A_1}$
6	**HOMO-4$_{A_1}$**	LUMO+6$_{A_1}$
7	**HOMO-3$_{A_1}$**	HOMO-5$_{B_2}$
8	HOMO-2$_{A_1}$	HOMO$_{A_2}$
9	HOMO-1$_{A_1}$	HOMO-5$_{B_1}$
10	**LUMO$_{A_1}$**	LUMO+6$_{B_1}$
11	**LUMO+1$_{A_1}$**	LUMO+6$_{B_2}$
12	**LUMO+2$_{A_1}$**	HOMO-7$_{B_1}$
13	**LUMO+3$_{A_1}$**	HOMO-2$_{A_1}$
14	LUMO+4$_{A_1}$	HOMO-1$_{B_2}$
15	LUMO+6$_{A_1}$	LUMO+5$_{A_2}$
16	LUMO+7$_{A_1}$	LUMO+9$_{A_1}$
17	LUMO+8$_{A_1}$	LUMO+7$_{A_1}$
18	LUMO+9$_{A_1}$	LUMO+4$_{A_2}$
19	LUMO+10$_{A_1}$	HOMO-3$_{B_2}$
20	HOMO-7$_{B_1}$	LUMO+8$_{A_1}$
21	HOMO-5$_{B_1}$	LUMO+10$_{A_1}$
22	**HOMO-3$_{B_1}$**	LUMO+1$_{B_1}$
23	HOMO-1$_{B_1}$	LUMO+1$_{B_2}$
24	HOMO$_{B_1}$	HOMO-5$_{A_1}$
25	**LUMO+1$_{B_1}$**	LUMO+5$_{B_2}$
26	**LUMO+3$_{B_1}$**	LUMO+5$_{B_1}$
27	LUMO+5$_{B_1}$	HOMO-1$_{A_1}$
28	LUMO+6$_{B_1}$	HOMO-6$_{A_1}$
29	LUMO+8$_{B_1}$	LUMO+3$_{B_2}$
30	LUMO+9$_{B_1}$	LUMO+3$_{B_1}$
31	HOMO-7$_{B_1}$	HOMO-3$_{A_1}$
32	HOMO-5$_{B_1}$	LUMO+1$_{A_1}$
33	**HOMO-3$_{B_2}$**	LUMO+8$_{B_1}$
34	HOMO-1$_{B_2}$	LUMO+8$_{B_2}$
35	HOMO$_{B_2}$	**HOMO-4$_{A_1}$**
36	**LUMO+1$_{B_2}$**	**LUMO$_{A_1}$**
37	**LUMO+3$_{B_2}$**	**LUMO+2$_{A_1}$**
38	LUMO+5$_{B_2}$	LUMO+3$_{A_1}$
39	LUMO+6$_{B_2}$	LUMO+9$_{B_1}$
40	LUMO+8$_{B_2}$	LUMO+9$_{B_2}$
41	LUMO+9$_{B_2}$	HOMO$_{B_2}$
42	HOMO-2$_{A_2}$	HOMO$_{B_1}$
43	HOMO$_{A_2}$	**HOMO-7$_{A_1}$**
44	LUMO+4$_{A_2}$	HOMO-8$_{A_1}$
45	LUMO+5$_{A_2}$	HOMO-9$_{A_1}$

Table 5.1: Ordering of the orbitals based on their irreducible representations and Fiedler vector. The orbitals which are dominantly participating in the dynamics in each ordering are highlighted in bold. In the irrep ordering, orbitals firstly are ordered with respect to their irreducible representation and within the symmetry sectors, they are ordered according to their energy. Moreover, in the irrep ordering, the orbitals irreps follow Molpro convention.

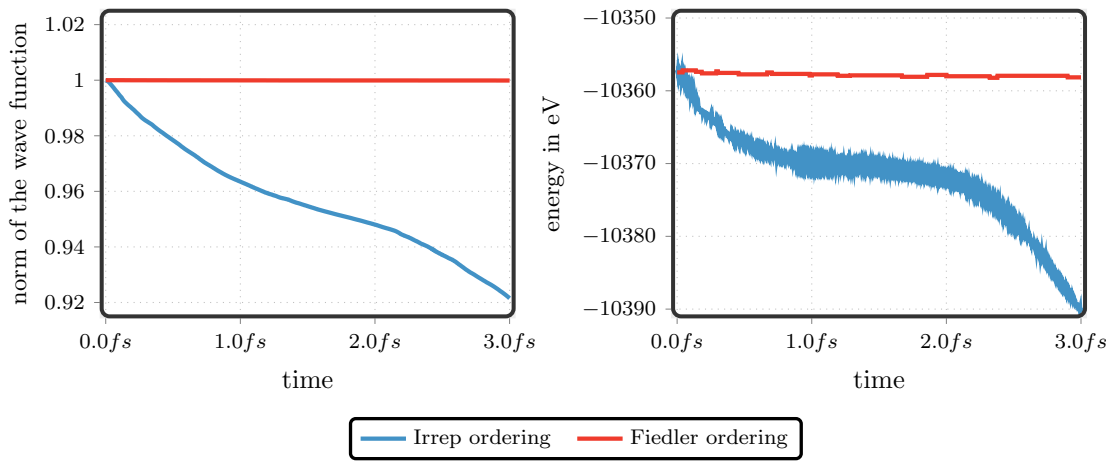

Figure 5.6: (left) Norm of the wave function as a function of time. (right) Energy of the system as a function of time for irrep ordering and Fiedler ordering. Here, a bond dimension of $D = 120$ and the noise prefactor = $10^{-3}, 10^{-6}, 0$ in the sweep instruction are used for all calculations.

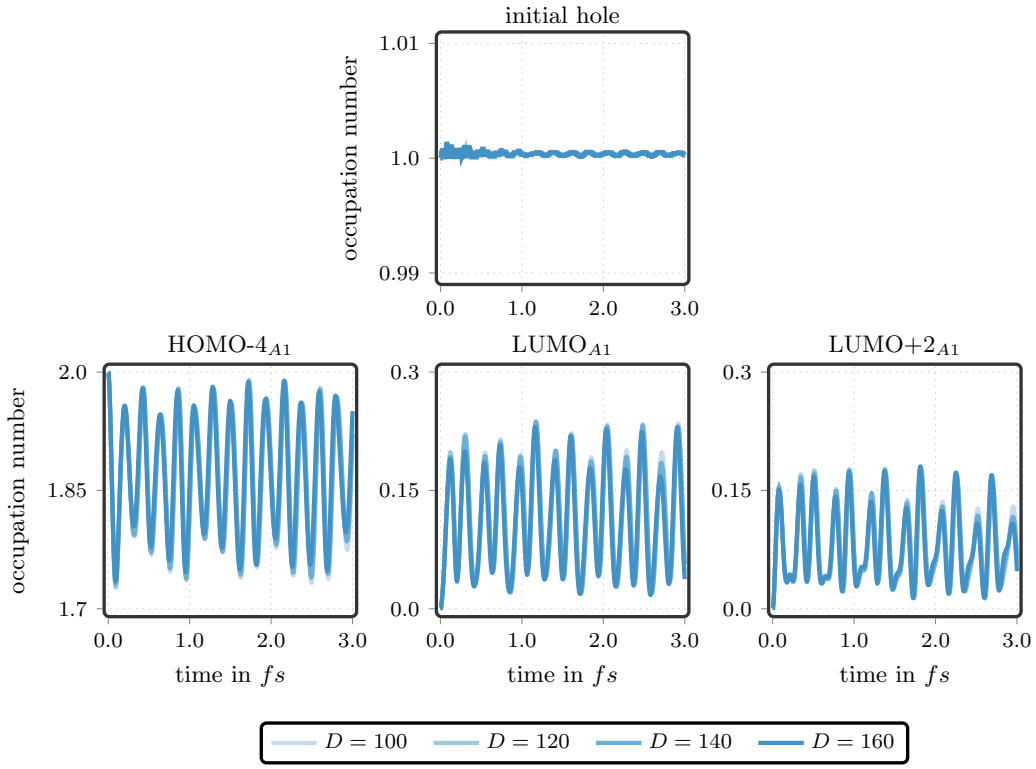

Figure 5.7: Time-evolution of the occupation number of the molecular orbitals which are most involved in the dynamics for various MPS bond dimension. Here Fiedler orbital ordering is employed and the noise prefactor = $10^{-3}, 10^{-6}, 0$ is used in the sweep instruction.

5.3.2 Influence of Numerical Random Noise

As we mentioned before in Section 4.4, we expect that increasing the noise prefactor leads to an improved convergence rate of the dynamics in terms of the MPS bond dimension. On the other hand, we have previously seen that varying the noise prefactor in the sweep instructions alters the dynamics for irreps ordering. It means, in this case, the dynamics is not stable in terms of the

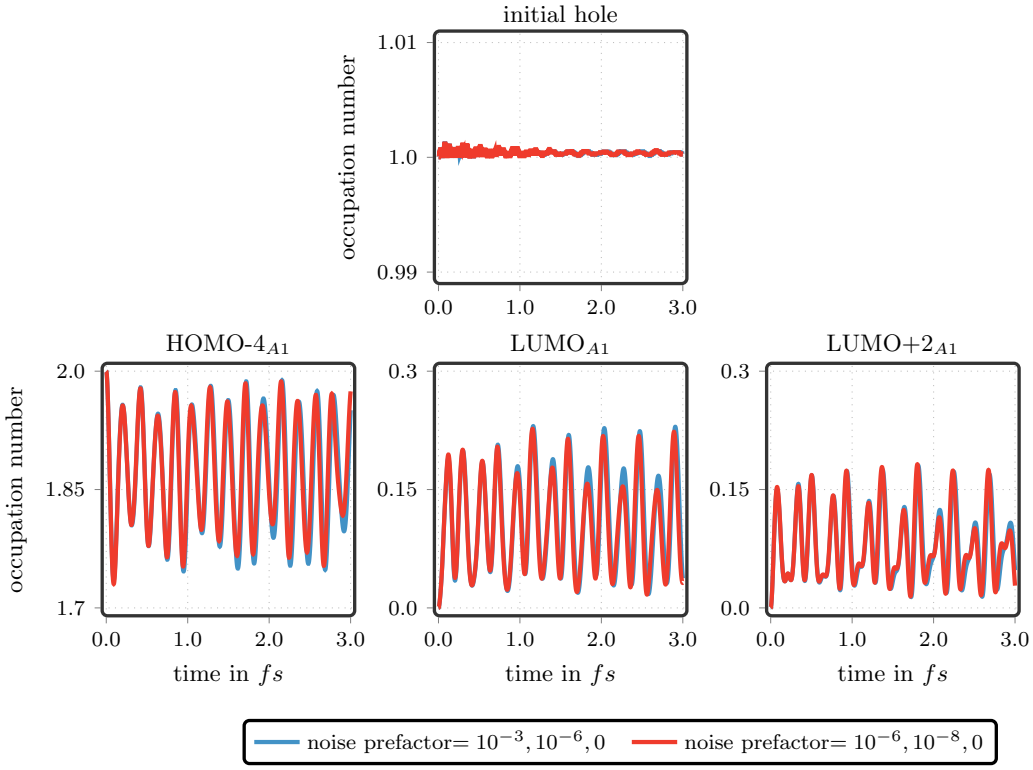

Figure 5.8: Time-evolution of the occupation number of the molecular orbitals which are most involved in the dynamics for various noise prefactors in the sweep instruction. Here Fiedler orbital ordering and the MPS bond dimension of $D = 160$ are employed.

numerical noise. In contrast to the irrep ordering case, in the Fiedler ordering case, varying the noise prefactor does not affect the dynamics within the period of $3fs$ after the sudden ionization. Figure 5.8 illustrates the time-evolution of the initial hole and three molecular orbitals which are most involved in the dynamics for the two different noise prefactors. It is apparent that for the two different noise prefactors there is no significant difference in the dynamics. It is another evidence for numerical stability of the resolved dynamics based on the Fiedler ordering.

Figure 5.9 depicts the time-evolution of the occupation number of the most important molecular orbitals considering the dynamics for various MPS bond dimension with smaller noise prefactor (noise prefactor = $10^{-6}, 10^{-8}, 0$). It seems that doing time-evolution with a smaller noise prefactor leads to diminishing convergence rates of the MPS approach (notable after $2fs$) with respect to the MPS bond dimension. To perform a quantitative analysis of this behavior, we will use the square difference between converged occupation number dynamics $n(t)_{D_{con}}$, and one of the other occupation number dynamics in terms of the MPS bond dimension $n(t)_D$, as follows:

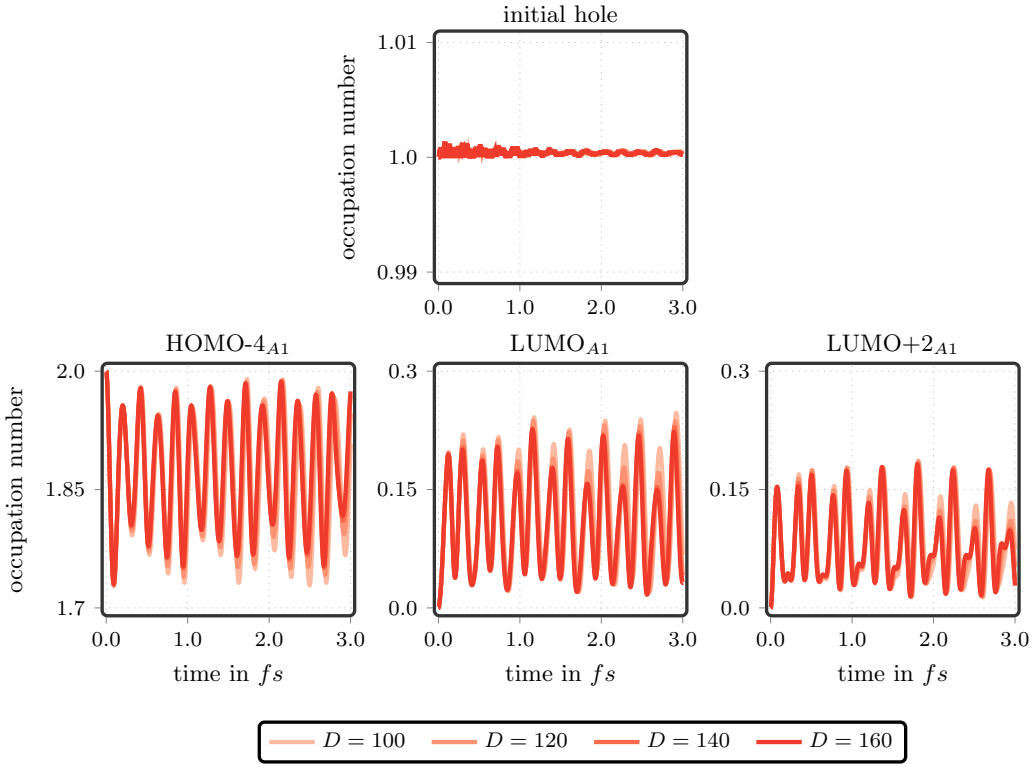

Figure 5.9: Time-evolution of the occupation number of the molecular orbitals which are most involved in the dynamics for various MPS bond dimension. Here Fiedler orbital ordering is employed and the noise prefactor = $10^{-6}, 10^{-8}, 0$ is used in the sweep instruction.

$$d(t)_D = \left(n(t)_{D_{con}} - n(t)_D \right)^2. \tag{5.10}$$

We see from Figure 5.7 to Figure 5.9 that the results are convergent for $D_{con} = 140$ for both noise prefactors and it means that for larger MPS dimension one does not see a significant dependency of the dynamics on the MPS bond dimension.

The Top panels of Figure 5.10 demonstrate the obtained square difference between the converged occupation numbers and occupation numbers with MPS bond dimension $D = 100$ based on the Equation 5.10 for different molecular orbitals and various noise prefactors. It is apparent that the square difference for smaller noise prefactor $(10^{-6}, 10^{-8}, 0)$ is remarkably larger compared to larger noise prefactor $(10^{-3}, 10^{-6}, 0)$. As we already expected, increasing the noise prefactor leads to an improved convergence rate of the MPS approach with respect to the bond dimension.

In addition, the bottom panels of Figure 5.10 indicate the same behavior for $D = 120$, but it should be noted that the square difference for larger MPS bond

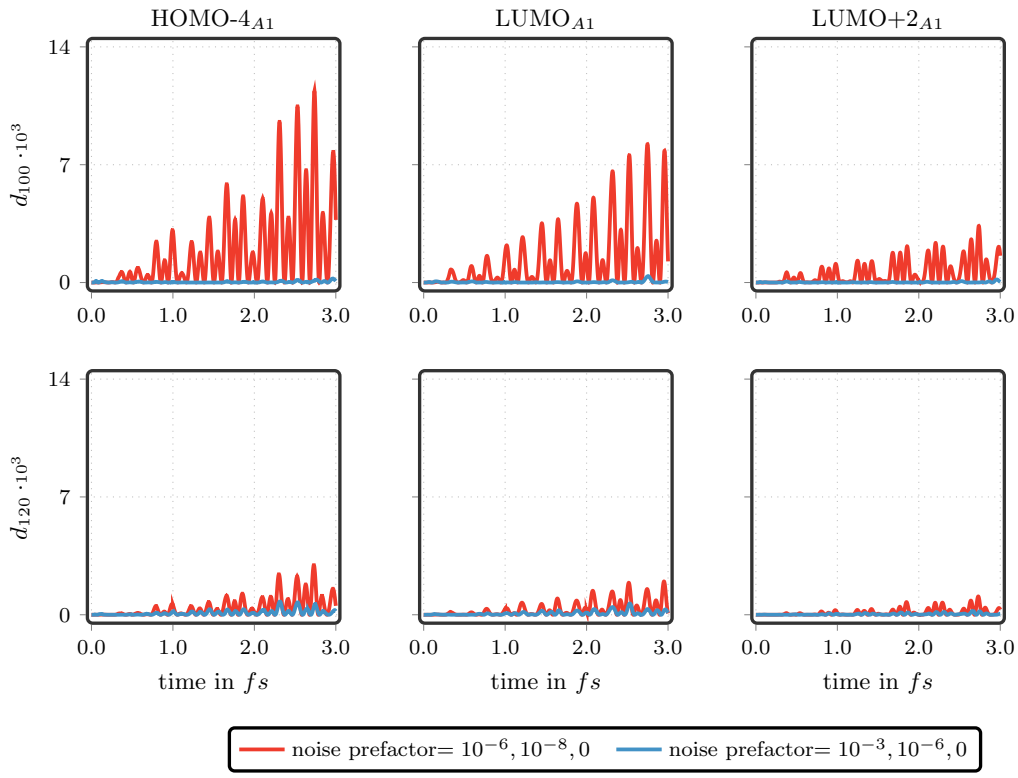

Figure 5.10: Time-evolution of the square difference between converged occupation number and occupation number with MPS bond dimension $D = 100$ (d_{100}) (top) and $D = 120$ (d_{120}) (bottom) for different molecular orbitals and various noise prefactors in the sweep instruction.

dimension ($D = 120$) is significantly reduced for both of the noise prefactor and all the molecular orbitals. Additionally, we observe the square differences grow with time. Roughly speaking, the square difference parameter can be interpreted as the error of the occupation number dynamics. On the other hand, it is shown that the error of the OERDM [1] in the time-dependent MPS approach grows linearly with time and can be controlled by adjusting the bond dimension of the MPS representation [45]. Therefore, regarding the Figure 5.10 the error of the occupation number dynamics can be controlled by tuning the numerical noise as well as adjusting the MPS bond dimension.

[1] As we mentioned earlier, the diagonal elements of the OERDM are the occupation numbers of molecular orbitals.

5.4 Conclusions

In this chapter, we employed the MPS representation of the many-body state to investigate the charge migration in silicon tetrafluoride. In this study, we considered the $2p$ orbital of the silicon atom in silicon tetrafluoride, which is a core orbital, suddenly ionized. We found out that orbital ordering is crucial in the performance of the MPS approach to study the electron dynamics in the core ionized silicon tetrafluoride. We realized that placing the strongly

correlated orbitals close to each other in the one-dimensional lattice improves the performance of the MPS approach. We understood that, unlike the ordering of the orbitals based on the irreducible representations, MPS bond dimension $D = \mathcal{O}(100)$ is sufficient to resolve the dynamics in this case. In addition, we saw that the numerical noise, which was introduced in the variational optimization of the MPS, is another concept that can increase the efficiency of the MPS approach. By performing quantitative analysis, we showed that increasing the noise prefactor in the sweep instruction leads to an enhanced convergence rate of the dynamics in terms of the MPS bond dimension.

6 Correlated Charge Migration Following Core Ionization in Silicon Tetrafluoride

6.1 Introduction

In the previous chapter, we have applied the MPS approach to study the correlated electron dynamics in core ionized silicon tetrafluoride. To obtain the convergent dynamics we have considered two kinds of the ordering of the orbitals and found out that the orbital ordering based on the Fiedler vector leads to convergent dynamics in terms of the MPS bond dimension within a range which is computationally accessible. Additionally, we have investigated the role of the numerical noise on the electron dynamics and showed that increasing the noise prefactor in sweep instructions enhances the convergence rate of the MPS approaches in terms of the bond dimension.

In the following chapter, we want to investigate the electron dynamics triggered by the core ionization in silicon tetrafluoride. We show that core ionization of silicon tetrafluoride triggers intense and fast charge migration in the valence orbitals while the initial hole remains unchanged during the dynamics. This charge migration occurs on a shorter time scale than the decay of the core hole by the Auger process. (The Auger decay time of the $2p$ hole in silicon tetrafluoride is around $8\,fs$ [175].) To understand the origin of the time period of the charge migration, we analyze the dynamics and detect the correlated cationic eigenstates which are responsible for the charge migration. Finally, we investigate the role of the nuclear geometry in the charge migration process and find out that small nuclear displacements along the normal modes of the molecule can change the time period of the charge migration which can lead to damping of dynamics similar to the situation that was reported elsewhere [176].

6.2 Charge Migration in Core Ionized Silicon Tetrafluoride

As we saw in Section 5.3, after obtaining the convergent dynamics which is induced by the sudden ionization of the $2p$ orbital of the silicon atom in SiF_4, we understood that only three orbitals (HOMO-4_{A1}, LUMO$_{A1}$, and LUMO+2_{A1} which are displayed in Figure 6.1) are dominantly involved in the dynamics while the initial hole does not change during dynamics. To have a closer look at the spatial distribution of these molecular orbitals we are using the molecular orbitals composition analysis.

Generally, a molecular orbital can be defined as the linear combination of atomic orbitals.

$$\phi_i(r) = \sum_\mu C_{\mu i}\chi_\mu(r) \tag{6.1}$$

where $C_{\mu i}$ is the molecular orbital coefficient and χ_μ is the atomic orbital. Inserting Equation 6.1 into the orthonormality condition of the molecular orbitals yields

$$\sum_\mu C_{\mu i}^2 + 2\sum_\mu \sum_{\nu>\mu} C_{\mu i}C_{\nu i}S_{\mu\nu} = 1 \tag{6.2}$$

where $S_{\mu\nu}$ is the overlap matrix among atomic orbitals given by:

$$S_{\mu\nu} = \int \chi_\mu(r)\chi_\nu^*(r)\,dr \tag{6.3}$$

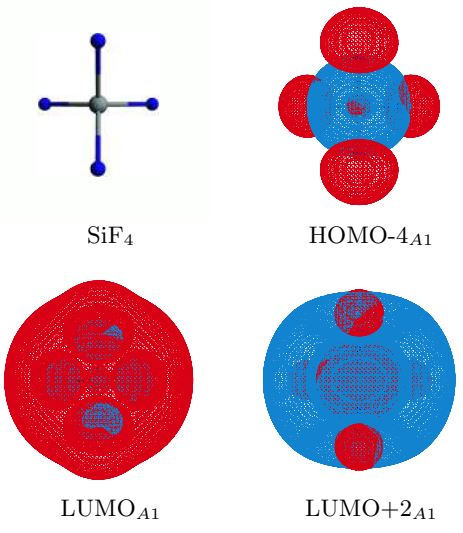

Figure 6.1: Molecular geometry of silicon tetrafluoride determined by geometry optimization on the Hartree-Fock level and three relevant valence molecular Hartree-Fock orbitals participating in the dynamics following ionization of the $2p$ orbital of the silicon atom in silicon tetrafluoride molecule. Shown are the HOMO-4_{A1} orbitals occupied in the electronic ground state of this molecule and the unoccupied orbitals LUMO$_{A1}$ and LUMO+2_{A1}.

The first term in Equation 6.2 is a local term that characterizes the net population of the atomic orbital in molecular orbital i. The second term is a cross term that characterizes the shared electrons between atomic orbital pairs in molecular orbital i. Once the basis functions [1] are set and the coefficients of the atomic orbitals obtained, the molecular orbital compositions can be calculated directly according to their different definitions. In the *Mulliken analysis* [177], the cross terms are equally partitioned to the corresponding atomic orbitals. Consequently, the composition of atomic orbital μ to molecular orbital i is defined as [178]:

$$\Theta_{\mu i} = C_{\mu i}^2 + \sum_{\nu \neq \mu} C_{\mu i} C_{\nu i} S_{\mu \nu} \, . \tag{6.4}$$

In practical applications, the composition analysis based on the Mulliken method has the disadvantage that the result of the composition analysis can be meaningless due to negative values. To avoid this issue we use the method proposed by Ros and Schuit [179]. In this method, the composition of the atomic orbital μ in molecular orbital i is defined as:

$$\Theta_{\mu i} = \frac{C_{\mu i}^2}{\sum_\nu C_{\nu i}^2} \, . \tag{6.5}$$

By inserting identity which has been already introduced in Equation 6.2 into the above formula, Θ can be rewritten as:

$$\Theta_{\mu i} = C_{\mu i}^2 + \frac{C_{\mu i}^2}{\sum_\nu C_{\nu i}^2} \sum_{\nu \neq \mu} C_{\mu i} C_{\nu i} S_{\mu \nu} \tag{6.6}$$

It is clear that in this decomposition of molecular orbital i into atomic orbital μ, the total terms of all atom pairs are partitioned instead of the cross terms between atomic orbitals μ and other ones. The advantage of the method which was introduced by Rose and Schuit is that negative values of the Θ never occur.

In addition, the molecular composition analysis can be done in terms of the different atoms. Considering the total contribution of orbitals belonging to a specific atom, one can define:

$$\Theta_{i,A} = \sum_{\mu \in A} \Theta_{\mu i} \tag{6.7}$$

where $\Theta_{i,A}$ indicates the weight of the molecular orbital i which can be attributed to atom A.

[1] In the context of quantum chemistry, when a molecular calculation is performed, it is common practice to use a basis composed of atomic orbitals. Therefore, in this context, basis functions and atomic orbitals are sometimes used interchangeably, however, the basis functions are generally not true atomic orbitals.

Table 6.1: Composition analysis based on the Ros-Schuit partition of the molecular orbitals which contribute the most to the dynamics after sudden ionization of the $2p$ electron of the silicon atom in SiF_4. This analysis has been done using the composition analysis implementation of the Multiwfn program [180].

Orbital	Silicon	Tetrafluoride
HOMO-4_{A_1}	39.98 %	60.02 %
LUMO$_{A_1}$	73.22 %	26.78%
LUMO+2_{A_1}	94.94 %	5.06 %

In Table 6.1 the result of the composition analysis in terms of the different parts of the SiF_4 molecule, i.e. silicon atom and tetrafluoride part, for the molecular orbitals contribute the most to the dynamics after sudden ionization of the $2p$ electron of the silicon atom (HOMO-$7A_1$) is reported. LUMO$_{A1}$, and LUMO+2_{A1} are mostly located at the silicon atom, while HOMO-4_{A1} has a substantial contribution of the tetrafluoride part. Thereby, by removing one electron from the silicon core, excitations in the valence space are generated to screen the core hole. These excitations thus correspond to charge migration from the silicon atom to the tetrafluoride part.

To illustrate this charge migration mechanism in space and time, we calculate the time-dependent hole density which is given by:

$$\rho_h(r,t) = \rho_{HF}(r) - \rho(r,t) \tag{6.8}$$

where $\rho_{HF}(r)$ is the electron density in the Hartree-Fock ground state and $\rho(r,t)$ is the time-dependent electron density which is given by:

$$\rho(r,t) = \sum_{ij} \gamma_{ij}(t)\phi_i(r)\phi_j^*(r)\,. \tag{6.9}$$

Here $\gamma_{ij}(t)$ is the time-dependent OERDM and $\phi_i(r)$ are molecular orbitals obtained from the Hartree-Fock calculation.

In Figure 6.2 we see snapshots of the time-dependent hole density at four different points in time. Obviously, at the time $t = 0$ the initial hole is completely localized on the silicon atom. Following the sudden ionization at time $t = 0$, valence electrons start flowing from the tetrafluoride part to the silicon atom. Accordingly, at time $t = 0.11\,fs$ the hole migrates from the valence orbitals of the silicon atom to the tetrafluoride part while the initial hole at the core of the silicon atom stays unchanged. After a short time, $t = 0.21\,fs$, the electrons partially flow back to the fluoride atoms and therefore the hole migrates back to the silicon atom incompletely, and the whole process begins again while the initial hole remains unaffected. Note that the holes density is positive where

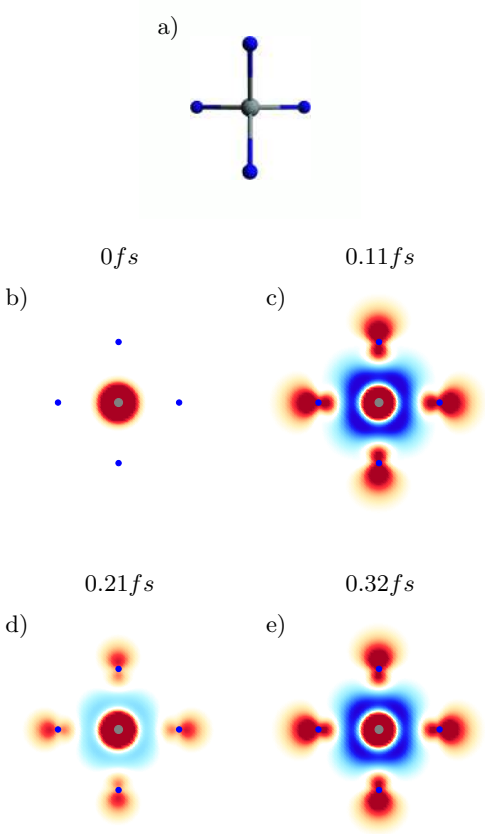

Figure 6.2: Hole density of the silicon tetrafluoride molecule at four different points in time. We use an MPS bond dimension $D = 160$ to represent many-body state. a) molecular structure of the silicon tetrafluoride molecule, b) in the initial state, the hole is completely localized on the silicon atom. c) the hole from valence orbitals of the silicon atom migrates to the tetrafluoride while the initial hole stays unchanged. d) after $0.21\,fs$, the hole migrates back to the valence orbitals of the silicone atom partially. e) the valence hole has moved to the tetrafluoride part again.

electrons are deficient (red) and negative (blue) where they are surplus.

6.3 Population Analysis

We have seen that sudden ionization of the $2p$ orbitals of the silicon atom in a silicon tetrafluoride molecule leads to electron dynamics that gives rise to charge migration in the valence orbitals. To quantify such charge migration we use *Löwdin population analysis* [63]. Doing so, we will be able to quantify how the hole spreads over the individual parts of the molecule and then extract the oscillation period of the hole migration that we have observed above. Moreover, we can attribute each electron in the molecule to one respective atom. In particular, we are capable of examining how many electrons are located at the silicon atom and how many electrons are located at the tetrafluoride part. To do this, we transform the electron density into the orthogonalized atomic orbitals that are localized at the nuclei.

Let us start with the definition of the the number of the electrons. The total number of the electron N can be calculated by integrating the electron density

in Equation 6.9 as follows:

$$N(t) = \int \rho(r,t)\, dr \tag{6.10}$$

$$= \sum_{ij} \gamma_{ij}(t) \int \phi_i(r)\phi_j^*(r)\, dr \tag{6.11}$$

In addition, we already saw that the molecular orbital can be expanded in terms of the atomic orbitals (see Equation 6.1). On the other hand, the atomic orbitals that are used in molecular calculations are not orthonormal. Generally, these orbitals are normalized, but they are not orthogonal to one another. In the population analysis, it is advantageous to use the orthogonal atomic orbitals. A common way to orthogonalize the atomic orbitals is the so-called symmetric orthogonalization, which uses the inverse square root of the overlap matrix (Equation 6.3) as the transformation matrix to construct orthogonalized atomic orbitals[63]

$$\chi'_\alpha = \sum_\beta \left(S^{-\frac{1}{2}}\right)_{\alpha\beta} \chi_\beta \,. \tag{6.12}$$

Now, the molecular orbitals can be expanded in terms of the orthogonal atomic orbitals:

$$\phi_i(r) = \sum_{\mu\alpha} C_{\mu i} \left(S^{\frac{1}{2}}\right)_{\alpha\mu} \chi'_\alpha(r) \,. \tag{6.13}$$

Inserting Equation 6.13 into Equation 6.11 yields:

$$N(t) = \sum_{\mu\nu} \left(\sum_{ij} C_{\mu i}\gamma_{ij}C^*_{j\nu} \right) \left(\sum_{\alpha\beta} \left(S^{\frac{1}{2}}\right)_{\alpha\mu} \left(S^{\frac{1}{2}}\right)_{\beta\nu} \right) \tag{6.14}$$

$$\times \int \chi'_\alpha(r)\chi'^*_\beta(r)\, dr$$

Using the orthonormality of the χ'_α

$$\int \chi'_\alpha(r)\chi'^*_\beta(r)\, dr = \delta_{\alpha\beta} \tag{6.15}$$

and defining

$$\bar{\gamma}_{\mu\nu} = \sum_{ij} C_{i\mu}\gamma_{ij}C^*_{j\nu} \,, \tag{6.16}$$

Equation 6.14 can be rewritten as:

$$N(t) = \sum_{\mu\nu\alpha} \left(S^{\frac{1}{2}}\right)_{\alpha\mu} \bar{\gamma}_{\mu\nu} \left(S^{\frac{1}{2}}\right)_{\alpha\nu} \tag{6.17}$$

$$= \sum_{\alpha} \left(S^{\frac{1}{2}} \bar{\gamma} S^{\frac{1}{2}}\right)_{\alpha\alpha} \tag{6.18}$$

$$= \mathrm{Tr}(S^{\frac{1}{2}} \bar{\gamma} S^{\frac{1}{2}}) \,. \tag{6.19}$$

Here, it is possible to interpret $\left(S^{\frac{1}{2}} \bar{\gamma} S^{\frac{1}{2}}\right)_{\alpha\alpha}$ as the occupation number of the orthogonalized atomic orbital $\chi'_\alpha(r)$ which is maximally doubly occupied. Assuming the atomic orbitals are centered on atomic nuclei, the corresponding number of electrons in orbitals located at the nuclei can be obtained. This procedure is called Löwdin population analysis. Note that if one employs the non-orthogonal atomic orbitals in the above-mentioned procedure, the occupation number of the non-orthogonal atomic orbital χ_μ can be understood as $\left(\bar{\gamma} S\right)_{\mu\mu}$ and similarly, the total number of electrons located on the different nucleus can be obtained. This method is called *Mulliken population analysis*. We have to mention that the Mulliken population analysis suffers from two acute problems. First: the occupation numbers of the atomic orbitals can be larger than two. Second, the occupation numbers can have a negative values which is unphysical and cannot be interpreted in a classical sense. Therefore, it is beneficial to use orthogonalized atomic orbitals (Löwdin population analysis).

We see the results of this hole population analysis in Figure 6.3, which shows the partial hole charge at the silicon atom and at the tetrafluoride part of the molecule for the first $3fs$ after a sudden ionization. Initially, at time $t = 0$, the hole is completely located on the silicon atom. The partial hole charge dynamics indicate the behavior we previously saw in Figure 6.2, but now, the oscillation period can be observed. In addition, Figure 6.3 illustrates the hole population for various MPS bond dimensions. Similar to the time-evolution of the occupation number of the molecular orbitals (Figure 5.7) within the range of $D = 100$ and $D = 160$, no significant dependency of the dynamics is observed. It means that for all the bond dimensions, the resulting dynamics are similar and we can assume that the results resolve the dynamics accurately (within the chosen atomic basis set).

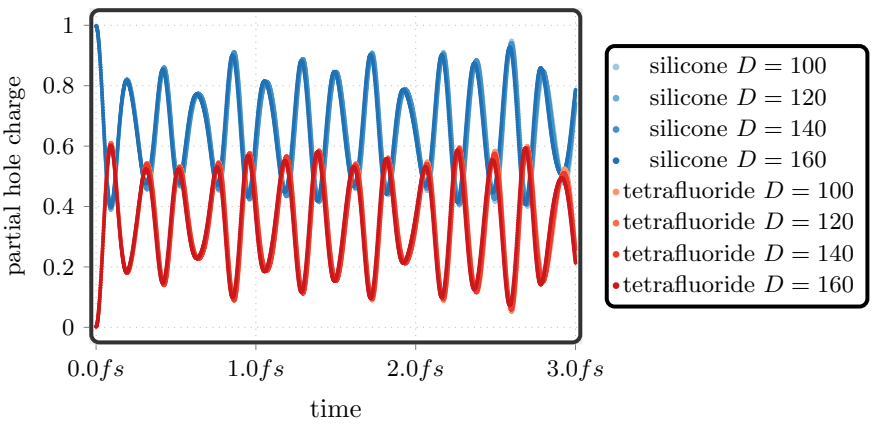

Figure 6.3: Time-dependent partial hole charge at the silicon atom and at the tetrafluoride part of the silicon tetrafluoride molecule. Here, the noise prefacort = $10^{-3}, 10^{-6}, 0$ is employed in the sweep instruction and the many-body state is represented with different bond dimensions D to indicate convergence.

6.4 Autocorrelation Function

To analyze the charge migration following the core ionization, we would like to compute the ionization spectrum of core ionized SiF_4. It is well-known that in the time-dependent calculations the ionization spectrum of a molecule can be easily extracted from the Fourier transformation of the *autocorrelation function* [181–183].

Generally, the autocorrelation function is defined as the overlap between the wave function at time $t = 0$ and time t [184].

$$C(t) = \langle \psi(0) | \psi(t) \rangle \tag{6.20}$$

On the other hand, the time-evolved wave function can be expanded in terms of the cationic eigenstates $|I\rangle$

$$|\psi(t)\rangle = \sum_I \langle I|\psi(t)\rangle \, |I\rangle = \sum_I \langle I| \exp\left(\frac{-iHt}{\hbar}\right) |\psi(0)\rangle \, |I\rangle \tag{6.21}$$

$$= \sum_I \langle I| \exp\left(\frac{-iE_I t}{\hbar}\right) |\psi(0)\rangle \, |I\rangle \tag{6.22}$$

where E_I indicates cationic energy eigenvalues. Inserting Equation 6.22 into Equation 6.20 yields:

$$C(t) = \sum_I \langle I|\psi(0)\rangle \, \langle \psi(0)|I\rangle \exp\left(\frac{-iE_I t}{\hbar}\right) \tag{6.23}$$

$$= \sum_I \alpha_I \exp\left(\frac{-iE_I t}{\hbar}\right) \tag{6.24}$$

where $\alpha_I = |\langle \psi(0)|I\rangle|^2$.

The autocorrelation function includes all information necessary for determining

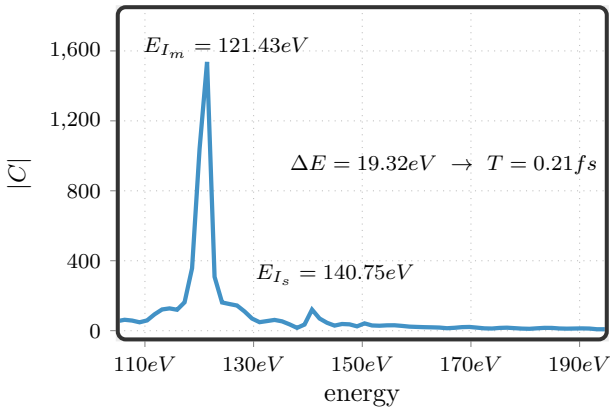

Figure 6.4: Energy-dependent autocorrelation function for the sudden ionization of the 2p orbital of the silicon atom at the center of the molecule. The final time is $3fs$ which leads to a resolution of $1.38eV$ in energy domain. A broadening of $0.14eV$ is applied to resolve the major peaks.

the ionization spectrum. By Fourier transformation of the autocorrelation function into the energy domain $C(E)$, we can derive the ionization energy of the states which contribute to the dynamics.

In Figure 6.4, we see the energy-dependent autocorrelation function extracted from an MPS based calculation with bond dimension $D = 160$. The energy-dependent autocorrelation function has two major peaks, each corresponding to one correlated eigenstate of the cationic molecule i.e. $|I_m\rangle$ and $|I_s\rangle$. The cationic eigenstate $|I_m\rangle$ can be assigned to the core level, at $E_{I_m} = 121.43eV$, and $|I_s\rangle$ can be assigned to the dominant satellite line at $E_{I_s} = 140.75eV$. Generally, one can determine the oscillation period of the electron dynamics by the energy differences between the cationic states involved [16]. The energy difference between the two peaks is about $\Delta E = 19.32eV$ corresponding to the oscillation period $0.21fs$ which resolves the oscillation period extracted from partial hole charge dynamics.

6.5 Transition Probability

In the last section, we found two cationic states which contribute to the electron dynamics. Moreover, it is well known that the main line $|I_m\rangle$ in the ionization spectrum is dominated by a $1h$ configuration and the satellite state $|I_s\rangle$ can be described by a $2h1p$ configuration [185]. In the following, we would like to take a closer look at the satellite states using the transition probability concept.

Let us start with the spin-dependent version of the two-hole-one-particle configuration which can be defined as:

$$|\phi_{aij,s}\rangle = \hat{c}^{\dagger}_{a\tau}\hat{c}_{i\sigma}\hat{c}_{j\tau}\,|\phi_o\rangle \tag{6.25}$$

where $|\phi_o\rangle$ is the Hartree-Fock ground state of the molecule, $\hat{c}$ and $\hat{c}^\dagger$ represent annihilation and creation operators respectively, i and j represent the indices of initially occupied and a labels initially unoccupied spin orbitals. τ and σ indicate the spin of spin orbitals, and s represents the final spin configuration.

A transition amplitude can be defined as the overlap of the time-dependent state and the spin-dependent $2h1p$ configuration.

$$A_{aij,s}(t) = \langle \psi(t) | \phi_{aij,s} \rangle \ . \tag{6.26}$$

Then the transition probability can be constructed from the transition amplitudes as follows:

$$P_{aij}(t) = \sum_s |A_{aij,s}(t)|^2 \ . \tag{6.27}$$

Note that, by taking the sum over spin configurations, the transition probability becomes a spinless quantity.

Figure 6.5 shows the transition probability for four different virtual orbitals (LUMO$_{A1}$, LUMO+1$_{A1}$, LUMO+2$_{A1}$, and LUMO+3$_{A1}$) at three different points in time (the transition probabilities for other virtual orbitals are zero). From this, we can see that a few elements of the transition probability have non-zero values, many of them are smaller than 0.01. For example, the transition probabilities for virtual orbital LUMO+3$_{A1}$ are smaller than 0.0001 and that is why this orbital does not contribute to the dynamics significantly (see Figure 5.5). On the other hand, we can find larger transition probabilities for other virtual orbitals. For instance, the transition probabilities for virtual orbital LUMO$_{A1}$ and LUMO+2$_{A1}$ are of order 0.1 for $i = 5$ (referred to Si_{2p} orbital) and $j = 10$ (referred to HOMO-4$_{A_1}$). In addition, for virtual orbital LUMO+1$_{A1}$ the transition probability is of order 0.01 when $i = 5$ and $j = 13$ (referred to HOMO-3$_{A_1}$). To gain an understanding of the underlying process, it is beneficial to take a closer look at the dynamics of the dominant transition probabilities. Figure 6.6 shows the time-evolution of the dominating elements of the transition probability. As we have mentioned above, only three of the transition probabilities belonging to the $2h1p$ configurations $|\phi_{L_{A1}Si_{2p}H-4_{A1}}\rangle$, $|\phi_{L+2_{A1}Si_{2p}H-4_{A1}}\rangle$, and $|\phi_{L+1_{A1}Si_{2p}H-3_{A1}}\rangle$, dominantly contribute to the dynamics. In addition, the element associated to the configuration $|\phi_{L+1_{A1}Si_{2p}H-3_{A1}}\rangle$ is one order of magnitude smaller than the other ones. In other words, the related transition to this configuration is significantly smaller than other configurations and corresponding orbitals do not contribute to the dynamics notably. It can

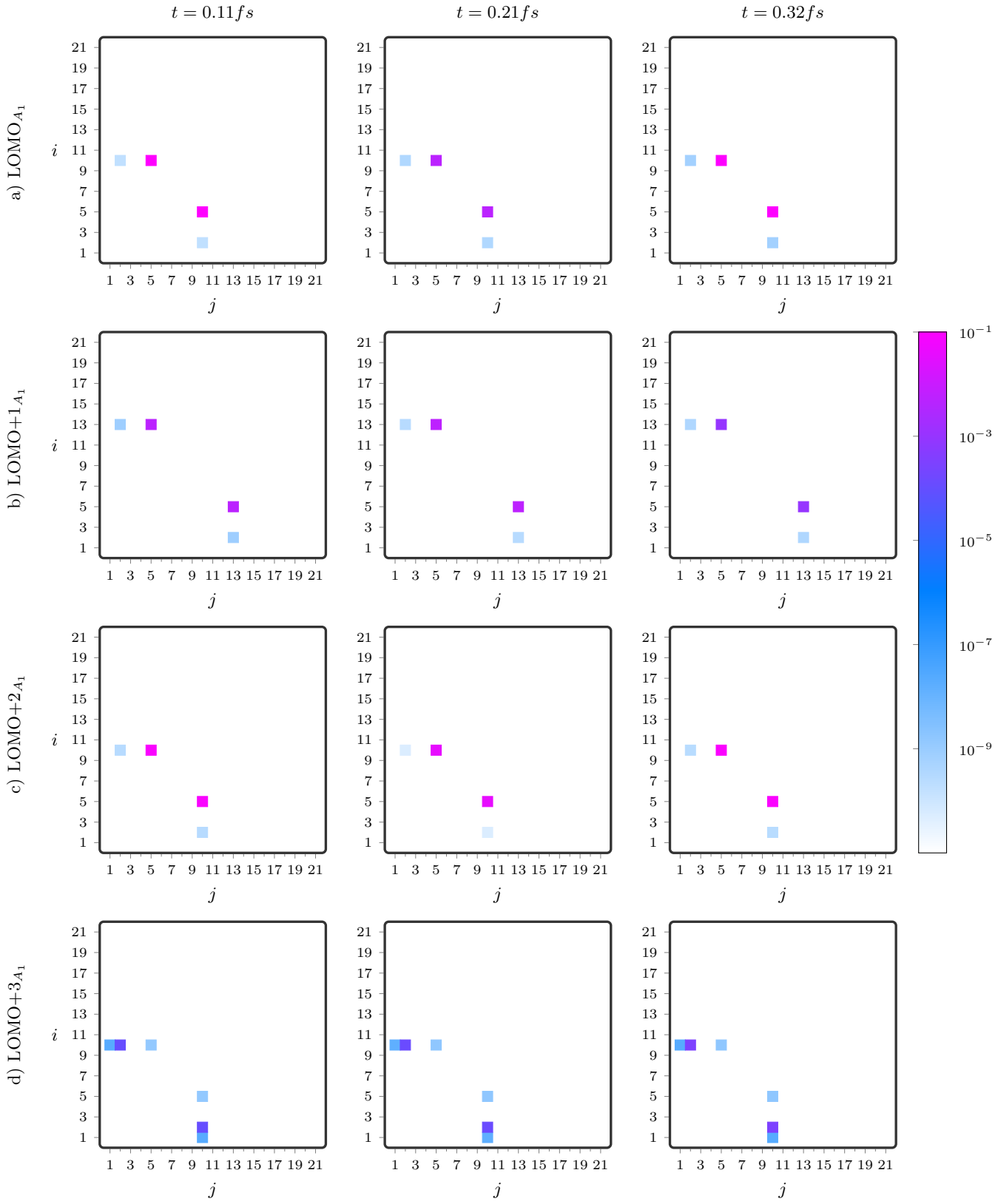

Figure 6.5: The transition probability after the prompt removal of an electron from $2p$ orbital of the silicon atom in silicon tetrafluoride for four different virtual orbitals (LUMO$_{A1}$, LUMO+1$_{A1}$, LUMO+2$_{A1}$, and LUMO+3$_{A1}$) at three different points in time. In this figure, the indices refer to the initially occupied molecular orbitals which are sorted based on their energies. The transition probabilities for other virtual orbitals are zero. Here, the noise prefactor = $10^{-3}, 10^{-6}, 0$ is employed in the sweep instruction and the many-body state is represented using the MPS approach with bond dimensions $D = 140$.

also be understood from Figure 5.6 where the HOMO-3$_{A_1}$ and LUMO+1$_{A_1}$ have negligible contribution to the dynamics in comparison with other contributed orbitals.

By Fourier transformation of the transition probabilities into the frequency domain, we can derive the frequencies which are present in those. Figure 6.7 shows the Fourier transform of the transition probability for the dominating $2h1p$ configurations indicated in Figure 6.6. The frequency-dependent transition probabilities for both of $2h1p$ configurations have three major peaks which are located at $\hbar\omega_1 = 9.66eV$, $\hbar\omega_2 = 19.32eV$, and $\hbar\omega_3 = 28.98eV$ respectively. It should be noted that the height of the first and third peak for the $|\phi_{L_{A1}Si_{2p}H-4_{A1}}\rangle$ configuration is smaller than the height of the second one. Therefore, the former ones have a small contribution. For that reason, the second frequency, $\hbar\omega_2 = 19.32eV$, is the dominant frequency in the corresponding transition probability.

In contrast to the transition probability regarding to the $|\phi_{L_{A1}Si_{2p}H-4_{A1}}\rangle$ configuration, the height of the major peaks observed in the Fourier transformation of the transition probability for configuration $|\phi_{L+2_{A1}Si_{2p}H-4_{A1}}\rangle$ are comparable to each other. However, the second peak is related to the main frequency of the transition probability while other ones also have a significant contribution in the time-dependent behavior. Hence, one can interpret the beating pattern observed in the transition probability of $|\phi_{L+2_{A1}Si_{2p}H-4_{A1}}\rangle$ configuration as well as dynamics of the occupation number of LUMO+2$_{A_1}$ (see Figure 5.7) using the contribution of these frequencies. Moreover, the main peak of the Fourier transform of the transition probabilities, $\hbar\omega_2 = 19.32eV$, perfectly fits the energy difference between cationic eigenstates which is observed in Figure 6.4. Roughly speaking, it means that the satellite state $|I_s\rangle$ can be interpreted as a linear combination of $|\phi_{L_{A1}Si_{2p}H-4_{A1}}\rangle$ and $|\phi_{L+2_{A1}Si_{2p}H-4_{A1}}\rangle$ configurations.

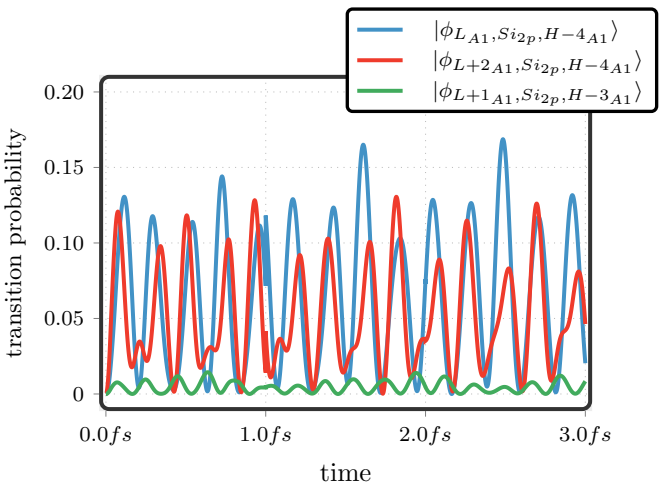

Figure 6.6: The time-dependent transition probability after the prompt removal of an electron from the $2p$ orbital of silicon atom in silicon tetrafluoride for the dominant $2h1p$ configurations.

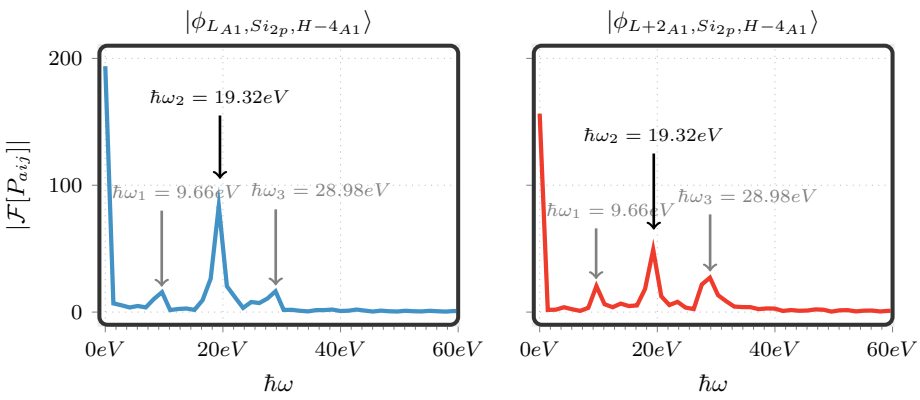

Figure 6.7: Fourier transform of the transition probability for the dominant $2h1p$ configurations $|\phi_{L_{A1}Si_{2p}H-4_{A1}}\rangle$ (left) and $|\phi_{L+2_{A1}Si_{2p}H-4_{A1}}\rangle$ (right). In this calculation, the frequency resolution is $1.38eV$.

6.6 Impact of Nuclear Geometry

So far, we have characterized the electron dynamics in the silicon tetrafluoride molecule using fixed molecular geometry that stays constant during the investigation period. This assumption has been made based on the Born-Oppenheimer Approximation (see Section 2.2) i.e. since the nuclei are heavier than the electrons, the electrons move much faster than the nuclei, and considering static molecular geometry is a valid assumption.

Recently, a series of theoretical studies [176, 186–188] has investigated the impact of the finite width of the wave packet of the nuclei on electronic dynamics in the molecules. These studies show that the spatial delocalization of the nuclei induces dephasing that can lead to damping of the electronic charge migration. In these studies, to take into account the quantum nature of the nuclei approximately, the nuclear positions within the width of the Gaussian wave packet of the nuclear ground state have been considered and the resulting electron dynamics has been averaged. This consideration gives rise to a superposition of coherent oscillations with various oscillation periods that average out within a few femtoseconds. It should be noted that the cationic spectrum at the different nuclear geometries is different and it leads to the cancellation of the oscillations in the averaged dynamics. Therefore, it served as a motivation for us to study the impact of this nuclear induced dephasing of the charge migration discussed previously.

To investigate the influence of the nuclear geometry on the above-discussed charge migration in the silicon tetrafluoride molecule, let us start with considering an artificial molecular geometry where the length of one of the Si-F bonds is not fixed and can change (see Figure 6.8). In this artificial geometry, we only consider displacement of fluorine atoms, since these are the ones

whose ground state wave function has the largest spread. Furthermore, for the sake of simplicity, we only consider the impact of the displacement of one of the fluorine atoms on the electronic dynamics and assume other atoms are fixed.

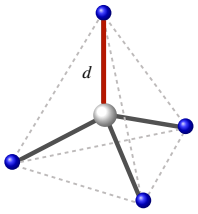

Figure 6.8: Silicon tetrafluoride molecule at an artificial molecular geometry. In this geometry one of the Si-F bonds is not fixed and its position can alter. The displacement of this bond is represented by d.

Let us introduce d as the bond distance between the silicon atom and the movable fluorine atom (see Figure 6.8). When the bond distance changes, the electronic ground state energy of the molecule changes and forms a potential energy surface as illustrated in Figure 6.9. The shape of this potential energy surface characterizes how strongly the fluorine atom is bound to the molecule and determines the width of the nuclear wave function. The wave function of the nuclei can be obtained by solving the Schrödinger equation with respect to the external potential which is given by the potential energy surface. From the nuclear wave function, which is shown in Figure 6.9, one can determine the spatial delocalization of the considered fluorine atom. To study the impact of displacement of this fluorine atom on the charge migration dynamics, we increase d from its equilibrium by 1%, i.e we stretch one of the Si-F bonds by 1%, and then carry out a charge migration calculation using the MPS method.

Figure 6.10 indicates the partial hole charge at the silicon atom and the tetrafluoride part of the silicon tetrafluoride molecule after sudden ionization of the $2p$ orbital of the silicon atom for equilibrium and artificially stretched molecular geometry. It is obvious that in the stretched molecule, the charge migration still survives, but its oscillation period is enhanced, i.e. by stretching one of the Si-F bonds by 1%, the charge migration slowed down by 5%. Note that the nature of the electron dynamics does not change in the stretched geometry. Figure 6.11 shows the time-evolution of the occupation number of the initial hole plus the molecular orbitals which contribute dominantly to the dynamics. Similar to the equilibrium geometry in the stretched geometry, the occupation number of the initial hole does not alter and the initial hole

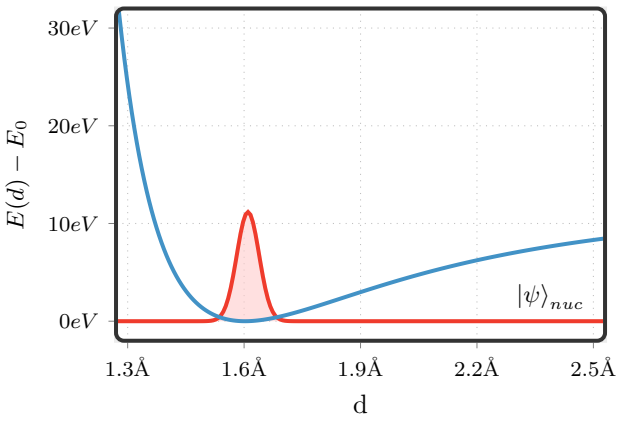

Figure 6.9: Potential energy surface of the HartreeFock ground state with respect to one of the silicon-fluorine bond lengths (blue). For specific fluorine atom, a nuclear wave function (red) with finite width is develops in this potential energy surface.

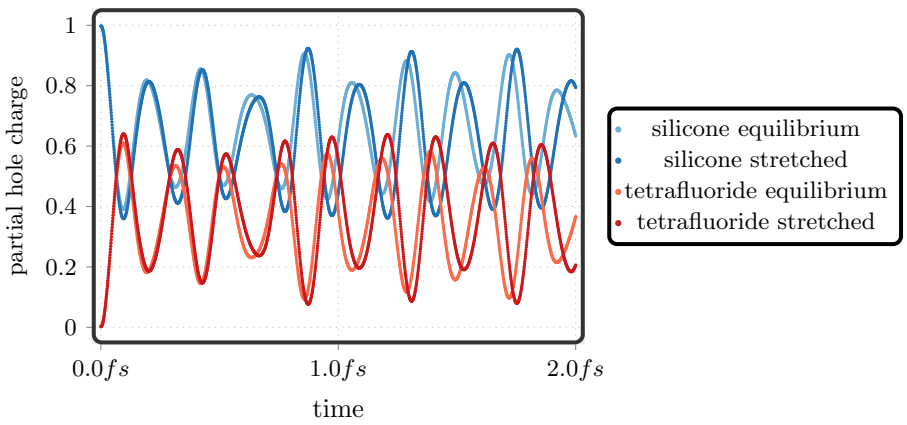

Figure 6.10: Time-dependent partial hole charge at the silicon atom and at the tetrafluoride part of the silicon tetrafluoride molecule for equilibrium and artificially stretched molecular geometry. Here, the noise prefactor $= 10^{-6}, 10^{-8}, 0$ in the sweep instruction is employed and the many-body state is represented using the MPS approach with bond dimensions $D = 120$.

remains unaffected during the dynamics. Furthermore, HOMO-4_{A1}, LUMO$_{A1}$, and LUMO+2_{A1} leave similar as before, they oscillatory contribute to the dynamics, but the oscillation period is slightly increased in comparison to the equilibrium molecular geometry. Therefore, we can deduce that stretching of one of the Si-F bonds in the silicon tetrafluoride molecule leads to a change of the oscillation period of the charge migration, but underlying dynamics does not change. It means, if one considers the ionization spectrum of the stretched geometry, there are still two lines corresponding to the main state and a satellite state, but the energy gap between these states is different in comparison to the equilibrium geometry.

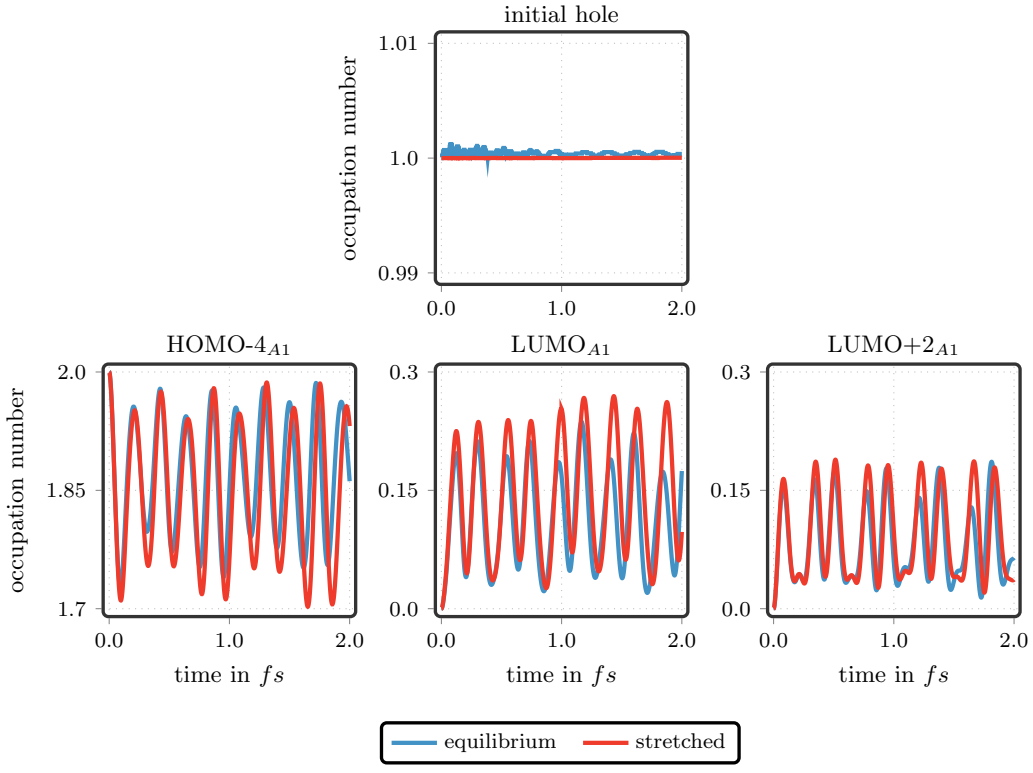

Figure 6.11: Time-evolution of the occupation number of the molecular orbitals which are dominantly involved in the dynamics for equilibrium and stretched molecular geometry.

Until now, to investigate the impact of the nuclear geometry on the charge migration in the silicon tetrafluoride molecule, we have only considered the role of one of the fluorine atoms by introducing one simple artificial molecular geometry where the Si-F bond is not fixed and can alter. We took into account this modification under the assumption that the lightest nucleus in the molecule has the broadest wave function spread. This assumption does not reflect all the physical realities. That is why we would like to use the molecular vibration approach and consequently the *normal mode* concept to study the impact of the nuclear geometry on charge migration.

6.7 Molecular Vibration

In general, molecular vibrations describe the harmonic motion of the atoms in a molecule relative to one another, where the center of mass of the molecule stays fixed. Commonly, vibrations of polyatomic molecules are characterized in terms of the normal modes. Normal modes describe the pattern of independent vibrational motion of atoms in the molecule that happen without moving to any other ones. Normally, for a non-linear molecule with N atoms, there are $3N-6$ normal modes of vibration, whereas a linear molecule has $3N-5$ normal modes [189].

To investigate the molecular vibration in terms of the normal modes, let us start with expanding the nuclear Hamiltonian (Equation 2.10) around the equilibrium position of the nuclei R_{eq}.

$$\hat{H}_n = \sum_i -\frac{\hbar^2}{2M_i}\frac{\partial^2}{\partial^2 R_i} + E_e(R_i) \tag{6.28}$$

$$= \sum_i -\frac{\hbar^2}{2M_i}\frac{\partial^2}{\partial^2 x_i} + E_e(R_{eq}) + \sum_i \left(\frac{\partial E_e}{\partial x_i}\right)_0 x_i + \frac{1}{2}\sum_{ij} k_{ij}x_i x_j \tag{6.29}$$

Here the displacement from the equilibrium position of the nucleus is defined as $x_i = R_i - R_{eq}$ and subscript 0 denotes that the derivatives are to be assessed at the equilibrium position (at $x_i = 0$). Additionally, the first derivatives are all zero at equilibrium (all $x_i = 0$) because there is a minimum at the equilibrium position of nuclei on the potential energy surface. Moreover, the *force constant*,

k_{ij}, is defined as:

$$k_{ij} = \left(\frac{\partial^2 E_e}{\partial x_i \partial x_j}\right)_0 \tag{6.30}$$

From the definition of the k_{ij}, one can understand that a displacement of one atom can affect restoring forces experienced by the other atoms. It is worth mentioning that the sum in Equation 6.29 is overall $3N$ displacements of the N atoms, but some displacements, which are related to the translation (3 displacements) and rotation (3 displacements) of the molecule, have zero force constant. Therefore, it is essential to distinguish these zero force constant displacements from the real vibrations.

To simplify the problem one can introduce the *mass weighted normal mode coordinates*. These are defined in terms of the *mass weighted coordinates* $q_i = \sqrt{M_i} x_i$ by the linear equation

$$Q_k = \sum_i l_{ki} q_i \tag{6.31}$$

where l_{ki} are the eigenvectors of the mass weighted force constant matrix K which is defined as:

$$K_{ij} = \left(\frac{\partial^2 E_e}{\partial q_i \partial q_j}\right)_0 \tag{6.32}$$

Using mass weighted normal mode coordinates, Hamiltonian in Equation 6.29 turns into [2] :

$$\hat{H} = E_0 + \sum_i -\frac{\hbar^2}{2}\frac{\partial^2}{\partial^2 Q_i} + \frac{1}{2}\sum_i \lambda_i Q_i^2 \tag{6.33}$$

[2] For simplification we write $E_e(R_{eq}) = E_0$

where λ_i are the eigenvalues of the mass weighted force constant matrix and are directly related to the frequency of the mass weighted normal mode i as:

$$f_i = \frac{\sqrt{\lambda_i}}{2\pi} \tag{6.34}$$

consequently, the wavenumber related to the mass weighted normal mode i is given by

$$\nu_i = \frac{\sqrt{\lambda_i}}{2\pi c} \tag{6.35}$$

Where c is the speed of the light.

We have to mention that using the mass weighted normal mode coordinate leads to disappearing cross terms in the Hamiltonian and thus one can rewrite the Hamiltonian as the independent terms.

$$\hat{H} = E_0 + \sum_i h_i \tag{6.36}$$

$$h_i = \sum_i -\frac{\hbar^2}{2}\frac{\partial^2}{\partial^2 Q_i} + \frac{1}{2}\sum_i \lambda_i Q_i^2 \tag{6.37}$$

We have seen that by constructing the mass weighted force constant matrix and diagonalizing, the normal modes and corresponding frequency and wavenumber can be derived. Also, we have understood that the number of normal modes for a nonlinear molecule with N atoms is given by $3N - 6$. For example, silicon tetrafluoride which consists of 5 atoms, in total has 9 normal modes some of those, depending on the geometry and symmetries of the molecule, degenerate. Figure 6.12 illustrates the normal modes of the silicone tetrafluoride molecule where the symmetric stretch normal mode is nondegenerate, symmetric bend normal mode is doubly degenerate, and asymmetric stretch and asymmetric bend normal modes are triply degenerate. In order to determine the normal modes and corresponding wavenumber, we employed the quantum chemistry program package Molpro [168]. The wavenumber of the different normal modes of the SiF_4 molecule are summarized in Table 6.2. Furthermore, the Hartree-Fock ground state of the SiF_4 molecule with respect to the displacement of the different normal modes coordinates is illustrated in the Figure 6.13. From these potential energy surfaces, it can be understood that the asymmetric stretch normal modes are the fastest ones and consequently nuclear wave functions with respect to these normal modes have the smallest width.

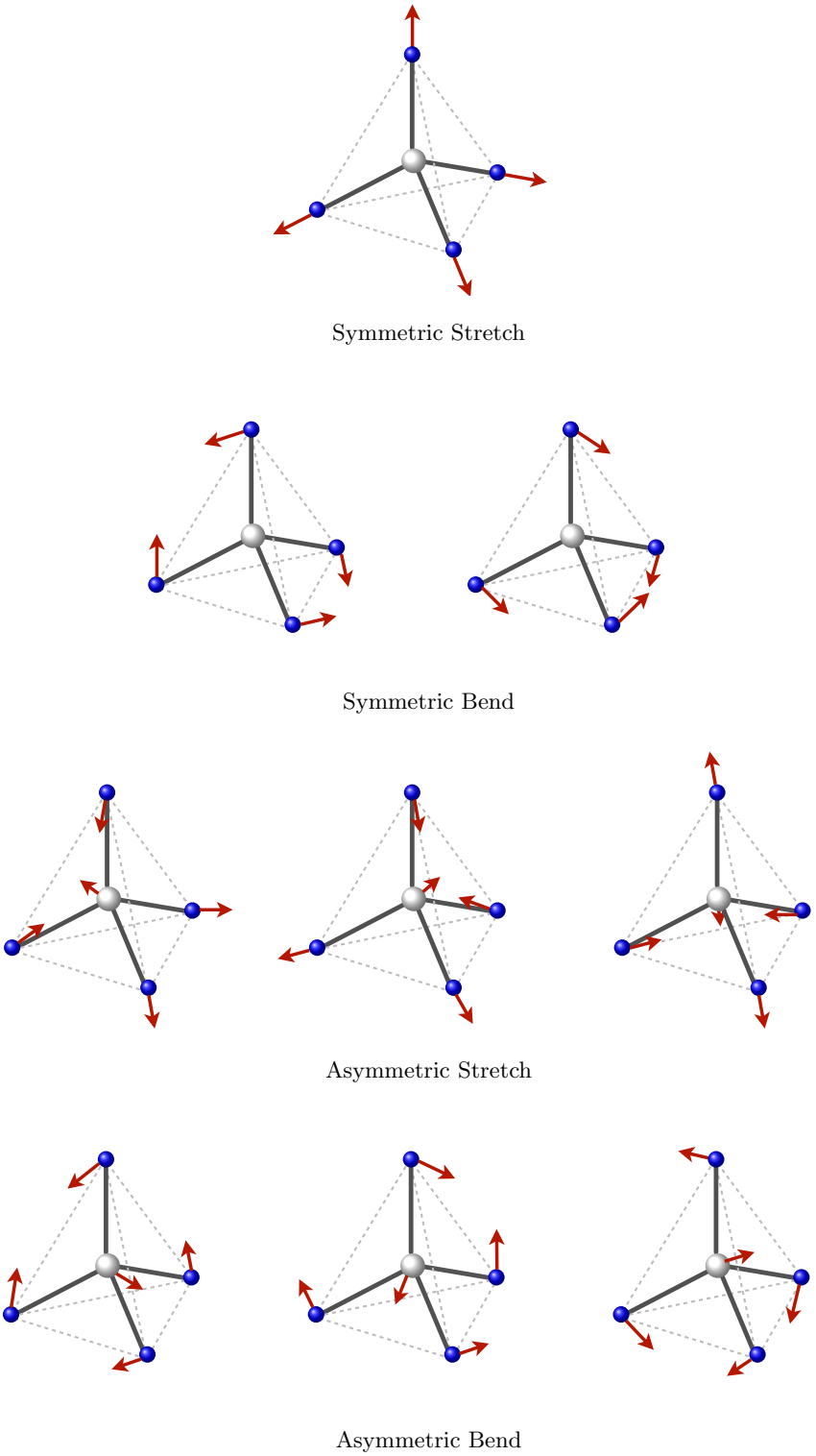

Figure 6.12: The normal modes of the silicone tetrafluoride molecule where the symmetric stretch normal mode is nondegenerate, symmetric bend normal mode is doubly degenerate and asymmetric stretch and asymmetric bend normal modes are triply degenerate. Arrows demonstrate the relative displacement of the atoms in a mass weighted coordinate system, q_i, when the molecule vibrates.

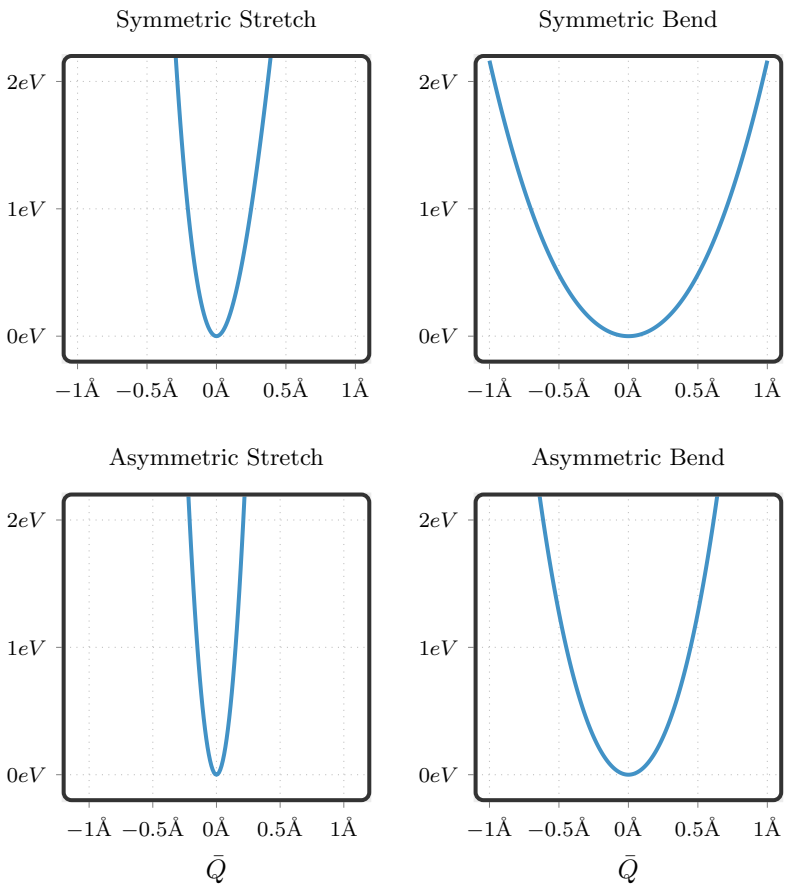

Figure 6.13: Potential energy surface of the Hartree-Fock ground state of the SiF_4 molecule with respect to the displacement of the different normalized normal mode coordinate $\bar{Q}$.

Normal mode	Wavenumber (cm^{-1})
Symmetric Stretch	751.07
Symmetric Bend	228.66
Asymmetric Stretch	1026.87
Asymmetric Bend	350.49

Table 6.2: The wavenumber of the different normal modes of the SiF_4 molecule. To achieve the normal modes and corresponding wavenumbers, the quantum chemistry program package Molpro [168] is used.

As we mentioned before, in order to take into account the quantum nature of the nuclei on the charge migration after sudden ionization in the molecules, sampling the nuclear position within the width of the Gaussian wave packet of the nuclear ground is required. It means that to investigate the impact of the delocalization of the nuclei on the charge migration one should first consider different nuclear geometries corresponding to displacements along with different vibrational modes of the molecule and then perform a charge migration calculation and finally take the average with respect to the probability of the nuclear geometries.

In Section 3.6, we have seen that exploiting the point group symmetry describing the spatial symmetry of the molecule leads to simplification of the MPS representation of the many-body state and one can rewrite the MPS tensors $A[i]$ in block diagonal form reflecting the irreps of the symmetry point

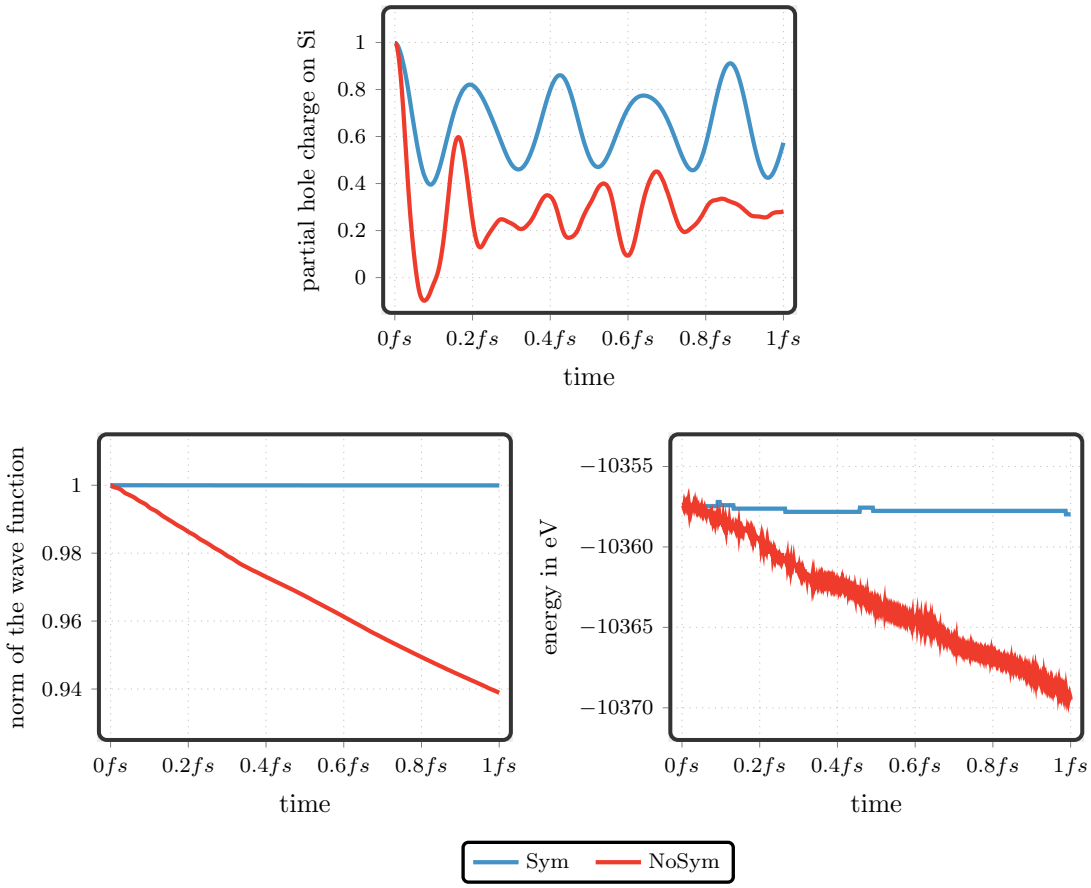

Figure 6.14: (top) Time-dependent partial hole charge at the silicon atom and at the tetrafluoride part of the silicon tetrafluoride molecule. (bottom left) Norm of the wave function as a function of time. (bottom right) Energy of the system as a function of time for Sym and NoSym cases. The noise prefactor = $10^{-3}, 10^{-6}, 0$ is used in the sweep instruction and the many-body state is represented using the MPS approach with bond dimensions $D = 140$.

group. On the one hand, simplification of the MPS representation by employing spatial symmetry of the molecule (or other symmetry of the quantum chemical systems) results in improved convergence behavior. In this case, we basically aided the variational optimization to focus on the states that follow the symmetries of the system. On the other hand, small displacement along the normal modes of the molecule can lead to a reduction of the geometrical symmetry of the molecule. The performance of our MPS approach depends on the symmetry group of the molecule, therefore, we expect that our MPS approach can not resolve the correct dynamics in situations where the spatial symmetry of the molecule is reduced.

For example, Figure 6.14 (top) shows the time-evolution of the partial hole charge on the Si atom in the silicon tetrafluoride molecule based on the two different situations, Sym and NoSym. In such situations, we have considered C_{2v} and C_1 as the point groups of the molecule in the equilibrium geometry and did the charge migration calculation using the MPS approach. Since point group C_1 is the point group with the lowest symmetry and only includes

the identity as symmetry element, we called it NoSym case, and since C_{2v} is the highest symmetry point group which we can employ for the silicon tetrafluoride molecule, we called it Sym case for simplicity.

For the NoSym case, the partial hole charge on the silicon atom intensively oscillates within $0.2fs$, but after this time period, it seems to be damped. We have seen the same behavior for the irrep orbital ordering (see Figure 5.3) where the dominant dynamics was oscillatory, but after one time period (around $0.2fs$) the oscillation was damped out. In this case, the damping of the dynamics is an artifact of orbital ordering and by reordering the orbitals and putting the strongly correlated orbitals close to each other, one can resolve the correct dynamics.

In the NoSym case, as before, the damping of the partial hole charge dynamics is an artifact due to the long-range coherences in the system. Since the C_1 symmetry point group consists of only one irrep, there are no zero elements among the non-diagonal elements of the OERDM, which hold electronic coherences, hence, the long-range coherences in the system are maximal. Furthermore, in the molecule with C_1 symmetry point group, the norm of the wave function and energy of the system are not conserved during the dynamics. From Figure 6.14 (bottom) one can understand that in contrast to the calculation with the C_{2v} symmetry point group, in the NoSym case, the norm of the wave function and the energy of the system change with time and are not conserved due to the electronic coherences which appear in the system. Therefore, reduction of the symmetry point group of the molecule leads to an introduction of artificial electronic coherences in the system which spoils our MPS approach performance.

Moreover, one can clarify the role of the reduction of the symmetry point group on the performance of our MPS approach in terms of the dimension of Hilbert space. In Section 3.6, we saw that employing the point group symmetry results in a reduction of the dimension of the Hilbert space. For example, if one ignores any geometrical symmetry of SiF_4 and employs C_1 symmetry (NoSym case) then full CI bond dimension is as large as $D_{FCI} = 213,005,990$ whereas by employing C_{2v} it reduces to $D_{FCI} = 57,183,556$. In other words, by employing C_2 the dimension of the effective many-body Hilbert space reduces significantly. Therefore, in the NoSym case, we need to increase the necessary bond dimension to obtain correct results. It means when one keeps the bond dimension fixed the truncation error in the NoSym case is much larger than in the Sym case which spoils the results. Therefore, to consider the impact of

Geometry	Atom	x	y	z
#1	Si	0.0	0.0	0.0
	F_1	1.246	0.0	1.047
	F_2	-1.246	0.0	1.047
	F_3	0.0	1.246	-1.047
	F_4	0.0	-1.246	-1.047
#2	Si	0.0	0.0	0.088
	F_1	1.419	0.0	0.904
	F_2	-1.419	0.0	0.904
	F_3	0.0	1.230	-0.969
	F_4	0.0	-1.230	-0.969
#3	Si	0.0	0.0	0.0
	F_1	1.386	0.0	0.980
	F_2	-1.386	0.0	0.980
	F_3	0.0	1.386	-0.098
	F_4	0.0	-1.386	-0.098
#4	Si	0.0	0.0	0.082
	F_1	1.286	0.0	0.906
	F_2	-1.286	0.0	0.906
	F_3	0.0	1.363	-0.967
	F_4	0.0	-1.363	-0.967

Table 6.3: The actual nuclear positions used for four different geometries. The coordinates are given in angstrom.

the nuclear geometry on the charge migration in silicon tetrafluoride, instead of sampling the nuclear geometries to mimic spatial nuclear delocalization, we only consider geometries that conserve the symmetry point group of the molecule. It means, we restrict ourselves to a few nuclear geometries and ignore a significant number of geometries which would be achievable by displacing the nucleus along with the normal modes. To obtain such geometries, we consider normal modes where the displacement of the nuclear positions does not reduce the symmetry point group of the molecule and then displace the nuclear positions along with the normal mode coordinates. So that the probability density of the nuclear wave function equals 0.89. The actual nuclear positions used for four different geometries are given in Table 6.3.

Results of the charge migration calculation for different nuclear geometries are illustrated in Figure 6.15. These results show that the time period of the partial hole charge at the silicon atom changes with respect to the geometry of the nucleus. For example, the time period of the above mentioned dynamics for different nuclear geometries is $T_1 = 0.180 fs, T_2 = 0.165 fs, T_3 = 0.217 fs, T_4 = 0.215 fs$. (Keep in mind that the time period of the dynamics corresponding to equilibrium geometry is $0.21 fs$.) Consequently, if one samples the nuclear

positions within the width of the Gaussian wave function of the nuclear ground state, a damping of the electronic charge migration is to be expected. Furthermore, Figure 6.15 shows the hole population on the silicon atom for the NoSym case where the C_1 point group is employed. In this case, same as before, dynamics are damped with time due to the artificial electronic coherences which are induced in the system as a result of using C_1 point group. In addition, Figure 6.16 and Figure 6.17 depict the the energy of the system and the norm of the wave function as a function of the time for different nuclear geometries. As we expect, in the NoSym case, the norm of the wave function and the energy of the system change with time and are not conserved. These results are another evidence of the dependency of the performance of our MPS approach on the used symmetry point group.

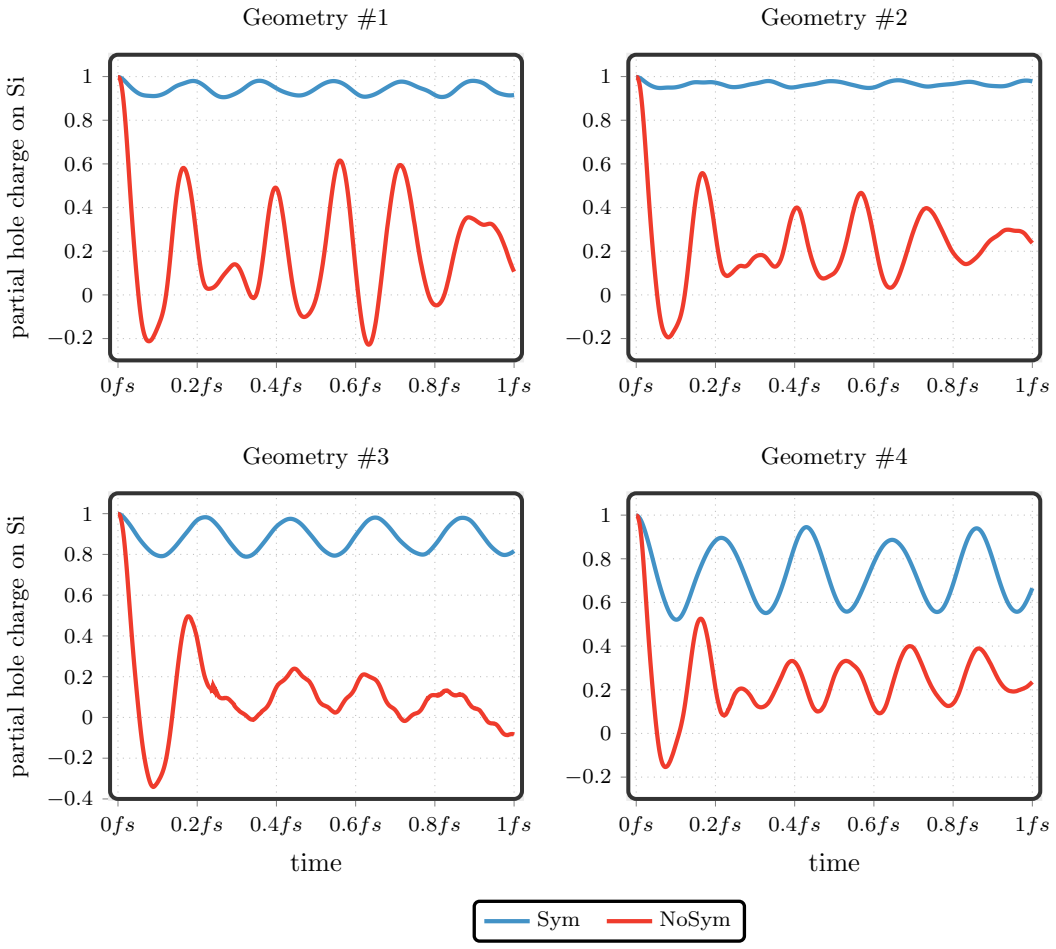

Figure 6.15: Time-dependent partial hole charge at the silicon atom of the silicon tetrafluoride molecule for different nuclear geometries and for Sym and NoSym cases. Here, the noise prefactor = $10^{-3}, 10^{-6}, 0$ is used in the sweep instruction and the many-body state is represented using the MPS approach with bond dimensions $D = 140$.

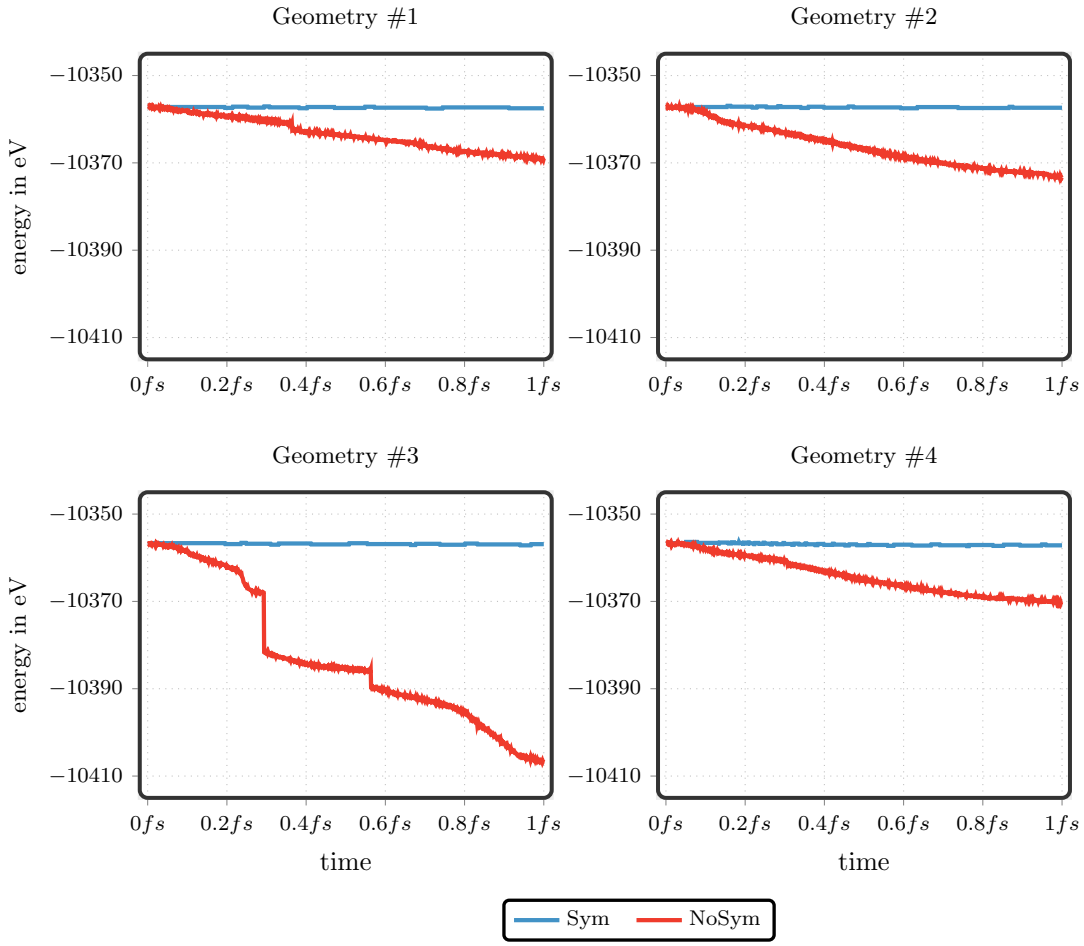

Figure 6.16: Energy of the system as a function of time for different nuclear geometries and for the Sym and NoSym case.

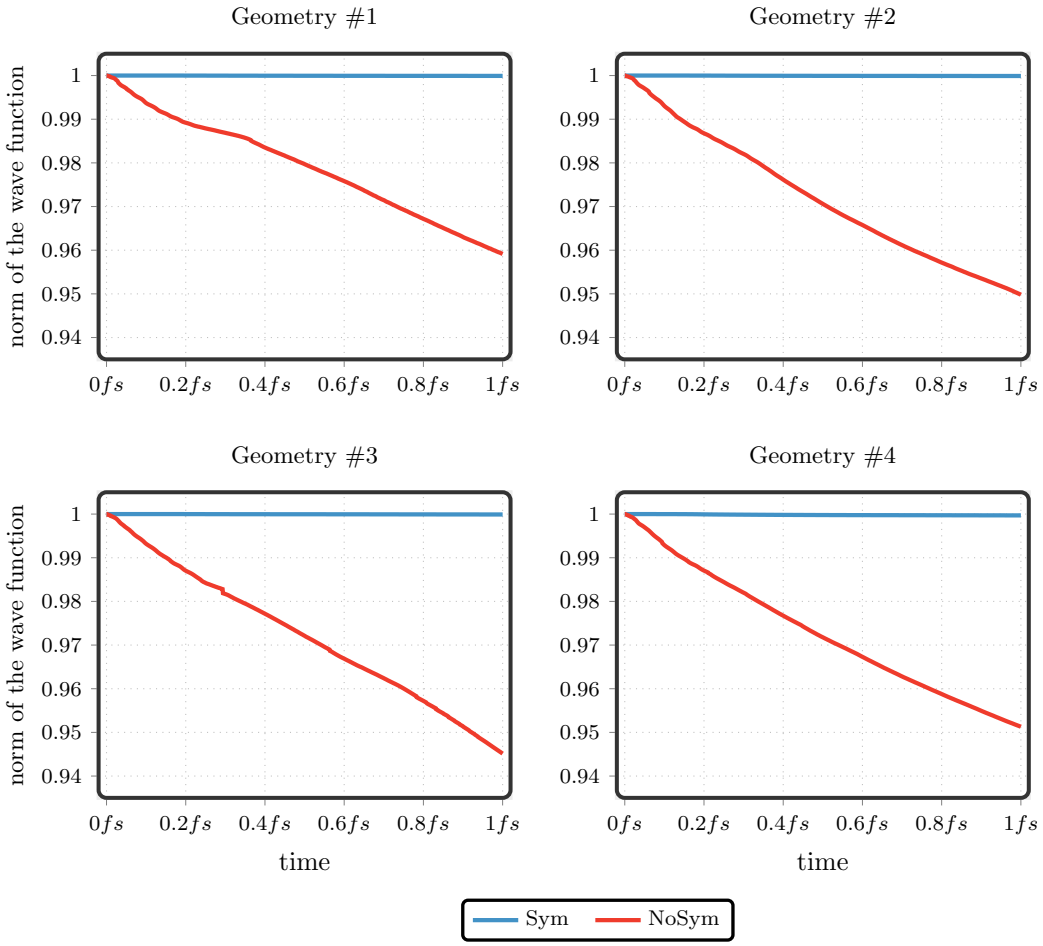

Figure 6.17: Norm of the wave function as a function of time for different nuclear geometries and for the Sym and NoSym case.

6.8 Conclusions

In Chapter 5, we understood that the ionization of the $2p$ orbital of the silicon atom triggers the electron dynamics in the valence orbitals while the created hole in the core does not alter during the process up to $3fs$ after ionization. In this chapter, we aimed to analyze the electron dynamics in the core ionized silicon tetrafluoride. We demonstrated that the above-mentioned dynamics in the valence orbitals lead to the migration of the hole charge between the silicon atom and the tetrafluoride part on a time scale of $0.21fs$ which is faster than the decay time of the core electron by an Auger process. Moreover, we showed that the time period of the charge migration can be extracted from the energy-dependent autocorrelation function which includes the correlated states of the cation. In addition, our analysis based on the transition probabilities indicated that only two $2h1p$ configurations contribute the most to the dynamics which is in agreement with results obtained from the dynamics of the occupation number of the molecular orbitals. Lastly, we discussed the impact of the geometry of the molecule on the charge migration, most importantly by introducing two approaches. First, we stretched one of the fluorine atoms artificially, and second, considering small displacements along with the normal modes of the molecule. The results obtained for the different molecular geometries showed that small displacements along the normal modes lead to an alteration of the time period of the charge migration which can give rise to a damping of the charge migration if one accounts the finite width of the nuclear wave function same procedure as discussed in [176].

Conclusions and Outlook

7

In this thesis, we used the time-dependent MPS approach to study molecular inner-shell processes. We specifically investigated the correlation-driven electron dynamics in the core ionized silicon tetrafluoride molecule and demonstrated how the core ionization triggers ultrafast electron dynamics in the valence shell of the molecule. Furthermore, we studied the role of orbital ordering and numerical noise in the time-dependent MPS approach.

Summary

In Chapter 1, we outlined some theoretical methods to describe ultrafast processes in molecular systems. In addition, we outlined the time-dependent MPS method developed by Frahm and its implementation in the Hamburg CheMPS2 extension.

The basic concepts of the ab initio quantum chemistry were introduced in Chapter 2. We outlined Born-Oppenheimer approximation as well as the Hartree-Fock method as the simplest method to describe many-body wave functions in an uncorrelated fashion. In addition, we discussed the configuration interaction as a post-Hartree-Fock method to expand the many-body wave function in terms of the excited determinants.

We reviewed the general theory of MPS in the context of quantum chemistry in Chapter 3. In this chapter, the MPS formalism is introduced as a general representation of the many-body state. We discussed how exploitation of the symmetries of the quantum chemical Hamiltonian leads to a reduction of the dimension of the desired many-body Hilbert space and a simplification of the MPS tensors.

Next, in Chapter 4, the time-evolution of MPS to describe the time-dependent phenomena in the quantum chemical systems was outlined. First, we reviewed the Krylov space time-evolution method as the main time-dependent method which was used through this thesis. Further, we discussed the variational optimization procedure to perform operations (addition or operator application). We finished this chapter with some remarks on how to improve the performance of the variational optimization procedure. We introduced two-site

object, numerical random noise, and sweep schedule as the main tactics which can lead to an improvement of the optimization procedure.

We applied the time-dependent MPS approach to investigate the correlated electron dynamics in core ionized silicon tetrafluoride molecule in Chapter 5. We studied the electron dynamics after a sudden ionization of the $2p$ orbitals of the silicon atom in silicon tetrafluoride. We understood that orbital ordering plays a crucial role in the performance of the MPS approach. In a first attempt, we ordered the orbitals based on their irreps and their energies. We noticed that employing such orbital ordering spoils the performance of the MPS approach in the case of core ionization of SiF_4 and the dynamics do not converge even after increasing the MPS bond dimensions within the range of 100 to 180. It seems to obtain converged results, much larger bond dimensions are required which is not feasible practically.

We found out that if one puts the strongly correlated orbitals close to each other in the one-dimensional arrangement of system sites, then the non-local properties of the system which are artificially exaggerated by the inappropriate ordering of the orbitals disappear. Resolving the correct dynamics then becomes feasible with a reasonably large MPS bond dimension. We concluded that, unlike the ordering of the orbitals based on the irreducible representations, an MPS bond dimension of $D = \mathcal{O}(100)$ is sufficient to resolve the dynamics in this case. Further, we investigated the role of the numerical noise which was introduced in the variational optimization of the MPS. By performing quantitative analysis, we demonstrated that this concept can lead to an enhancement of the efficiency of the MPS approach by improving the convergence rate of the dynamics in terms of the MPS bond dimension.

In Chapter 6, we demonstrated that ionization of the $2p$ orbital of the silicon atom in the silicon tetrafluoride molecule triggers intense and fast electron dynamics in the valence orbitals while the initial core hole does not change during this initial process. We showed that this process results in a charge migration between the silicon atom and the tetrafluoride part on a time scale of $0.21\,fs$ which is faster than the decay time of the core electron by an Auger process. To understand the origin of the time period of the charge migration, we analyzed the dynamics in terms of the energy-dependent autocorrelation function and transition probability and identified the correlated cationic eigenstates which are responsible for the charge migration. We showed that the time period of the charge migration can be extracted from the energy-dependent autocorrelation function which includes the correlated states of

the cation. In addition, our analysis based on the transition probabilities indicated that only two $2h1p$ configurations had a dominant contribution to the dynamics which is in agreement with the results obtained from the dynamics of the occupation numbers of the molecular orbitals.

Finally, we studied the role of the nuclear geometry on the charge migration in SiF_4 by considering two approaches. First, we considered stretching one of the fluorine bonds artificially, and second, we examined a small displacement along with the normal modes of the molecule. We noticed that the small displacement along the normal modes leads to an altering of the time period of the charge migration which can give rise to a damping of the charge migration if one accounts for the finite width of the nuclear wave function. We observed that due to the computational restrictions of our MPS approach, considering the finite width of the nuclear wave function reliably is not possible.

Outlook

In this thesis, we studied the electron dynamics following core ionization in SiF_4. We found out that the triggered dynamics leads to an intense and ultrafast charge migration in the system which is faster than the decay time of the core electron by an Auger decay. Auger decay [190] is one of the best studied processes in light-induced electron emission and is the most direct probe of electron-electron interaction in atoms and molecules where the filling of the inner-shell vacancy of an atom or molecule is accompanied by the emission of the secondary electron. This process has commonly been described with the help of decay rates [191–197], but in recent years, the study of the real-time dynamics of this process has attracted attention [198–200]. Generally, Auger relaxation times are in the interval of hundreds of attoseconds to a few femtoseconds and principally our MPS approach is able to model this process.

To model Auger decay theoretically, it is essential to have a good description of the continuum [198]. For this reason, it is common practice to employ basis sets that consist of diffuse functions to describe the emitted electron. For example, it is shown [175, 201] that the valence electrons from the fluorine atoms of silicon tetrafluoride play an important role in the Auger decay of the silicon $2p$ hole, therefore, to mimic the Auger decay in the silicon tetrafluoride it is important to include some diffuse functions on the fluorine atoms in the basis set.

Roughly speaking, applying such kind of basis sets enlarges the dimension of the many-body Hilbert space significantly and makes the treatment of the electron dynamics using our MPS approach computationally challenging or even impossible. In the following, we outline some ideas for future development of the MPS approach, especially, to make the study of the real-time dynamics of the Auger process in the molecular system possible.

In Chapter 2, we have mentioned that to reduce the dimension of the many-body Hilbert space and thereby the required computational resources in the CI method, a truncation of the CI space concerning the excitation level is commonly used. On the other hand, we have understood that the MPS approach incorporates n-fold excitations into the wave function to approximate the full CI state. Therefore, it is beneficial to combine the MPS ansatz with the restricted excitation approach to reduce the computational cost. This combination has already been incorporated by Schaub into the Hamburg CheMPS2 extension [49], but in his implementation, he only considered the single and double excitation and ignored exploiting the point group symmetry. In Chapter 3 and Chapter 6, we have observed that the exploitation of the geometrical symmetry of the molecule reduces the dimension of the many-body Hilbert space and improves the performance of the MPS approach. Therefore, generalizing Schaub's implementation to a higher excitation level (e.g. triple, quadruple, and so on) while the geometrical symmetry of the molecule is imposed would allow treating electron dynamics in more complicated systems with the time-dependent MPS approach.

Further, as we have mentioned in Chapter 3, Hamburg CheMPS2 code can only deal with abelian point groups whereas several molecules exhibit non-abelian point groups. For example, centrosymmetric linear molecules such as acetylene , C_2H_2, diacetylene , C_4H_2, and carbon suboxide , C_3O_2 belong to $D_{\infty h}$ molecular point group which is non-abelian. Additionally, highly symmetric molecules such as tetrahedral and octahedral ones exhibit none-abelian point groups. Therefore, the implementation of the non-abelian point groups can enhance the capabilities of the MPS approach.

Another direction to increase the capabilities of the MPS approach of treating the electron dynamics in the molecular system is to incorporate new algorithms to order the orbitals in the one-dimension arrangement. In Chapter 6, we have understood that the orbital ordering plays a crucial role in the performance of the time-dependent MPS approach. We have seen that putting strongly correlated orbitals close to one another in a one-dimensional lattice leads to

a reduction of the non-local properties of the system, and thus the efficiency of our MPS approach significantly improves. This kind of orbital ordering is inspired by the DMRG algorithms where the Fiedler ordering is utilized to increase the efficiency. So far, a variety of methods to sort the orbitals on the one-dimensional lattice in DMRG algorithms has been proposed [148, 169, 171, 202] of which the methods according to orbital entropies and methods based on the genetic algorithms have been demonstrated to be very efficient. Therefore, it would be of great benefit to incorporate the above-mentioned methods into the time-dependent MPS approach to enhance the performance and accuracy of this method.

Appendix

A

A.1 Dynamics Following the Ionization of Degenerated Orbitals

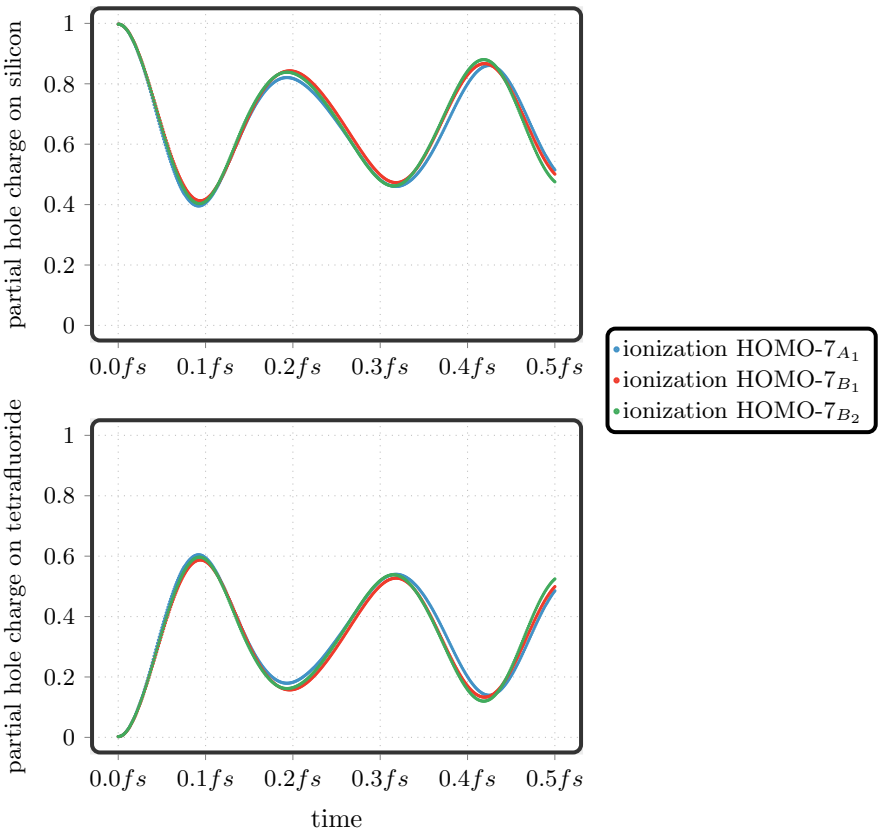

Figure A.1: Time-dependent partial hole charge at the silicon atom, (top) and tetrafluoride part (bottom) of the silicon tetrafluoride molecule after ionization of the HOMO-7 orbital with different irreducible representation. Resulting dynamics after ionization of the degenerated orbitals are physically similar, but the small divergence in the longer time period comes from the order of the orbitals in the one-dimensional lattice (see Table 5.1). The time-evolution is done using the Krylov space method with a Krylov space dimension $N_K = 6$ and a time step size $\delta t = 1as$. Also, the noise prefactor = $10^{-3}, 10^{-6}, 0$ is used. The many-body state is represented using the MPS approach with bond dimensions $D = 140$.

Bibliography

[1] Wolfgang Pauli. 'Über das Wasserstoffspektrum vom Standpunkt der neuen Quantenmechanik'. In: *Zeitschrift für Physik A Hadrons and nuclei* 36.5 (1926), pp. 336–363 (cited on page 1).

[2] Lucy Mensing. 'Die Rotations-Schwingungsbanden nach der Quantenmechanik'. In: *Zeitschrift für Physik* 36.11-12 (1926), pp. 814–823 (cited on page 1).

[3] SM Sze et al. *Physics of Semiconductor Devices*. 2018 (cited on page 1).

[4] Arnaldo Donoso and Craig C Martens. 'Simulation of coherent nonadiabatic dynamics using classical trajectories'. In: *The Journal of Physical Chemistry A* 102.23 (1998), pp. 4291–4300 (cited on page 1).

[5] Walter Heitler and Fritz London. 'Wechselwirkung neutraler Atome und homöopolare Bindung nach der Quantenmechanik'. In: *Zeitschrift für Physik* 44.6-7 (1927), pp. 455–472 (cited on page 1).

[6] Rienk van Grondelle. 'Photoinduced processes in nucleic acids and proteins: concluding remarks'. In: *Faraday discussions* 207 (2018), pp. 513–521 (cited on page 1).

[7] Marwa Abdelmouleh et al. 'Photoinduced Processes within Noncovalent Complexes Involved in Molecular Recognition'. In: *Chemistry-A European Journal* 26.10 (2020), pp. 2243–2250 (cited on page 1).

[8] Erik P Månsson et al. 'Real-time observation of a correlation-driven sub 3 fs charge migration in ionised adenine'. In: *Communications Chemistry* 4.1 (2021), pp. 1–7 (cited on page 1).

[9] Tobias Unruh, Luis I Domenianni, and Peter Vöhringer. 'Photo-induced primary processes of trans-[Co (acac) 2 (N3)(py)] in liquid solution studied by femtosecond vibrational and electronic spectroscopies'. In: *Molecular Physics* (2021), e1964043 (cited on page 1).

[10] Robert E Blankenship. *Molecular mechanisms of photosynthesis*. John Wiley & Sons, 2021 (cited on page 1).

[11] Hyunwoong Park et al. 'Photoinduced charge transfer processes in solar photocatalysis based on modified TiO 2'. In: *Energy & Environmental Science* 9.2 (2016), pp. 411–433 (cited on page 1).

[12] Albert Stolow, Arthur E Bragg, and Daniel M Neumark. 'Femtosecond time-resolved photoelectron spectroscopy'. In: *Chemical reviews* 104.4 (2004), pp. 1719–1758 (cited on page 2).

[13] Franck Lépine, Giuseppe Sansone, and Marc JJ Vrakking. 'Molecular applications of attosecond laser pulses'. In: *Chemical Physics Letters* 578 (2013), pp. 1–14 (cited on page 2).

[14] Mauro Nisoli et al. 'Attosecond electron dynamics in molecules'. In: *Chemical reviews* 117.16 (2017), pp. 10760–10825 (cited on page 2).

[15] Lorenz S Cederbaum and J Zobeley. 'Ultrafast charge migration by electron correlation'. In: *Chemical Physics Letters* 307.3-4 (1999), pp. 205–210 (cited on pages 2, 47).

[16] J Breidbach and LS Cederbaum. 'Migration of holes: Formalism, mechanisms, and illustrative applications'. In: *The Journal of chemical physics* 118.9 (2003), pp. 3983–3996 (cited on pages 2, 69).

[17] Milan Delor et al. 'Toward control of electron transfer in donor-acceptor molecules by bond-specific infrared excitation'. In: *Science* 346.6216 (2014), pp. 1492–1495 (cited on page 2).

[18] Manohar Awasthi, Yulian V Vanne, and Alejandro Saenz. 'Non-perturbative solution of the time-dependent Schrödinger equation describing H2 in intense short laser pulses'. In: *Journal of Physics B: Atomic, Molecular and Optical Physics* 38.22 (2005), p. 3973 (cited on page 2).

[19] R.G. Parr, W. Yang, and Yang Yang Weitao. *Density-Functional Theory of Atoms and Molecules*. Density-functional Theory of Atoms and Molecules. Oxford University Press, USA, 1994 (cited on page 3).

[20] Christopher J Cramer. *Essentials of computational chemistry: theories and models*. John Wiley & Sons, 2013 (cited on pages 3, 11).

[21] Pascal Krause, Tillmann Klamroth, and Peter Saalfrank. 'Time-dependent configuration-interaction calculations of laser-pulse-driven many-electron dynamics: Controlled dipole switching in lithium cyanide'. In: *The Journal of chemical physics* 123.7 (2005), p. 074105 (cited on page 3).

[22] Stefan Klinkusch, Peter Saalfrank, and Tillmann Klamroth. 'Laser-induced electron dynamics including photoionization: A heuristic model within time-dependent configuration interaction theory'. In: *The Journal of chemical physics* 131.11 (2009), p. 114304 (cited on page 3).

[23] Maximilian Hollstein, Robin Santra, and Daniela Pfannkuche. 'Correlation-driven charge migration following double ionization and attosecond transient absorption spectroscopy'. In: *Physical Review A* 95.5 (2017), p. 053411 (cited on pages 3, 46).

[24] Steven R White. 'Density matrix formulation for quantum renormalization groups'. In: *Physical review letters* 69.19 (1992), p. 2863 (cited on pages 3, 16, 39).

[25] Steven R White and Richard L Martin. 'Ab initio quantum chemistry using the density matrix renormalization group'. In: *The Journal of chemical physics* 110.9 (1999), pp. 4127–4130 (cited on page 3).

[26] S Daul et al. 'Full-CI quantum chemistry using the density matrix renormalization group'. In: *International Journal of Quantum Chemistry* 79.6 (2000), pp. 331–342 (cited on page 3).

[27] Alexander O Mitrushenkov et al. 'Quantum chemistry using the density matrix renormalization group'. In: *The Journal of Chemical Physics* 115.15 (2001), pp. 6815–6821 (cited on page 3).

[28] Garnet Kin-Lic Chan and Martin Head-Gordon. 'Exact solution (within a triple-zeta, double polarization basis set) of the electronic Schrödinger equation for water'. In: *The Journal of chemical physics* 118.19 (2003), pp. 8551–8554 (cited on page 3).

[29] Garnet Kin-Lic Chan, Mihály Kállay, and Jürgen Gauss. 'State-of-the-art density matrix renormalization group and coupled cluster theory studies of the nitrogen binding curve'. In: *The Journal of chemical physics* 121.13 (2004), pp. 6110–6116 (cited on page 3).

[30] D. Perez-Garcia et al. 'Matrix Product State Representations'. In: *Quantum Info. Comput.* 7.5 (July 2007), pp. 401–430 (cited on page 4).

[31] Steven R White and Adrian E Feiguin. 'Real-time evolution using the density matrix renormalization group'. In: *Physical review letters* 93.7 (2004), p. 076401 (cited on pages 4, 20, 33).

[32] Andrew John Daley et al. 'Time-dependent density-matrix renormalization-group using adaptive effective Hilbert spaces'. In: *Journal of Statistical Mechanics: Theory and Experiment* 2004.04 (2004), P04005 (cited on page 4).

[33] Sebastian Paeckel et al. 'Time-evolution methods for matrix-product states'. In: *Annals of Physics* 411 (2019), p. 167998 (cited on pages 4, 20, 23, 33).

[34] Tirthankar Dutta and S Ramasesha. 'Double time window targeting technique: Real-time DMRG dynamics in the Pariser-Parr-Pople model'. In: *Physical Review B* 82.3 (2010), p. 035115 (cited on page 4).

[35] Michael P Zaletel et al. 'Time-evolving a matrix product state with long-ranged interactions'. In: *Physical Review B* 91.16 (2015), p. 165112 (cited on page 4).

[36] Jutho Haegeman et al. 'Unifying time evolution and optimization with matrix product states'. In: *Physical Review B* 94.16 (2016), p. 165116 (cited on pages 4, 34, 35).

[37] Valentin Zauner-Stauber and Jad C Halimeh. 'Probing the anomalous dynamical phase in long-range quantum spin chains through Fisher-zero lines'. In: *Physical Review E* 96.6 (2017), p. 062118 (cited on page 4).

[38] Jad C Halimeh and Valentin Zauner-Stauber. 'Dynamical phase diagram of quantum spin chains with long-range interactions'. In: *Physical Review B* 96.13 (2017), p. 134427 (cited on page 4).

[39] Paul Secular et al. 'Parallel time-dependent variational principle algorithm for matrix product states'. In: *Physical Review B* 101.23 (2020), p. 235123 (cited on page 4).

[40] Mingru Yang and Steven R White. 'Time-dependent variational principle with ancillary Krylov subspace'. In: *Physical Review B* 102.9 (2020), p. 094315 (cited on page 4).

[41] Luhang Yang and Adrian Feiguin. 'From deconfined spinons to coherent magnons in an antiferromagnetic Heisenberg chain with long range interactions'. In: *SciPost Physics* 10.5 (2021), p. 110 (cited on page 4).

[42] Yao Yao et al. 'Full quantum dynamics simulation of a realistic molecular system using the adaptive time-dependent density matrix renormalization group method'. In: *The journal of physical chemistry letters* 9.2 (2018), pp. 413–419 (cited on pages 4, 35).

[43] Xiaoyu Xie et al. 'Time-dependent density matrix renormalization group quantum dynamics for realistic chemical systems'. In: *The Journal of chemical physics* 151.22 (2019), p. 224101 (cited on pages 4, 35).

[44] Alberto Baiardi and Markus Reiher. 'Large-scale quantum dynamics with matrix product states'. In: *Journal of chemical theory and computation* 15.6 (2019), pp. 3481–3498 (cited on pages 4, 35).

[45] Lars-Hendrik Frahm and Daniela Pfannkuche. 'Ultrafast ab Initio Quantum Chemistry Using Matrix Product States'. In: *J. Chem. Theory Comput.* 15.4 (2019), pp. 2154–2165 (cited on pages 4, 16, 20, 23, 35, 37, 59).

[46] Alberto Baiardi. 'Electron Dynamics with the Time-Dependent Density Matrix Renormalization Group'. In: *Journal of Chemical Theory and Computation* (2021) (cited on pages 4, 35).

[47] Lars-Hendrik Frahm. 'On the Matrix Product State Approach in Time-Dependent Ab Initio Quantum Chemistry'. PhD Thesis. Universität Hamburg, 2019 (cited on pages 4, 19, 20, 31, 35, 47, 48).

[48] Frederik Weissler. 'Zeitabhängige ab initio Quantenchemie'. 2019 (cited on page 4).

[49] Darius Schaub. 'Ionization dynamics of H2O - a Matrix Product State study'. 2019 (cited on pages 4, 92).

[50] Nis-Luca van Hülst. 'Elektronendynamik des Wassermoleküls in gepulsten Feldern'. 2021 (cited on page 4).

[51] J Breidbach and LS Cederbaum. 'Migration of holes: Numerical algorithms and implementation'. In: *The Journal of chemical physics* 126.3 (2007), p. 034101 (cited on page 5).

[52] Erich Hückel. 'Quantentheoretische beiträge zum benzolproblem'. In: *Zeitschrift für Physik* 70.3-4 (1931), pp. 204–286 (cited on page 7).

[53] Roald Hoffmann. 'An extended Hückel theory. I. hydrocarbons'. In: *The Journal of Chemical Physics* 39.6 (1963), pp. 1397–1412 (cited on page 7).

[54] Charles Alfred Coulson, Brian O'Leary, and Roger B Mallion. *Hückel theory for organic chemists*. Academic Press, 1978 (cited on page 7).

[55] James JP Stewart. 'Optimization of parameters for semiempirical methods I. Method'. In: *Journal of computational chemistry* 10.2 (1989), pp. 209–220 (cited on page 7).

[56] Trygve Helgaker, Poul Jorgensen, and Jeppe Olsen. *Molecular electronic-structure theory*. John Wiley & Sons, 2014 (cited on page 7).

[57] Richard A Friesner. 'Ab initio quantum chemistry: Methodology and applications'. In: *Proceedings of the National Academy of Sciences* 102.19 (2005), pp. 6648–6653 (cited on pages 7, 46).

[58] Ramamurti Shankar. *Principles of quantum mechanics*. Springer Science & Business Media, 2012 (cited on page 8).

[59] Jack Simons. 'An experimental chemist's guide to ab initio quantum chemistry'. In: *The Journal of Physical Chemistry* 95.3 (1991), pp. 1017–1029 (cited on page 8).

[60] Frank Jensen. *Introduction to computational chemistry*. John wiley & sons, 2017 (cited on pages 8, 11).

[61] Max Born and Robert Oppenheimer. 'Zur quantentheorie der molekeln'. In: *Annalen der physik* 389.20 (1927), pp. 457–484 (cited on page 8).

[62] Ira N Levine. *Quantum chemistry*. Pearson Education, 2013 (cited on page 8).

[63] Attila Szabo and Neil S Ostlund. *Modern quantum chemistry: introduction to advanced electronic structure theory*. Courier Corporation, 2012 (cited on pages 10, 11, 13, 65, 66).

[64] Chr Møller and Milton S Plesset. 'Note on an approximation treatment for many-electron systems'. In: *Physical review* 46.7 (1934), p. 618 (cited on page 11).

[65] Hendrik J Monkhorst. 'Calculation of properties with the coupled-cluster method'. In: *International Journal of Quantum Chemistry* 12.S11 (1977), pp. 421–432 (cited on page 11).

[66] C David Sherrill and Henry F Schaefer III. 'The configuration interaction method: Advances in highly correlated approaches'. In: *Advances in quantum chemistry* 34 (1999), pp. 143–269 (cited on page 11).

[67] Isaiah Shavitt and Rodney J Bartlett. *Many-body methods in chemistry and physics: MBPT and coupled-cluster theory*. Cambridge university press, 2009 (cited on page 11).

[68] Szilárd Szalay et al. 'Tensor product methods and entanglement optimization for ab initio quantum chemistry'. In: *International Journal of Quantum Chemistry* 115.19 (2015), pp. 1342–1391 (cited on page 13).

[69] RK Nesbet. 'Configuration interaction in orbital theories'. In: *Proceedings of the Royal Society of London. Series A. Mathematical and Physical Sciences* 230.1182 (1955), pp. 312–321 (cited on page 14).

[70] Stephen R Langhoff and Ernest R Davidson. 'Configuration interaction calculations on the nitrogen molecule'. In: *International Journal of Quantum Chemistry* 8.1 (1974), pp. 61–72 (cited on page 14).

[71] Jeremy P Coe. 'Machine learning configuration interaction'. In: *Journal of chemical theory and computation* 14.11 (2018), pp. 5739–5749 (cited on page 14).

[72] Frank Neese. 'A spectroscopy oriented configuration interaction procedure'. In: *The Journal of chemical physics* 119.18 (2003), pp. 9428–9443 (cited on page 14).

[73] Loren Greenman et al. 'Implementation of the time-dependent configuration-interaction singles method for atomic strong-field processes'. In: *Physical Review A* 82.2 (2010), p. 023406 (cited on page 14).

[74] Antonia Karamatskou et al. 'Calculation of photoelectron spectra within the time-dependent configuration-interaction singles scheme'. In: *Physical Review A* 89.3 (2014), p. 033415 (cited on page 14).

[75] Nina Rohringer, Ariel Gordon, and Robin Santra. 'Configuration-interaction-based time-dependent orbital approach for ab initio treatment of electronic dynamics in a strong optical laser field'. In: *Physical Review A* 74.4 (2006), p. 043420 (cited on page 14).

[76] Tillmann Klamroth. 'Laser-driven electron transfer through metal-insulator-metal contacts: Time-dependent configuration interaction singles calculations for a jellium model'. In: *Physical Review B* 68.24 (2003), p. 245421 (cited on page 14).

[77] Maximilian Hollstein and Daniela Pfannkuche. 'Multielectron dynamics in the tunneling ionization of correlated quantum systems'. In: *Physical Review A* 92.5 (2015), p. 053421 (cited on page 14).

[78] Jane K Cullum and Ralph A Willoughby. *Lanczos algorithms for large symmetric eigenvalue computations: Vol. I: Theory*. SIAM, 2002 (cited on page 15).

[79] Ulrich Schollwöck. 'The density-matrix renormalization group'. In: *Reviews of modern physics* 77.1 (2005), p. 259 (cited on page 15).

[80] D Perez-Garcia et al. 'Matrix product state representations'. In: *QUANTUM INFORMATION & COMPUTATION* 7.5-6 (2007), pp. 401–430 (cited on page 15).

[81] Gregory M Crosswhite and Dave Bacon. 'Finite automata for caching in matrix product algorithms'. In: *Physical Review A* 78.1 (2008), p. 012356 (cited on page 15).

[82] Ulrich Schollwöck. 'The density-matrix renormalization group in the age of matrix product states'. In: *Ann. Phys. (N. Y.)* 326.1 (2011), pp. 96–192 (cited on pages 15, 16, 18, 38).

[83] Hong-Chen Jiang, Zheng-Yu Weng, and Tao Xiang. 'Accurate determination of tensor network state of quantum lattice models in two dimensions'. In: *Phys. Rev. Lett.* 101.9 (2008), p. 090603 (cited on page 16).

[84] Thomas Huckle, Konrad Waldherr, and Thomas Schulte-Herbrüggen. 'Computations in quantum tensor networks'. In: *Linear Algebra Its Appl.* 438.2 (2013), pp. 750–781 (cited on page 16).

[85] Román Orús. 'A practical introduction to tensor networks: Matrix product states and projected entangled pair states'. In: *Annals of Physics* 349 (2014), pp. 117–158 (cited on pages 16, 19, 20).

[86] Stellan Östlund and Stefan Rommer. 'Thermodynamic limit of density matrix renormalization'. In: *Physical review letters* 75.19 (1995), p. 3537 (cited on page 16).

[87] Tomotoshi Nishino and Andrej Gendiar. 'Origin of Matrix Product State in Statistical Mechanics'. In: *International Workshop on Density Matrix Renormalization Group and Other Advances in Numerical Renormalization Group Methods, August 23-September*. Vol. 3. 2010 (cited on page 16).

[88] Steven R White. 'Density-matrix algorithms for quantum renormalization groups'. In: *Physical Review B* 48.14 (1993), p. 10345 (cited on pages 16, 41).

[89] B Lake et al. 'Multispinon continua at zero and finite temperature in a near-ideal Heisenberg chain'. In: *Physical review letters* 111.13 (2013), p. 137205 (cited on page 16).

[90] Simeng Yan, David A Huse, and Steven R White. 'Spin-liquid ground state of the S= 1/2 kagome Heisenberg antiferromagnet'. In: *Science* 332.6034 (2011), pp. 1173–1176 (cited on page 16).

[91] Vedika Khemani, Frank Pollmann, and Shivaji Lal Sondhi. 'Obtaining highly excited eigenstates of many-body localized hamiltonians by the density matrix renormalization group approach'. In: *Physical review letters* 116.24 (2016), p. 247204 (cited on page 16).

[92] DM Kennes and Christoph Karrasch. 'Entanglement scaling of excited states in large one-dimensional many-body localized systems'. In: *Physical Review B* 93.24 (2016), p. 245129 (cited on page 16).

[93] Sebastian Wouters et al. 'CheMPS2: A free open-source spin-adapted implementation of the density matrix renormalization group for ab initio quantum chemistry'. In: *Computer Physics Communications* 185.6 (2014), pp. 1501–1514 (cited on pages 16, 27, 43).

[94] Sebastian Wouters and Dimitri Van Neck. 'The density matrix renormalization group for ab initio quantum chemistry'. In: *The European Physical Journal D* 68.9 (2014), p. 272 (cited on pages 16, 24, 40, 41).

[95] Sebastian Keller et al. 'An efficient matrix product operator representation of the quantum chemical Hamiltonian'. In: *The Journal of chemical physics* 143.24 (2015), p. 244118 (cited on page 16).

[96] Soichi Shirai, Yuki Kurashige, and Takeshi Yanai. 'Computational evidence of inversion of 1La and 1Lb-derived excited states in naphthalene excimer formation from ab Initio multireference theory with large active space: DMRG-CASPT2 Study'. In: *Journal of chemical theory and computation* 12.5 (2016), pp. 2366–2372 (cited on page 16).

[97] Jiri Brabec et al. 'Massively parallel quantum chemical density matrix renormalization group method'. In: *Journal of computational chemistry* 42.8 (2021), pp. 534–544 (cited on page 16).

[98] Fabian M Faulstich et al. 'Numerical and theoretical aspects of the DMRG-TCC method exemplified by the nitrogen dimer'. In: *Journal of chemical theory and computation* 15.4 (2019), pp. 2206–2220 (cited on page 16).

[99] Biswa Nath Datta. *Numerical linear algebra and applications*. Vol. 116. Siam, 2010 (cited on page 17).

[100] Ivan V Oseledets. 'Tensor-train decomposition'. In: *SIAM Journal on Scientific Computing* 33.5 (2011), pp. 2295–2317 (cited on page 18).

[101] Jens Eisert, Marcus Cramer, and Martin B Plenio. 'Colloquium: Area laws for the entanglement entropy'. In: *Reviews of Modern Physics* 82.1 (2010), p. 277 (cited on page 19).

[102] Karel Van Acoleyen, Michaël Mariën, and Frank Verstraete. 'Entanglement rates and area laws'. In: *Physical review letters* 111.17 (2013), p. 170501 (cited on page 19).

[103] Ö Legeza, J Röder, and BA Hess. 'QC-DMRG study of the ionic-neutral curve crossing of LiF'. In: *Molecular Physics* 101.13 (2003), pp. 2019–2028 (cited on page 20).

[104] Gerrit Moritz, Alexander Wolf, and Markus Reiher. 'Relativistic DMRG calculations on the curve crossing of cesium hydride'. In: *The Journal of chemical physics* 123.18 (2005), p. 184105 (cited on page 20).

[105] Sebastian F Keller and Markus Reiher. 'Determining Factors for the Accuracy of DMRG in Chemistry'. In: *arXiv preprint arXiv:1401.5497* (2014) (cited on page 20).

[106] Sebastian Keller et al. 'An efficient matrix product operator representation of the quantum chemical Hamiltonian'. In: *The Journal of chemical physics* 143.24 (2015), p. 244118 (cited on page 20).

[107] Sebastian Wouters et al. 'CheMPS2: Improved DMRG-SCF routine and correlation functions'. In: *Computer Physics Communications* 191 (2015), pp. 235–237 (cited on page 20).

[108] Alberto Baiardi and Markus Reiher. 'The density matrix renormalization group in chemistry and molecular physics: Recent developments and new challenges'. In: *The Journal of Chemical Physics* 152.4 (2020), p. 040903 (cited on page 20).

[109] Dominique Gobert et al. 'Real-time dynamics in spin-1 2 chains with adaptive time-dependent density matrix renormalization group'. In: *Physical Review E* 71.3 (2005), p. 036102 (cited on page 20).

[110] Juan José Garca-Ripoll. 'Time evolution of matrix product states'. In: *New Journal of Physics* 8.12 (2006), p. 305 (cited on pages 20, 33).

[111] F Heidrich-Meisner, Adrian E Feiguin, and E Dagotto. 'Real-time simulations of nonequilibrium transport in the single-impurity Anderson model'. In: *Physical Review B* 79.23 (2009), p. 235336 (cited on page 20).

[112] Enrico Ronca et al. 'Time-step targeting time-dependent and dynamical density matrix renormalization group algorithms with ab initio Hamiltonians'. In: *Journal of chemical theory and computation* 13.11 (2017), pp. 5560–5571 (cited on page 20).

[113] Alberto Baiardi and Markus Reiher. 'Large-scale quantum dynamics with matrix product states'. In: *Journal of chemical theory and computation* 15.6 (2019), pp. 3481–3498 (cited on page 20).

[114] Xiaoyu Xie et al. 'Time-dependent density matrix renormalization group quantum dynamics for realistic chemical systems'. In: *The Journal of Chemical Physics* 151.22 (2019), p. 224101 (cited on page 20).

[115] Frank Verstraete, Valentin Murg, and J Ignacio Cirac. 'Matrix product states, projected entangled pair states, and variational renormalization group methods for quantum spin systems'. In: *Advances in Physics* 57.2 (2008), pp. 143–224 (cited on page 20).

[116] Frank Verstraete et al. 'Criticality, the area law, and the computational power of projected entangled pair states'. In: *Physical review letters* 96.22 (2006), p. 220601 (cited on page 20).

[117] Valentin Murg et al. 'Simulating strongly correlated quantum systems with tree tensor networks'. In: *Physical Review B* 82.20 (2010), p. 205105 (cited on page 20).

[118] Y-Y Shi, L-M Duan, and Guifre Vidal. 'Classical simulation of quantum many-body systems with a tree tensor network'. In: *Physical review a* 74.2 (2006), p. 022320 (cited on page 20).

[119] Luca Tagliacozzo, Glen Evenbly, and Guifré Vidal. 'Simulation of two-dimensional quantum systems using a tree tensor network that exploits the entropic area law'. In: *Physical Review B* 80.23 (2009), p. 235127 (cited on page 20).

[120] Adrián Franco-Rubio and Guifré Vidal. 'Entanglement and correlations in the continuous multi-scale entanglement renormalization ansatz'. In: *Journal of High Energy Physics* 2017.12 (2017), p. 129 (cited on page 20).

[121] Bartlomiej Czech et al. 'Tensor networks from kinematic space'. In: *Journal of High Energy Physics* 2016.7 (2016), p. 100 (cited on page 20).

[122] Garnet Kin-Lic Chan et al. 'Matrix product operators, matrix product states, and ab initio density matrix renormalization group algorithms'. In: *The Journal of chemical physics* 145.1 (2016), p. 014102 (cited on pages 22, 23).

[123] Peter W Atkins and Ronald S Friedman. *Molecular quantum mechanics*. Oxford university press, 2011 (cited on page 28).

[124] Ian P McCulloch and Miklos Gulácsi. 'Density matrix renormalisation group method and symmetries of the Hamiltonian'. In: *Australian Journal of Physics* 53.4 (2000), pp. 597–612 (cited on page 31).

[125] Ian P McCulloch and Miklós Gulácsi. 'Total spin in the density matrix renormalization group algorithm'. In: *Philosophical magazine letters* 81.6 (2001), pp. 447–453 (cited on page 31).

[126] Ian P McCulloch and Miklós Gulácsi. 'The non-Abelian density matrix renormalization group algorithm'. In: *EPL (Europhysics Letters)* 57.6 (2002), p. 852 (cited on page 31).

[127] J. J. Sakurai and Jim Napolitano. *Modern Quantum Mechanics*. 2nd ed. Cambridge University Press, 2017 (cited on page 31).

[128] N. Zettili. *Quantum Mechanics: Concepts and Applications*. Wiley, 2009 (cited on page 31).

[129] Albert Messiah. *Albert Messiah: Quantenmechanik. Band 2*. Vol. 2. Walter de Gruyter, 1990 (cited on page 31).

[130] Sebastian Wouters. 'Accurate variational electronic structure calculations with the density matrix renormalization group'. PhD thesis. Ghent University, 2014 (cited on pages 31, 41).

[131] Guifré Vidal. 'Efficient simulation of one-dimensional quantum many-body systems'. In: *Physical review letters* 93.4 (2004), p. 040502 (cited on page 34).

[132] Masuo Suzuki. 'Generalized Trotter's formula and systematic approximants of exponential operators and inner derivations with applications to many-body problems'. In: *Communications in Mathematical Physics* 51.2 (1976), pp. 183–190 (cited on page 34).

[133] Hale F Trotter. 'On the product of semi-groups of operators'. In: *Proceedings of the American Mathematical Society* 10.4 (1959), pp. 545–551 (cited on page 34).

[134] Jutho Haegeman et al. 'Time-dependent variational principle for quantum lattices'. In: *Physical review letters* 107.7 (2011), p. 070601 (cited on pages 34, 35).

[135] Benedikt Kloss, Yevgeny Bar Lev, and David Reichman. 'Time-dependent variational principle in matrix-product state manifolds: Pitfalls and potential'. In: *Physical Review B* 97.2 (2018), p. 024307 (cited on pages 34, 35).

[136] Claudius Hubig. 'Symmetry-protected tensor networks'. PhD thesis. lmu, 2017 (cited on page 35).

[137] Marko Medenjak and Jacopo De Nardis. 'Domain wall melting in spin-1 XXZ chains'. In: *Physical Review B* 101.8 (2020), p. 081411 (cited on page 35).

[138] Yantao Wu. 'Time-dependent variational principle for mixed matrix product states in the thermodynamic limit'. In: *Physical Review B* 102.13 (2020), p. 134306 (cited on page 35).

[139] Raffaele Borrelli and Maxim F Gelin. 'Simulation of quantum dynamics of excitonic systems at finite temperature: An efficient method based on thermo field dynamics'. In: *Scientific reports* 7.1 (2017), pp. 1–9 (cited on page 35).

[140] Carl Runge. ' "U about the numerical solution ö solution of differential equations'. In: *mathematical annals* 46.2 (1895), pp. 167–178 (cited on page 35).

[141] Wilhelm Kutta. 'Beitrag zur naherungsweisen integration totaler differentialgleichungen'. In: *Z. Math. Phys.* 46 (1901), pp. 435–453 (cited on page 35).

[142] Tae Jun Park and JC Light. 'Unitary quantum time evolution by iterative Lanczos reduction'. In: *The Journal of chemical physics* 85.10 (1986), pp. 5870–5876 (cited on page 35).

[143] Marlis Hochbruck and Christian Lubich. 'On Krylov subspace approximations to the matrix exponential operator'. In: *SIAM Journal on Numerical Analysis* 34.5 (1997), pp. 1911–1925 (cited on page 35).

[144] PE Dargel et al. 'Lanczos algorithm with matrix product states for dynamical correlation functions'. In: *Physical Review B* 85.20 (2012), p. 205119 (cited on page 35).

[145] Michael L Wall. 'Out-of-equilibrium dynamics with matrix product states'. In: *Quantum Many-Body Physics of Ultracold Molecules in Optical Lattices*. Springer, 2015, pp. 177–222 (cited on page 35).

[146] Cornelius Lanczos. 'An iteration method for the solution of the eigenvalue problem of linear differential and integral operators'. In: (1950) (cited on page 35).

[147] Yousef Saad. *Iterative methods for sparse linear systems*. SIAM, 2003 (cited on page 35).

[148] Garnet Kin-Lic Chan and Martin Head-Gordon. 'Highly correlated calculations with a polynomial cost algorithm: A study of the density matrix renormalization group'. In: *The Journal of chemical physics* 116.11 (2002), pp. 4462–4476 (cited on pages 41, 42, 93).

[149] Dominika Zgid and Marcel Nooijen. 'Obtaining the two-body density matrix in the density matrix renormalization group method'. In: *The Journal of chemical physics* 128.14 (2008), p. 144115 (cited on pages 41, 42).

[150] Steven R White. 'Density matrix renormalization group algorithms with a single center site'. In: *Physical Review B* 72.18 (2005), p. 180403 (cited on page 42).

[151] Johannes Hachmann, Wim Cardoen, and Garnet Kin-Lic Chan. 'Multireference correlation in long molecules with the quadratic scaling density matrix renormalization group'. In: *The Journal of chemical physics* 125.14 (2006), p. 144101 (cited on page 43).

[152] Jonathan J Dorando, Johannes Hachmann, and Garnet Kin-Lic Chan. 'Targeted excited state algorithms'. In: *The Journal of chemical physics* 127.8 (2007), p. 084109 (cited on page 43).

[153] Yuki Kurashige and Takeshi Yanai. 'High-performance ab initio density matrix renormalization group method: Applicability to large-scale multireference problems for metal compounds'. In: *The Journal of chemical physics* 130.23 (2009), p. 234114 (cited on page 43).

[154] Sebastian Wouters et al. 'Longitudinal static optical properties of hydrogen chains: Finite field extrapolations of matrix product state calculations'. In: *The Journal of chemical physics* 136.13 (2012), p. 134110 (cited on page 43).

[155] Huanchen Zhai and Garnet Kin-Lic Chan. 'Low communication high performance ab initio density matrix renormalization group algorithms'. In: *The Journal of Chemical Physics* 154.22 (2021), p. 224116 (cited on page 43).

[156] Roberto Olivares-Amaya et al. 'The ab-initio density matrix renormalization group in practice'. In: *The Journal of chemical physics* 142.3 (2015), p. 034102 (cited on pages 43, 51).

[157] R Noack and S White. *D. Scalapino in Computer Simulations in Condensed Matter Physics VII, edited by D. Landau, K.-K. Mon and H.-B. Schüttler*. 1994 (cited on page 43).

[158] Steven R White. 'Spin gaps in a frustrated Heisenberg model for CaV 4 O 9'. In: *Physical review letters* 77.17 (1996), p. 3633 (cited on page 43).

[159] Garnet Kin-Lic Chan. 'An algorithm for large scale density matrix renormalization group calculations'. In: *The Journal of chemical physics* 120.7 (2004), pp. 3172–3178 (cited on page 43).

[160] EM Stoudenmire and Steven R White. 'Real-space parallel density matrix renormalization group'. In: *Physical review B* 87.15 (2013), p. 155137 (cited on page 43).

[161] Sebastian Wouters, Veronique Van Speybroeck, and Dimitri Van Neck. 'DMRG-CASPT2 study of the longitudinal static second hyperpolarizability of all-trans polyenes'. In: *The Journal of chemical physics* 145.5 (2016), p. 054120 (cited on page 43).

[162] Si I Gorelsky and ABP Lever. 'Electronic structure and spectra of ruthenium diimine complexes by density functional theory and INDO/S. Comparison of the two methods'. In: *Journal of Organometallic Chemistry* 635.1-2 (2001), pp. 187–196 (cited on page 46).

[163] S Piskunov et al. 'Bulk properties and electronic structure of SrTiO3, BaTiO3, PbTiO3 perovskites: an ab initio HF/DFT study'. In: *Computational Materials Science* 29.2 (2004), pp. 165–178 (cited on page 46).

[164] Andrea Decker et al. 'Spectroscopic and Quantum Chemical Studies on Low-Spin FeIV O Complexes: Fe- O Bonding and Its Contributions to Reactivity'. In: *Journal of the American Chemical Society* 129.51 (2007), pp. 15983–15996 (cited on page 46).

[165] RN Straker et al. 'Computational ligand design in enantio-and diastereoselective ynamide [5+ 2] cycloisomerization'. In: *Nature communications* 7.1 (2016), pp. 1–9 (cited on page 46).

[166] Andreas Bergner et al. 'Ab initio energy-adjusted pseudopotentials for elements of groups 13–17'. In: *Molecular Physics* 80.6 (1993), pp. 1431–1441 (cited on page 46).

[167] Warren J Hehre, Robert Ditchfield, and John A Pople. 'Selfconsistent molecular orbital methods. XII. Further extensions of Gaussiantype basis sets for use in molecular orbital studies of organic molecules'. In: *The Journal of Chemical Physics* 56.5 (1972), pp. 2257–2261 (cited on page 46).

[168] Hans-Joachim Werner et al. 'Molpro: a general-purpose quantum chemistry program package'. In: *Wiley Interdisciplinary Reviews: Computational Molecular Science* 2.2 (2012), pp. 242–253 (cited on pages 46, 78, 80).

[169] Örs Legeza and Jeno Sólyom. 'Optimizing the density-matrix renormalization group method using quantum information entropy'. In: *Physical Review B* 68.19 (2003), p. 195116 (cited on pages 50, 93).

[170] Gergely Barcza et al. 'Quantum-information analysis of electronic states of different molecular structures'. In: *Physical Review A* 83.1 (2011), p. 012508 (cited on pages 50–52).

[171] Gerrit Moritz, Bernd Artur Hess, and Markus Reiher. 'Convergence behavior of the density-matrix renormalization group algorithm for optimized orbital orderings'. In: *The Journal of chemical physics* 122.2 (2005), p. 024107 (cited on pages 51, 93).

[172] Naoki Nakatani and Garnet Kin-Lic Chan. 'Efficient tree tensor network states (TTNS) for quantum chemistry: Generalizations of the density matrix renormalization group algorithm'. In: *The Journal of chemical physics* 138.13 (2013), p. 134113 (cited on page 51).

[173] Miroslav Fiedler. 'Algebraic connectivity of graphs'. In: *Czechoslovak mathematical journal* 23.2 (1973), pp. 298–305 (cited on page 52).

[174] Miroslav Fiedler. 'A property of eigenvectors of nonnegative symmetric matrices and its application to graph theory'. In: *Czechoslovak mathematical journal* 25.4 (1975), pp. 619–633 (cited on page 52).

[175] TD Thomas et al. 'Anomalous Natural Linewidth in the 2 p Photoelectron Spectrum of S i F 4'. In: *Physical review letters* 89.22 (2002), p. 223001 (cited on pages 61, 91).

[176] Morgane Vacher et al. 'Electron dynamics following photoionization: Decoherence due to the nuclear-wave-packet width'. In: *Physical Review A* 92.4 (2015), p. 040502 (cited on pages 61, 73, 87).

[177] Robert S Mulliken. 'Electronic population analysis on LCAO–MO molecular wave functions. I'. In: *The Journal of Chemical Physics* 23.10 (1955), pp. 1833–1840 (cited on page 63).

[178] Linlin Zhong, Xiaohua Wang, and Mingzhe Rong. 'Molecular orbital composition and its effect on electron-impact ionization cross sections of molecules: A comparative study'. In: *Physics of Plasmas* 25.10 (2018), p. 103507 (cited on page 63).

[179] Pieter Ros and GCA Schuit. 'Molecular orbital calculations on copper chloride complexes'. In: *Theoretica chimica acta* 4.1 (1966), pp. 1–12 (cited on page 63).

[180] Tian Lu and Feiwu Chen. 'Multiwfn: a multifunctional wavefunction analyzer'. In: *Journal of computational chemistry* 33.5 (2012), pp. 580–592 (cited on page 64).

[181] Volker Engel. 'The calculation of autocorrelation functions for spectroscopy'. In: *Chemical physics letters* 189.1 (1992), pp. 76–78 (cited on page 68).

[182] MD Feit and JA Fleck Jr. 'Solution of the Schrödinger equation by a spectral method II: Vibrational energy levels of triatomic molecules'. In: *The Journal of Chemical Physics* 78.1 (1983), pp. 301–308 (cited on page 68).

[183] Michael H Beck et al. 'The multiconfiguration time-dependent Hartree (MCTDH) method: a highly efficient algorithm for propagating wavepackets'. In: *Physics reports* 324.1 (2000), pp. 1–105 (cited on page 68).

[184] Reinhard Schinke. *Photodissociation dynamics: spectroscopy and fragmentation of small polyatomic molecules*. 1. Cambridge University Press, 1995 (cited on page 68).

[185] Siegfried Lünnemann, Alexander I Kuleff, and Lorenz S Cederbaum. 'Ultrafast electron dynamics following outer-valence ionization: The impact of low-lying relaxation satellite states'. In: *The Journal of chemical physics* 130.15 (2009), 04B616 (cited on page 69).

[186] Andrew J Jenkins et al. 'Nuclear spatial delocalization silences electron density oscillations in 2-phenyl-ethyl-amine (PEA) and 2-phenylethyl-N, N-dimethylamine (PENNA) cations'. In: *The Journal of chemical physics* 144.10 (2016), p. 104110 (cited on page 73).

[187] Andrew J Jenkins et al. 'Charge migration in polycyclic norbornadiene cations: Winning the race against decoherence'. In: *The Journal of chemical physics* 145.16 (2016), p. 164103 (cited on page 73).

[188] Morgane Vacher et al. 'Electron and nuclear dynamics following ionisation of modified bismethylene-adamantane'. In: *Faraday discussions* 194 (2016), pp. 95–115 (cited on page 73).

[189] E Bright Wilson, JC Decius, and Paul C Cross. *Molecular Vibrations: The Theory of Infrared and Raman Vibrational Spectra*. Courier Corporation, 2012 (cited on page 76).

[190] Marie-Geneviève Barthés-Labrousse. 'The Auger Effect'. In: *Microscopy Microanalysis Microstructures* 6.3 (1995), pp. 253–262 (cited on page 91).

[191] TR Walsh, TE Meehan, and FP Larkins. 'Molecular Auger rates using a statistical model and ab initio wavefunctions'. In: *Journal of Physics B: Atomic, Molecular and Optical Physics* 27.19 (1994), p. L657 (cited on page 91).

[192] Jürgen Zobeley, Robin Santra, and Lorenz S Cederbaum. 'Electronic decay in weakly bound heteroclusters: Energy transfer versus electron transfer'. In: *The Journal of Chemical Physics* 115.11 (2001), pp. 5076–5088 (cited on page 91).

[193] Robin Santra and Lorenz S Cederbaum. 'Non-Hermitian electronic theory and applications to clusters'. In: *Physics reports* 368.1 (2002), pp. 1–117 (cited on page 91).

[194] Christian Buth, Robin Santra, and Lorenz S Cederbaum. 'Impact of interatomic electronic decay processes on Xe 4d hole decay in the xenon fluorides'. In: *The Journal of chemical physics* 119.20 (2003), pp. 10575–10584 (cited on page 91).

[195] Vitali Averbukh and Lorenz S Cederbaum. 'Ab initio calculation of interatomic decay rates by a combination of the Fano ansatz, Greens-function methods, and the Stieltjes imaging technique'. In: *The Journal of chemical physics* 123.20 (2005), p. 204107 (cited on page 91).

[196] Nicolas Sisourat et al. 'Impact of nuclear dynamics on interatomic Coulombic decay in a He dimer'. In: *Physical Review A* 82.5 (2010), p. 053401 (cited on page 91).

[197] T Miteva et al. 'The effect of the partner atom on the spectra of interatomic Coulombic decay triggered by resonant Auger processes'. In: *The Journal of chemical physics* 141.16 (2014), p. 164303 (cited on page 91).

[198] Alexander I Kuleff and Lorenz S Cederbaum. 'Tracing ultrafast interatomic electronic decay processes in real time and space'. In: *Physical review letters* 98.8 (2007), p. 083201 (cited on page 91).

[199] Alexander I Kuleff. 'Electronic decay through carbon chains'. In: *Chemical Physics* 482 (2017), pp. 216–220 (cited on page 91).

[200] John B Mullenix, Victor Despré, and Alexander I Kuleff. 'Electronic decay through non-linear carbon chains'. In: *Journal of Physics B: Atomic, Molecular and Optical Physics* 53.18 (2020), p. 184006 (cited on page 91).

[201] Ralph Püttner et al. 'Si 1s- 1, 2s- 1 and 2p- 1 lifetime broadening of SiX 4 (X= F, Cl, Br, CH 3) molecules: SiF 4 anomalous behaviour reassessed'. In: *Physical Chemistry Chemical Physics* 21.17 (2019), pp. 8827–8836 (cited on page 91).

[202] Jörg Rissler, Reinhard M Noack, and Steven R White. 'Measuring orbital interaction using quantum information theory'. In: *Chemical Physics* 323.2-3 (2006), pp. 519–531 (cited on page 93).